nature cell biology

Article

https://doi.org/10.1038/s41556-026-01966-0

# Diffusing caveolin-1 scaffolds regulate mechanosignalling

Received: 9 December 2024

Accepted: 20 April 2026

Satish Kailasam Mani[1,2,3,16], Nicolas Tardif[1,2,3,12,16], Olivier Rossier[4,5,16], Ismail M. Khater[6,7], Xuesi Zhou[4,5], Victor Breton[1,2,3], Filipe Nunes Vicente[4,5,13], Adiyodi Veettil Radhakrishnan[4,5,14], Céline Gracia[1,2,3], Pamela Gonzalez Troncoso[1,2,3], Isabel Brito[8], Richard Ruez[1,2,3,15], Melissa Dewulf[1,2,3], Ghassan Hamarneh[6], Ivan Robert Nabi[9], Philippe Cuniasse[10], Pierre Sens[11], Grégory Giannone[4,5,17], Cédric M. Blouin[1,2,3,17] ✉ & Christophe Lamaze[1,2,3,17] ✉

Caveolae are invaginated plasma membrane nanodomains traditionally associated with membrane trafficking and signalling. These multifunctional organelles are also essential mechanosensors mediating the cell response to mechanical stress. We investigated the role of caveolae mechanics in regulating various signalling pathways. Single-molecule imaging and super-resolution microscopy revealed that mechanical stress rapidly triggers caveolae disassembly and the release of caveolin-1 scaffolds, which then exhibit enhanced diffusion at the plasma membrane. This promoted direct interaction between the caveolin-1 scaffolding domain and the tyrosine kinase JAK1, leading to the inhibition of its catalytic activity. A similar process was observed for eNOS, PTEN and PTP1B. The control of signalling by diffusing Cav1 scaffolds was further validated by a theoretical model based on caveolae thermodynamics. These findings establish a mechanotransduction paradigm in which signalling information is decoded remotely from the initial mechanosensing caveola, through dynamic and reversible assembly of tension-controlled complexes between signalling effectors and caveolin-1 scaffolds.

Caveolae are discrete bulb-shaped plasma membrane structures with diameters of 50–80 nm that can cluster into 'rosettes'[1,2]. They were first identified by electron microscopy (EM) in epithelial and endothelial cells over 70 years ago[3,4]. The integral membrane protein caveolin-1 (Cav1) oligomerizes to form the primary 8S building blocks of caveolae assembly in many cell types, particularly in adipocytes, endothelial cells and muscle cells. The caveolin family consist of three isoforms: Cav1, caveolin-2 (Cav2) and muscle-specific caveolin-3 (Cav3)[5–7]. Despite early EM observations of electron-dense cytoplasmic regions, caveolae were long considered non-coated invaginations, in contrast to the fuzzy coat of clathrin-coated pits. The composition and organization of the caveolar coat were clarified with the discovery of the cavin family of proteins (Cavin1–Cavin4). Cavin1, is essential for caveolae morphogenesis in all cell types[8], whereas Cavin4 expression is restricted to muscle cells[9–11]. Accessory proteins, including EHD2, pacsin2/syndapin2 (pacsin3/syndapin3 in muscle) and filamin A, localize to the caveolar neck and regulate stability and dynamics through interactions with the actin cytoskeleton[12–16]. A recent cryo-EM study resolved the quaternary structure of the Cav1 complex, revealing an 8S assembly of 11 primary α-helical protomers that are tightly arranged into a ~14-nm spiral disc with N termini on the outer ring and C termini forming a central β-barrel[17].

Caveolae and Cav1 have been implicated in diverse biological processes, including transcytosis, endocytosis, lipid homeostasis and signal transduction[18–21], and are linked to multiple human diseases[22]. For example, mutations or altered expression of caveolins and cavins

A full list of affiliations appears at the end of the paper. ✉e-mail: cedric.blouin@curie.fr; christophe.lamaze@curie.fr

are associated with lipodystrophy, vascular dysfunction, cancer and muscle dystrophies[23–26].

A major focus has been the role of Cav1 in intracellular signalling[1,27,28]. Earlier studies proposed that caveolae and/or Cav1 modulate the activity of numerous growth factors, signalling receptors, and kinases, including endothelial nitric oxide synthase (eNOS), the insulin receptor, the epidermal growth factor receptor (EGFR), Src-family kinases and HRas/KRas[29–33]. However, the reliance on Cav1 and signalling protein overexpression systems raised concerns about artefactual localization. Indeed, caveolae seem to exclude most transmembrane and cytosolic proteins while concentrating lipids[34]. This led to the proposal that Cav1 can regulate signalling outside caveolae, as endogenous Cav1 inhibits EGFR signalling in tumour cells that lack caveolae[35]. Subsequent work showed that Cav1 controls migration and tumour progression through the regulation of focal adhesion and membrane tension in prostate cancer PC3 cells devoid of Cavin1 and therefore of caveolae[9,36–38]. These non-caveolar Cav1 assemblies, termed scaffolds[39], have been recently visualized at the plasma membrane by super-resolution microscopy and EM[40–42]. How the key role of Cav1 in caveolae formation relates to its regulation of signalling effectors that are located outside caveolae remains unclear, making it a prime research focus.

In 2011, we uncovered a key role for caveolae in mechanosensing. Mechanical stress induces rapid flattening of caveolae, increasing membrane area and buffering membrane tension to prevent rupture[43]. This essential function of caveolae has been validated across several cell types in vitro and in vivo[42,44–48] and has prompted a reassessment of caveolae biology in the context of cell mechanics[2,49–52].

Here, we examined how the tension-dependent cycle of caveolae disassembly and reassembly regulates intracellular signalling. Using super-resolution and live-cell single-molecule imaging, we show that mechanical stress rapidly converts caveolae into smaller Cav1 assemblies corresponding to scaffolds. These scaffolds diffuse rapidly within the plasma membrane and directly interact via the Cav1 scaffolding domain (CSD) with signalling effectors outside caveolae, including the Janus kinase JAK1, leading to inhibition of its catalytic activity and reduced STAT3 activation upon interferon (IFN)-α stimulation. Upon stress release, JAK–STAT signalling is restored. AlphaFold3 (AF3) predictions combined with molecular dynamics (MD) simulations provide a structural model of the Cav1–JAK1 interaction, consistent with Cav1 mutagenesis data and identifies candidate JAK1 interface residues. We extend the mechanical regulation of signalling by Cav1 scaffolds to PTEN, PTP1B and eNOS. A thermodynamics model of caveolae assembly and disassembly under mechanical stress recapitulates these observations and supports the generality of this signalling mechanism. Altogether, our study establishes a mechanotransduction paradigm whereby selective signalling pathways are regulated at locations distant from caveolae.

## Results

### The JAK–STAT signalling pathway is controlled by caveolae under mechanical stress

We investigated whether the mechano-dependent cycle of caveolae disassembly/reassembly acts as a switch to regulate signalling pathways[1,49]. Our previous studies suggesting that caveolae mechanics could regulate JAK–STAT signalling in muscle cells[53] prompted us to further explore this regulatory mechanism in mouse lung endothelial cells (MLECs), which are particularly enriched in caveolae. Upon IFNα stimulation, wild-type (WT) and Cav1 knockout ($\mathrm{Cav1}^{-/-}$) MLECs were subjected to 25% uniaxial stretch. STAT3 phosphorylation (pSTAT3 Tyr705) decreased by 52% in stretched WT cells compared with resting cells (Fig. 1a), whereas no activation occurred without IFNα (Extended Data Fig. 1a). This reduction was absent in $\mathrm{Cav1}^{-/-}$ cells, indicating that this regulatory mechanism depends on the presence of functional caveolae and/or Cav1 (Fig. 1a). Accordingly, STAT3 nuclear translocation was inhibited by stretch in WT (Fig. 1b,d) but not $\mathrm{Cav1}^{-/-}$ cells (Fig. 1c,d), whereas STAT1 nuclear translocation remained unaffected (Fig. 1b–d). These data indicate that caveolae and/or Cav1 selectively modulate STAT3 phosphorylation in response to mechanical stress.

### Interaction of Cav1 with JAK1 results in STAT3 inhibition

IFNα signalling depends on the ubiquitous IFNAR receptor, composed of two receptor subunits, IFNAR1 and IFNAR2, and downstream tyrosine kinases TYK2 and JAK1, which are respectively associated with IFNAR1 and IFNAR2 (refs. 54,55). We hypothesized that caveolae/Cav1 regulate STAT3 activation via interaction with JAK1 or TYK2. Hypo-osmotic shock (30 mOsm, 5 min), which increases membrane tension and rapidly disassembles caveolae, similarly to cell stretching[43], resulted in enhanced Cav1–JAK1 interaction up to threefold (Fig. 2a). This effect was rapid, with increased interaction correlated with the intensity of the shock and plateaued at 5 min (Fig. 2b,c). This increase correlated with a substantial reduction of STAT3 phosphorylation by ~62% (Fig. 2d). Upon return to iso-osmotic conditions, wherein caveolae are reassembled to their initial numbers[43], both Cav1–JAK1 interaction and IFNα-induced STAT3 phosphorylation reverted to baseline. $\mathrm{Cav1}^{-/-}$ cells showed elevated STAT3 phosphorylation, consistent with Cav1-mediated inhibition[56,57]. Thus, Cav1 released during caveolae disassembly regulates the extent of Cav1–JAK1 interaction and STAT3 activation in a reversible, tension-dependent manner.

### Mechanical stress enhances diffusion of Cav1 oligomers at the plasma membrane

We had initially hypothesized that the disassembly of caveolae induced by increased membrane tension would release non-caveolar caveolins at the plasma membrane and coat proteins into the cytosol[43,49]. Indeed, single-molecule fluorescence analysis have now revealed that caveolae flattening results in the disassembly of the cavin coat structure[43,58]. In addition, we previously showed that mechanical disassembly of caveolae releases the EHD2 ATPase from the neck of caveolae, which then translocates to the nucleus and regulates gene transcription[59]. Upon mechanical disassembly of caveolae, caveolins could remain as a flat caveolar structure, as shown by deep-etch EM[43], or released as non-caveolar Cav1 oligomers. In this regard, the comprehension of the topology of Cav1 oligomers released upon caveolae flattening is crucial for understanding the functions of caveolae, which is still limited. Indeed, FRAP experiments allowed us to show an increased mobile fraction of Cav1 upon mechanical stress, suggesting that a higher number of Cav1 molecules are freely diffusing outside caveolae[43]. To monitor the fate of single Cav1 molecules with high spatiotemporal resolution at the plasma membrane, we performed single-particle tracking coupled with photoactivation localization microscopy (sptPALM) using total internal reflection fluorescence microscopy (TIRF) and photo-switchable mEos3.2-Cav1 (refs. 60–62). Thousands of reconstructed mEos3.2-Cav1 trajectories were sorted according to their diffusion mode (diffusive, confined or immobile; Fig. 3a) and diffusion coefficients ($D$) were computed (Fig. 3b and Methods).

In resting cells, most Cav1 trajectories were immobile, consistent with confinement in caveolae (Fig. 3a,b and Supplementary Video 1). Acute increase in membrane tension through hypo-osmotic shock induced a marked increase in the fraction of fast freely diffusive trajectories (Fig. 3a,b and Supplementary Video 2), which increased with the duration of the hypo-osmotic shock (Fig. 3c), in agreement with the visualization that mEos3.2-Cav1 trajectories explored a wider area with time. Upon return to iso-osmotic conditions (recovery), the fraction of diffusive Cav1 decreased to those of the resting state (Fig. 3d). Diffusion of a plasma membrane control (CAAX-mEos3.2) was unchanged (Extended Data Fig. 2a). These results indicate that Cav1 molecules, initially immobilized within caveolae, are released into a dynamic and reversible diffusive pool in response to mechanical stress.

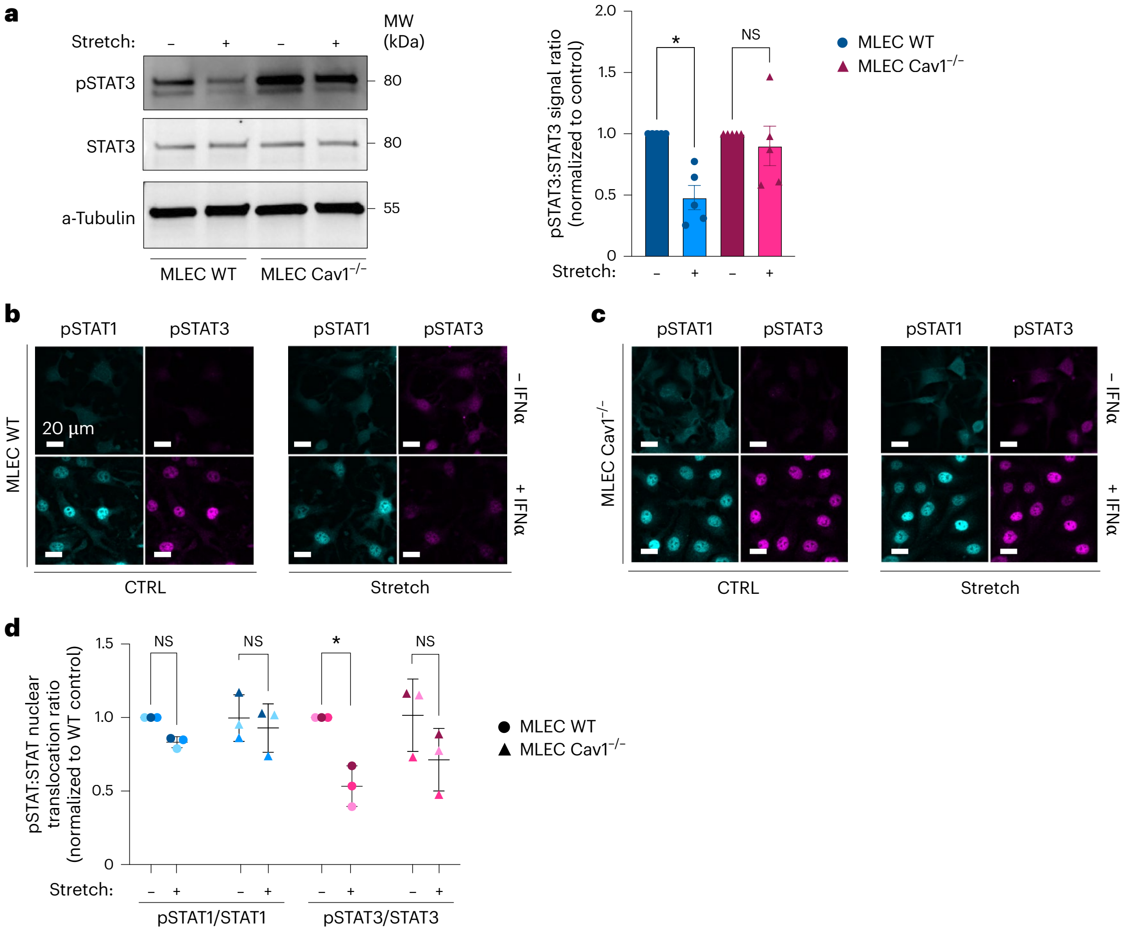

**Fig. 1 | Caveolae mechanics modulate the JAK–STAT signalling pathway.** **a**, Representative immunoblots showing IFNα-induced STAT3 phosphorylation in MLEC WT and MLEC Cav1$^{-/-}$ cells subjected or not to uniaxial stretch, together with quantification of the pSTAT3/STAT3 signal ratio normalized to the corresponding unstretched control condition. Data are presented as mean ± s.e.m.; dots represent five independent biological replicates ($n = 5$). Statistical significance was assessed using one-way analysis of variance (ANOVA) with Friedman test; exact $P$ values are provided in the Source Data. **b**,**c**, Representative immunofluorescence (IF) images showing nuclear translocation of pSTAT1 and pSTAT3 in MLEC WT (**b**) and MLEC Cav1$^{-/-}$ (**c**) cells subjected or not to uniaxial stretch, in the absence or presence of IFNα. Images are representative of three independent biological replicates ($n = 3$) with similar results. Scale bars, 20 µm. **d**, Quantification of pSTAT1/STAT1 and pSTAT3/STAT3 nuclear translocation ratios, normalized to the unstretched MLEC WT control. Data are presented as mean ± s.e.m.; symbols represent three independent biological replicates ($n = 3$). Statistical significance was assessed using two-way ANOVA with Šídák's multiple-comparisons test (two-sided). Exact $P$ values are provided in the Source Data; $P < 0.05$; NS, not significant. Source numerical data and unprocessed blots are available in source data.

## Cav1 oligomers interact with JAK1 to modulate the JAK–STAT pathway

Differentiating between the functions of caveolae and caveolin oligomers has been a persistent challenge in the field of caveolae biology[1,2,39,63]. To distinguish caveolar versus non-caveolar Cav1, we used mouse embryonic fibroblasts (MEFs) knocked out for the *PTRF* gene encoding Cavin1 (Cavin1$^{-/-}$ MEFs), which lack caveolae and display mobile Cav1 (refs. 9,42). These cells showed increased diffusive Cav1 (Fig. 3e, g, h), similar to WT MEFs under osmotic stress (Fig. 3f,h). Re-expression of Cavin1 restored caveolae and reduced Cav1 diffusion to levels measured in resting WT cells (Fig. 3e–h). We next investigated the impact of Cav1 diffusion on JAK/STAT signalling. Notably, IFNα failed to activate STAT3 in Cavin1$^{-/-}$ cells but was rescued by Cavin1 re-expression (Fig. 3i). In Cavin1$^{-/-}$ cells expressing different levels of Cav1 oligomers, STAT3 activation inversely correlated with Cav1 levels (Fig. 3j). These data indicate that non-caveolar Cav1 mediates STAT3 inhibition.

## Nanoscale imaging of Cav1 oligomers under mechanical stress

Super-resolution microscopy and machine learning have provided new insights into the nanoscale organization of the plasma membrane[64–69]. Stochastic optical reconstruction microscopy (STORM) imaging of endogenous Cav1 and Cavin1 in MLEC cells revealed caveolae-sized circular structures with an apparent diameter of 50–100 nm, consistent with the known size of caveolae (Fig. 4a and Extended Data Fig. 3a,b). The use of an astigmatic lens with HILO illumination further enabled three-dimensional (3D) visualization (Extended Data Fig. 3c). Caveolae disassembly during hypo-osmotic shock likely proceeds via flattening before coat release[40]. Accordingly, Cav1-positive structures increased in diameter and area during shock and returned to baseline upon recovery (Extended Data Fig. 3a).

Cav1 oligomers have been proposed to assemble into Cav1 scaffolds, outside caveolae[39]. However, these scaffolds are too small to be visually detectable using conventional fluorescence microscopy or EM techniques. Recently, computational network modelling and machine-learning-based 3D pattern analysis applied to single-molecule localization microscopy (SMLM) data enabled the identification of caveolae and three distinct classes of Cav1 scaffolds[40]. The classification was achieved using weakly supervised machine learning through cluster-based feature analysis, considering various parameters including size, shape, topology, hollowness, network characteristics and oligomerization state. The smallest S1A scaffold corresponds to the known 8S complex of SDS-resistant 11 Cav1

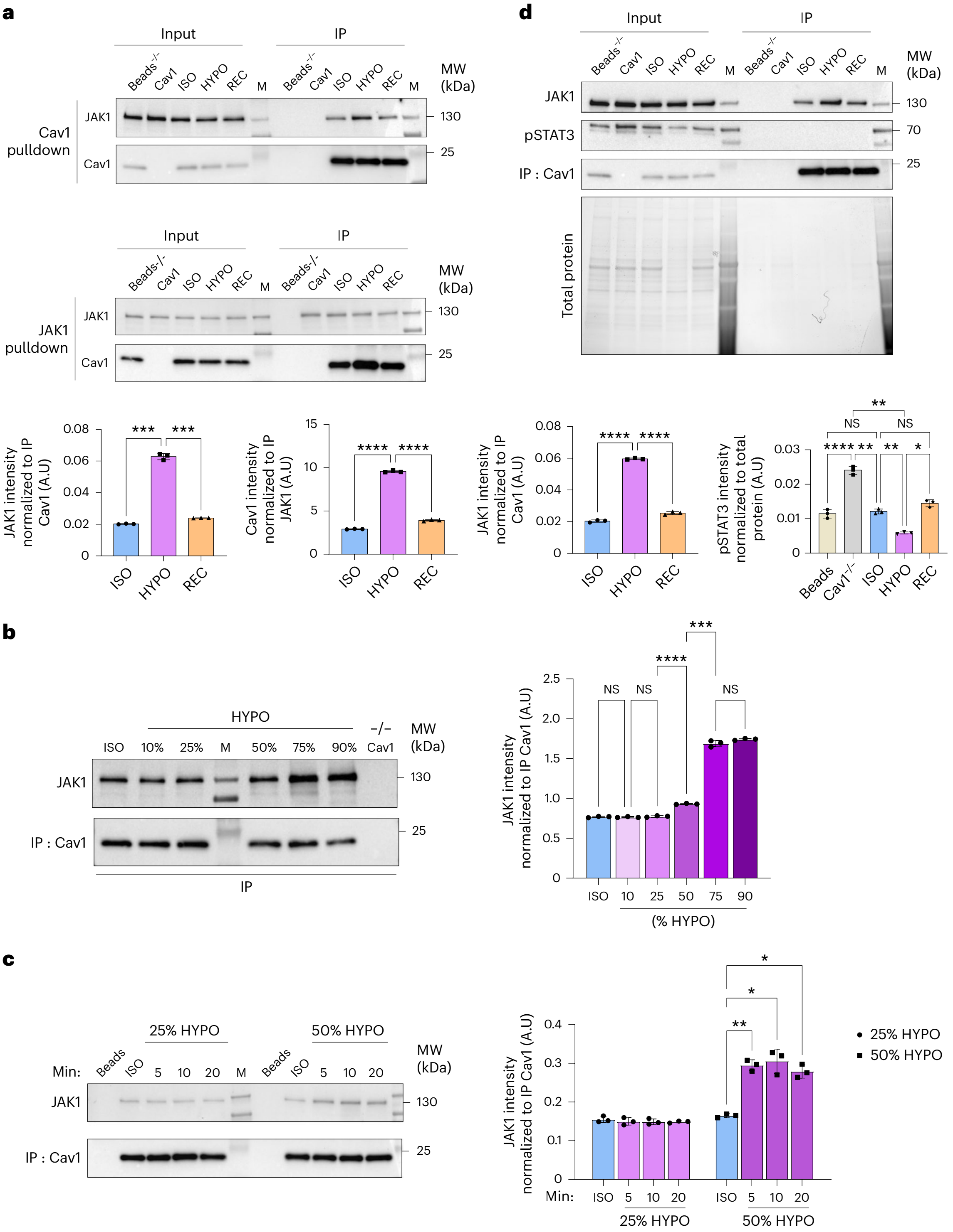

**Fig. 2 | Cav1-dependent inhibition of STAT3 activation is mediated through JAK1 association. a**, Representative reciprocal co-immunoprecipitation of endogenous Cav1 and JAK1 from MLEC WT cells under iso-osmotic (ISO), hypo-osmotic (HYPO) and recovery (REC; return to ISO medium after HYPO) conditions. Quantification is based on the signal intensity ratio of JAK1 relative to immunoprecipitated Cav1 and, conversely, Cav1 relative to immunoprecipitated JAK1. **b**, Representative co-immunoprecipitation of endogenous JAK1 with Cav1 in MLEC WT cells under ISO and increasing percentages of HYPO. Quantification is based on the JAK1–Cav1 signal intensity ratio in the immunoprecipitated fraction. **c**, Representative co-immunoprecipitation of endogenous JAK1 with Cav1 in MLEC WT cells under ISO and after increasing durations of 25% or 50% HYPO. Quantification is based on the JAK1–Cav1 signal intensity ratio in the immunoprecipitated fraction. **d**, Representative co-immunoprecipitation of endogenous JAK1 with Cav1 in MLEC WT cells under ISO, HYPO and REC, together with the corresponding IFNα-induced pSTAT3(Tyr705) levels. Quantification of JAK1 is based on the signal intensity ratio of JAK1 relative to immunoprecipitated Cav1. Quantification of pSTAT3(Tyr705) is based on the signal intensity ratio of pSTAT3(Tyr705) relative to total protein measured from the corresponding stain-free blot, shown below. For all panels, immunoblots are representative of three independent biological replicates ($n = 3$) with similar results. Quantified data are presented as mean ± s.d., with individual data points representing the independent biological replicates. Statistical significance was assessed using repeated-measures one-way ANOVA with multiple-comparisons correction; significance is indicated in the figure. Exact $P$ values are reported in the Source Data. $P < 0.05$, *$P < 0.01$, **$P < 0.001$, ***$P < 0.0001$; NS, not significant. Source numerical data and unprocessed blots are available in source data.

protomers, recently characterized by cryo-EM at 3.5 Å, which are the minimal building block required to assemble the 70S complex of budded caveolae[17,70,71]. S1B scaffolds are dimeric forms of S1A, whereas larger S2 scaffolds correspond to a hemispherical intermediate made of several S1A scaffolds[41]. In addition to identifying bona fide caveolae, our post-cluster segmentation of 3D STORM Cav1 localizations allowed the visualization of numerous S1A, S1B and S2 Cav1 scaffolds in resting WT MLECs (Fig. 4b). Based on previous estimates of ~144 ± 39 Cav1 molecules per caveola[72], and about thirteen 8S complexes or S1A scaffolds[17,41], we calculated that in resting cells ~49% of Cav1 resides in caveolae, whereas S2, S1B and S1A scaffolds account for ~30%, 14% and 7%, respectively; Supplementary Table 1). Upon 5 min of hypo-osmotic shock, caveolae decreased by ~34%, with a concomitant increase in scaffolds, particularly S1A (+20%) and S1B (+30%) (Fig. 4c, Extended Data Fig. 3d and Supplementary Table 2).

To validate these findings, we used DNA-based point accumulation for imaging in nanoscale topography (DNA-PAINT) to investigate the structural organization of the different Cav1 populations at rest and after cyclic stretching using a stretching device compatible with super-resolution microscopy[73]. DNA-PAINT relies on the stochastic binding of a fluorescent single-stranded DNA (imager strand) to the target-bound complement (docking strand) with sub-10-nm spatial resolutions[73]. To image Cav1, we used an anti-green fluorescent protein (GFP) nanobody that was functionalized with a DNA strand in MLEC Cav1$^{-/-}$ cells expressing Cav1–GFP. In resting cells, two broad and distinct distributions of nano-objects were detected: a larger population (~54%) of structures above 70 nm likely corresponding to caveolae and smaller structures below 70 nm likely corresponding to Cav1 scaffolds (~46%) (Fig. 4d). After cyclic stretching (30%, 0.5 Hz, 30 min), scaffolds increased to ~64% at the expense of caveolae (Fig. 4d and Extended Data Fig. 4a,b), consistent with 3D STORM experiments (Fig. 4c and Extended Data Fig. 3d). The size of the smallest detected structures (~25 nm) exceeds the experimental spatial resolution, suggesting that they correspond to S1A scaffolds and not individual caveolins. Altogether, these data show that membrane tension surges reduce caveolae and promote Cav1 scaffold formation.

## Preferential interaction of S1A and S1B Cav1 scaffolds with JAK1 under mechanical stress

We next investigated whether specific Cav1 scaffolds preferentially interact with JAK1. Multicolour 3D STORM with spectral demixing enabled the simultaneous localization of endogenous Cav1 and JAK1 (Extended Data Figs. 3b and 4c). We then applied machine learning and network features-based analysis to distinguish caveolae and Cav1 scaffold populations. Interaction analysis using MosaicIA[74] revealed a significant increase in JAK1 interaction with S1A and S1B scaffolds upon 5 min of hypo-osmotic shock, whereas interactions with caveolae and S2 scaffolds remained low and unchanged (Fig. 4e,f). We further quantified proximity between JAK1 and Cav1 scaffolds using Point Cloud Analyst-based clustering and centroid distance measurements between pairs of objects (JAK1–caveolae, JAK1–S2, JAK1–S1B and JAK1–S1A) (Fig. 4e and Extended Data Fig. 4d). The frequency of pairs at a centroid-to-centroid distance <100 nm within a defined region of interest (ROI) confirmed increased proximity between JAK1 and S1A/S1B scaffolds under stress (Fig. 4g). These data suggest that Cav1 is less accessible when assembled into caveolae or S2 scaffolds, whereas stress-induced S1A/S1B scaffolds are more diffusive and exposed.

## The caveolin scaffolding domain mediates the interaction between Cav1 and JAK1

STAT3 activation was inversely correlated with Cav1–JAK1 interaction, suggesting that Cav1 negatively regulates JAK1 activity. The CSD (NH$_2$-terminal residues 82–101) has been proposed to mediate interactions with a limited set of signalling proteins and exert inhibitory effects[29,30,75,76]. Expression of a Cav1 construct carrying CSD-inactivating point mutations at Phe92 and Val94 (Cav1–F92A/V94A-mRFP)[38] in MLEC Cav1$^{-/-}$ cells abolished co-immunoprecipitation with JAK1 (Fig. 5a).

We also monitored pSTAT1 and pSTAT3 nuclear translocation induced by IFNα stimulation in MLEC Cav1$^{-/-}$ cells re-expressing either Cav1 WT or Cav1–F92A/V94A (Fig. 5b). Expression of either construct had no effect on basal STAT3 levels (Extended Data Fig. 1b). pSTAT1 and pSTAT3 nuclear translocation levels were comparable between

**Fig. 3 | Upon osmotic shock, Cav1 is released from caveolae and undergoes lateral diffusion along the plasma membrane.** **a**, Top shows representative super-resolution PALM images of mEos3.2–Cav1 in MLEC WT cells under ISO conditions (left) and during HYPO (right), reconstructed from sptPALM acquisitions (50 Hz, >80 s). Insets show corresponding diffraction-limited images of coexpressed Cav1–GFP. Bottom shows colour-coded single-particle trajectories in the same cells, classified as diffusive (blue), confined (green) or immobile (red). Scale bars, 3 µm. **b**, Distribution of diffusion coefficient *D* computed from mEos3.2–Cav1 trajectories in MLEC WT cells under ISO (black) and HYPO (blue), shown on a logarithmic scale. The grey area corresponds to $D < 0.011$ µm$^2$ s$^{-1}$ and defines the immobile fraction. Middle shows box plots of diffusion coefficients for the freely diffusing trajectories. Right shows fractions of diffusive, confined and immobile trajectories. In **a** and **b**, data were obtained from single cells pooled from two independent biological experiments (MLEC WT ISO, $n = 9$ cells; MLEC WT HYPO, $n = 10$ cells). The distribution curves show the pooled trajectory data; box plots show the median (centre line/notch), mean (square) and box bounds corresponding to the 25th and 75th percentiles with whiskers extending to the minimum and maximum values. Where summary values are shown, data are presented as mean ± s.e.m. Statistical significance was assessed by ANOVA with multiple-comparisons correction (two-sided); exact *P* values are provided in the Source Data. **c**,**d**, Distribution of *D* computed from mEos3.2–Cav1 trajectories in MLEC WT cells during HYPO from $t = 0$ to 10 min (**c**) and after return from HYPO to recovery (REC) conditions from $t = 1$ to 30 min (**d**). Data were obtained from the same two independent biological experiments as in **a** and **b**. **e**, Representative super-resolution PALM images of mEos3.2–Cav1 in MEF Cavin1$^{-/-}$ cells (left; scaffolds) and MEF Cavin1$^{-/-}$ cells rescued with Cavin1–mEGFP (right; caveolae), reconstructed from sptPALM acquisitions (50 Hz, >80 s). Insets, Corresponding diffraction-limited images of mEos3.2–Cav1 (left) and Cavin1–mEGFP (right). Bottom, colour-coded trajectories classified as diffusive (blue), confined (green) or immobile (red). Scale bars, 3 µm. **f**, Distribution of *D* computed from mEos3.2–Cav1 trajectories in MEF WT cells under ISO (black) and HYPO (blue), shown on a logarithmic scale; the grey area corresponds to $D < 0.011$ µm$^2$ s$^{-1}$. **g**, Distribution of diffusion coefficient *D* computed from mEos3.2–Cav1 trajectories in MEF Cavin1$^{-/-}$ cells (blue) and MEF Cavin1$^{-/-}$ cells rescued with Cavin1–mEGFP (green). **h**, Box plots of diffusion coefficients for the freely diffusing trajectories and corresponding fractions of diffusive, confined and immobile trajectories in MEF WT ISO and HYPO, and in MEF Cavin1$^{-/-}$ cells with or without Cavin1–mEGFP rescue. In **e**–**h**, data were obtained from single cells pooled from two independent biological experiments (MEF WT ISO, $n = 8$ cells; MEF WT HYPO, $n = 8$ cells; MEF Cavin1$^{-/-}$, $n = 9$ cells; MEF Cavin1$^{-/-}$ + Cavin1–mEGFP, $n = 11$ cells). Box plots show the median (centre line/notch), mean (square) and box bounds corresponding to the 25th and 75th percentiles with whiskers extending to the minimum and maximum values. Where summary values are shown, data are presented as mean ± s.e.m. Statistical significance was assessed by ANOVA with multiple-comparisons correction (two-sided); exact *P* values are provided in the Source Data. **i**, Representative immunoblots showing STAT3 phosphorylation in MEF Cavin1$^{-/-}$ cells left untreated (NT) or rescued with Cavin1–mEGFP, at steady state (left) or after IFNα stimulation (right). Immunoblots are representative of three independent biological replicates with similar results. **j**, Representative immunoblots showing IFNα-induced STAT3 phosphorylation in MEF Cavin1$^{-/-}$ cells expressing low, medium or high levels of Cav1, together with quantification of the pSTAT3:STAT3 signal ratio normalized to the low-expression condition. Data are presented as mean ± s.e.m., with individual data points representing three independent biological replicates ($n = 3$). Statistical significance was assessed by ANOVA with multiple-comparisons correction (two-sided); exact *P* values are provided in the Source Data. ****$P < 0.0001$, ***$P < 0.001$, **$P < 0.01$, *$P < 0.05$; NS, not significant. Source numerical data and unprocessed blots are available in source data.

MLEC Cav1$^{-/-}$ cells expressing Cav1 WT and MLEC WT cells (Fig. 1d). In non-transfected cells, pSTAT3 nuclear translocation occurred normally; however, in cells overexpressing Cav1 WT, it was impaired, supporting an inhibitory role of Cav1 on JAK1 activity. In cells expressing Cav1–F92A/V94A, pSTAT3 nuclear translocation was restored upon IFNα stimulation, indicating that loss of STAT3 inhibition likely results from impaired JAK1 interaction (Fig. 5a,b). Consistent with STAT1 insensitivity to mechanical stress and caveolae, IFNα-induced pSTAT1 nuclear translocation remained unaffected regardless of Cav1 expression (Fig. 5b).

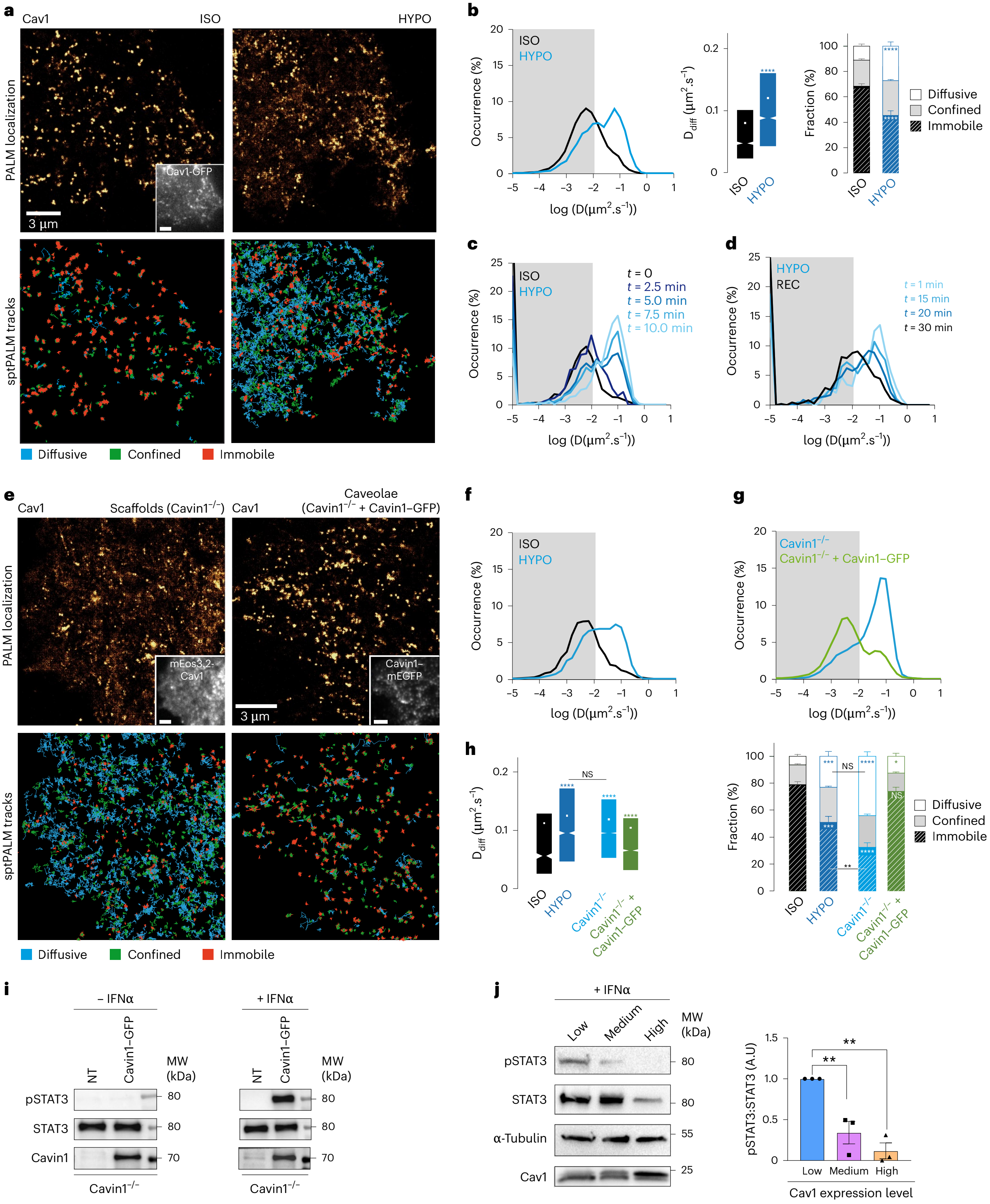

We further investigated CSD function using two peptides, CavTratin (Cav1 $^{82}$DGIWKASFTTFTVTKYWFYR$^{101}$) corresponding to Cav1–CSD and CavNoxin (Cav1 $^{82}$DGIWKASFAAATVTKYWFYR$^{101}$), in which key residues are replaced by alanines, abolishing inhibitory activity[77]. CavTratin treatment significantly reduced pSTAT3 levels upon IFNα stimulation compared with a scrambled control peptide (Fig. 6a), indicating that the CSD alone is sufficient to negatively regulate STAT3 activation. Conversely, CavNoxin increased IFNα-induced pSTAT3. Cav1 overexpression may generate non-caveolar Cav1 due to stoichiometric imbalance with caveolar components such as Cavin1 (refs. 37,71). Conversely, CavNoxin likely relieves JAK1 inhibition by competing with endogenous Cav1. To exclude indirect effects, we assessed CSD binding on JAK1 catalytic activity in a cell free assay. JAK1 activity, measured by ATP-to-ADP conversion, was unchanged with control peptide but decreased significantly and in a dose-dependent manner with CavTratin (Fig. 6b).

A caveolin binding motif has been proposed to mediate interactions with Cav1–CSD[78,79], though its role remains debated[80,81]. Sequence analysis of JAK1 identified three candidate motifs: within the FERM domain ($^{157}$YLFAQGQY$^{164}$), pseudo-kinase domain ($^{777}$WSFGTTLW$^{784}$) and tyrosine kinase domain ($^{1065}$WSFGVTLH$^{1072}$). The first was excluded as it is absent in the recombinant JAK1 used in vitro (Fig. 6b). Co-immunoprecipitation showed that residues 1057–1071, but not 1072–1154, are required for Cav1 interaction with JAK1 (Extended Data Fig. 5a). These data highlight the essential role of Cav1–CSD in mediating direct interaction with JAK1, likely via its tyrosine kinase domain, resulting in dose-dependent inhibition of JAK1 activity and downstream signalling.

These findings prompted structural investigation of Cav1 binding to JAK1. We used AF3 to model the complex[82], restricting JAK1 to its kinase domain (residues 855–1154) and using a series of Cav1 peptides encompassing residues 90–98 of the Cav1–CSD monomer. This choice was guided by our experimental observation that removal of JAK1 C-terminal region (residues 1057–1154) abolishes interaction with Cav1 (Extended Data Fig. 5a). We tested Cav1 peptides encompassing residues 90–98 because the Cav1–F92A/V94A mutant failed to interact with JAK1 (Fig. 5a,b). We chose to model Cav1 peptides rather than the full-length monomer because the cryo-EM structure of the Cav1 11-mer shows that residues 90–98 are not accessible for interactions with partner proteins such as JAK1 (PDB ID: 7SC0)[17]. Interactions likely require conformational rearrangement of Cav1, as suggested by coarse-grained MD simulations[83].

Long Cav1 sequences (≥71–121) adopted fully helical conformations resembling the cryo-EM structure of the Cav1 11-mer (PDB ID: 7SC0) and showed no credible interaction with JAK1. In contrast, shorter peptides (80–110) consistently yielded similar complex structures across five independent AF3 runs. Superimposition of these models revealed conserved positioning of residues 90–98 at the surface of the JAK1 kinase domain (Fig. 6c), with highly conserved side-chain orientations (Fig. 6d).

In these models, F92 and V94 insert into hydrophobic grooves at the surface of the JAK1 kinase domain (Fig. 6e). F92 occupies a hydrophobic cavity formed by JAK1 residues V1045, F1046, V1101 and the methyl group of T1100 (Fig. 6f), whereas V94 occupies a second hydrophobic pocket lined by residues Y1048, L1053 and V1045 (Fig. 6g). W98 forms a hydrogen bond via its HNε2 atom with the backbone carbonyl oxygen of Q1055 of the JAK1 kinase domain (Fig. 6g). No interactions were observed outside this core region. The importance of W98 was confirmed experimentally, as the Cav1-W98A mutant failed to bind JAK1 (Fig.6h).

Despite low confidence scores, as occasionally observed in AF3 predictions, we assessed interface stability using MD simulations in explicit solvent (~2.1 µs total). Simulations were initiated from the top-ranked AF3 model of the JAK1(855–1154)–Cav1(80–110) complex. The JAK1 kinase domain remained structurally stable with low Cα atom root-mean-square deviation (RMSD; <2.0 Å; Extended Data Fig. 5b–d) and low root-mean-square fluctuation (RMSF) values (1.0–2.0 Å; Extended Data Fig. 5e). In contrast, the Cav1(80–100) peptide showed higher flexibility overall (RMSD up to 8.0 Å; Extended Data Fig. 5b–d), but residues 90–98 remained stable (RMSD < 2.5 Å; RMSF < 2.0 Å), indicating a constrained core region (Extended Data Fig. 5f). Distal regions of the peptide underwent substantial conformational fluctuations relative to the JAK1 kinase domain, possibly due to the truncated peptide.

Minimum interatomic distance analysis further supported the stability of predicted interactions. Cav1 residue V94 consistently

**Fig. 4 | Nanoscale visualization of Cav1 organization and its remodelling in response to mechanical stress.** **a**, Representative two-dimensional (2D) single-colour dSTORM image of a MLEC WT cell stained for Cav1. Inset shows a higher-magnification view. Image is representative of three independent biological experiments with similar results. Scale bars, 1 µm; inset, 300 nm. **b**, Representative raw 2D STORM image and the corresponding post-cluster-segmentation image obtained after application of the 3D SMLM network-analysis pipeline used to classify Cav1 objects into caveolae and the three non-caveolar scaffold subclasses (S2, S1B and S1A). Images are representative of three independent biological experiments with similar results. Scale bars, 1 µm; insets, 300 nm. **c**, Quantification of the number of caveolae, S2, S1B and S1A Cav1 objects per 100 µm$^2$ in ISO and HYPO conditions from post-cluster-segmentation images acquired by 3D dSTORM. Data are presented as mean ± s.d., with individual data points representing ROIs used for statistical analysis ($n = 30$ ROIs per condition, corresponding to two ROIs per cell from 15 cells across three independent biological experiments). Statistical significance was assessed using a two-sided unpaired *t*-test. Exact *P* values are provided in the Source Data. **d**, DNA-PAINT images (top) of Cav1 in MLEC Cav1$^{-/-}$ cells re-expressing Cav1–GFP at steady state (CTRL) or after cyclic stretch (30% strain, 0.5 Hz, 30 min) on a polydimethylsiloxane stretching device. Middle, corresponding first-rank density maps generated with SR-Tesseler and normalized to the average localization density. Bottom, detected Cav1 clusters highlighted after segmentation. The boxed regions in the left panels are shown at higher magnification on the right. Images are representative of three independent biological experiments with similar results. The cluster-size distribution plot was generated from all segmented clusters pooled from three independent biological experiments (CTRL, $n = 1{,}929$ clusters; stretch, $n = 3{,}531$ clusters); bold lines indicate the mean. The bar plot shows the fraction of Cav1 clusters <70 nm and >70 nm. Data are presented as mean ± s.d. from three independent biological replicates ($n = 3$). Statistical significance was assessed using repeated-measures one-way ANOVA with multiple-comparisons correction (two-sided). Exact *P* values are provided in the Source Data. **e**, Representative 3D STORM visualization of JAK1 localizations and the different Cav1 object classes within a defined ROI under ISO (top) and HYPO (bottom) conditions. The corresponding segmented objects and extracted object centroids for the indicated Cav1–JAK1 pairs are shown on the right. Images are representative of 15 cells per condition acquired across three independent biological experiments with similar results. Scale bar, 3 µm; insets, 200 nm. **f**, Object-based spatial interaction analysis (MOSAIC suite, Fiji) showing the interaction strength (A.U.) between JAK1 and each Cav1 object class (caveolae, S2, S1B and S1A) under ISO and HYPO conditions. Data are presented as mean ± s.d., with individual data points representing ROIs ($n = 30$ ROIs per condition, corresponding to two ROIs per cell from 15 cells across three independent biological experiments). Statistical significance was assessed using repeated-measures one-way ANOVA with multiple-comparisons correction (two-sided). Exact *P* values are provided in the Source Data. **g**, Percentage occurrence of JAK1 objects located <100 nm or >100 nm from the indicated Cav1 object classes (caveolae, S2, S1B and S1A) under ISO and HYPO conditions. Data were obtained from ROIs ($n = 30$ ROIs per condition, corresponding to two ROIs per cell from 15 cells across three independent biological experiments) and are presented as mean ± s.d. Statistical significance was assessed using repeated-measures one-way ANOVA with multiple-comparisons correction (two-sided). Exact *P* values are provided in the Source Data. ****$P < 0.0001$, ***$P < 0.001$, **$P < 0.01$, *$P < 0.05$; NS, not significant.

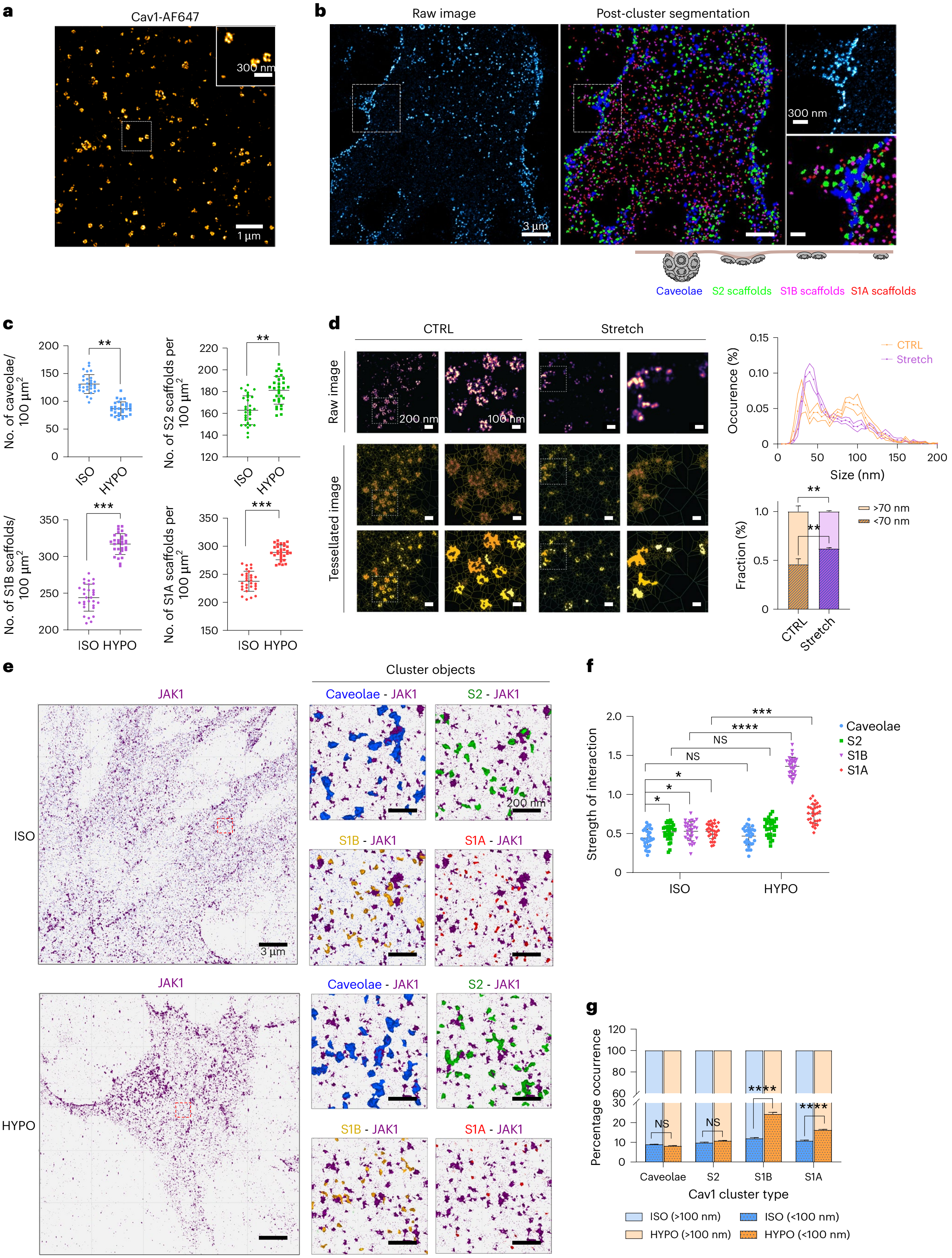
a
Cav1-AF647
300 nm
1 µm
b
Raw image
Post-cluster segmentation
3 µm
300 nm
Caveolae
S2 scaffolds
S1B scaffolds
S1A scaffolds
c
No. of caveolae/ 100 µm$^2$
200
150
100
50
0
**
ISO
HYPO
No. of S2 scaffolds per 100 µm$^2$
220
200
180
160
140
120
**
ISO
HYPO
No. of S1B scaffolds/ 100 µm$^2$
350
300
250
200
***
ISO HYPO
No. of S1A scaffolds per 100 µm$^2$
350
300
250
200
150
***
ISO HYPO
d
CTRL
Stretch
Raw image
200 nm
100 nm
Tessellated image
Occurence (%)
0.15
0.10
0.05
0
CTRL
Stretch
0
50
100
150
200
Size (nm)
Fraction (%)
1.0
0.5
0
**
**
>70 nm
<70 nm
CTRL
Stretch
e
Cluster objects
JAK1
Caveolae - JAK1
S2 - JAK1
ISO
3 µm
200 nm
S1B - JAK1
S1A - JAK1
JAK1
Caveolae - JAK1
S2 - JAK1
HYPO
S1B - JAK1
S1A - JAK1
f
Strength of interaction
2.0
1.5
1.0
0.5
0
***
****
NS
NS
*
*
*
ISO
HYPO
Caveolae
S2
S1B
S1A
g
Percentage occurrence
120
100
80
60
30
20
10
0
NS
NS
****
****
Caveolae
S2
S1B
S1A
Cav1 cluster type
ISO (>100 nm)
ISO (<100 nm)
HYPO (>100 nm)
HYPO (<100 nm)

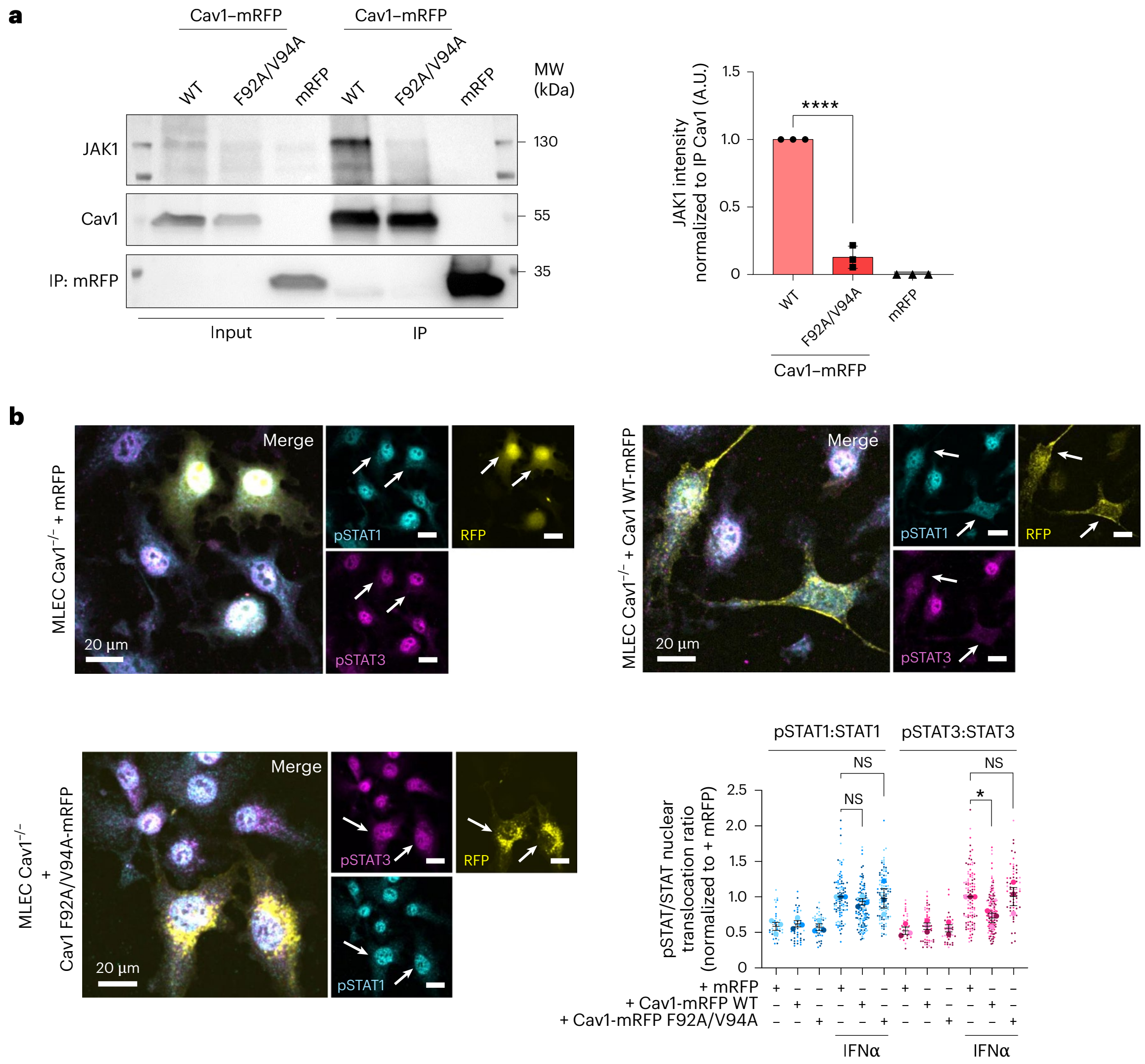

**Fig. 5 | Cav1–JAK1 association requires the caveolin scaffolding domain.** **a**, Representative RFP-trap co-immunoprecipitation from MLEC Cav1$^{-/-}$ cells expressing mRFP, Cav1-WT–mRFP, or Cav1-F92A/V94A–mRFP, with quantification of JAK1 signal intensity normalized to immunoprecipitated mRFP/Cav1–mRFP. Immunoblots are representative of three independent biological experiments with similar results. Quantified data are presented as mean ± s.e.m. (bars, mean; error bars, s.e.m.), with individual data points representing three independent biological replicates ($n = 3$). Statistical significance was assessed using a two-sided one-way ANOVA with multiple-comparisons correction. Exact *P* values are indicated in the figure and provided in the Source Data. **b**, Representative IF images showing nuclear translocation of pSTAT1(Tyr701) (cyan) and pSTAT3(Tyr705) (magenta) in IFNα-stimulated MLEC Cav1$^{-/-}$ cells expressing mRFP, Cav1(WT)–mRFP or Cav1(F92A/V94A)–mRFP (yellow). Images are representative of three independent biological experiments with similar results. Scale bar, 20 µm. Quantification of the pSTAT1/STAT1 and pSTAT3/STAT3 nuclear translocation ratios, normalized to the mRFP control, is presented as mean ± s.e.m. (bars, mean; error bars, s.e.m.), with individual data points representing three independent biological replicates ($n = 3$). Statistical significance was assessed using a two-sided one-way ANOVA with multiple-comparisons correction. Exact *P* values are indicated in the figure and provided in the Source Data. ****$P < 0.0001$, *$P < 0.05$; NS, not significant. Source numerical data and unprocessed blots are available in source data.

interacted with JAK1 residues V1045, Y1048 and L1053 along the three trajectories, consistent with persistent hydrophobic packing (Extended Data Fig. 5g–i). F92 remained constantly close to key JAK1 residues in two trajectories, with partial rearrangement in the third (Extended Data Fig. 5j–m). Likewise, the W98- Q1055 hydrogen bond was stable in trajectory 3 (Extended Data Fig. 5n), but fluctuated in trajectories 1 and 2, suggesting that this residue may exist in equilibrium between multiple confirmations (Extended Data Fig. 5n).

Together, these results support the AF3 model and indicate that Cav1 likely binds JAK1 via residues 90–98, with V94 being at the core and forming a key interaction with a set of hydrophobic JAK1 residues. This structural model fully agrees with biochemical data and underscores the central role of this Cav1 region in JAK1 binding.

## Multiple signalling pathways are controlled by the mechanical release of Cav1

We next examined whether additional signalling pathways are regulated by this mechanism using reverse-phase protein array (RPPA), which is a miniaturized dot-blot technology that enables proteomic analysis and identification of activated or altered signalling pathways[84]. Analysis of WT and Cav1$^{-/-}$ MLECs under uniaxial stretch (Extended Data Fig. 6a) revealed modulation of MAPK (p42/44) and AKT (pSer473) pathways. MAPK activation by stretch was Cav1-independent, whereas AKT pSer473 increase required Cav1 (Extended Data Fig. 6b). IFNα/β stimulation significantly increased STAT3 (Tyr705) and STAT1 (Tyr701) phosphorylation (Extended Data Fig. 6c). RPPA confirmed that stretching reduced STAT3 phosphorylation in a Cav1-dependent manner, with no effect on

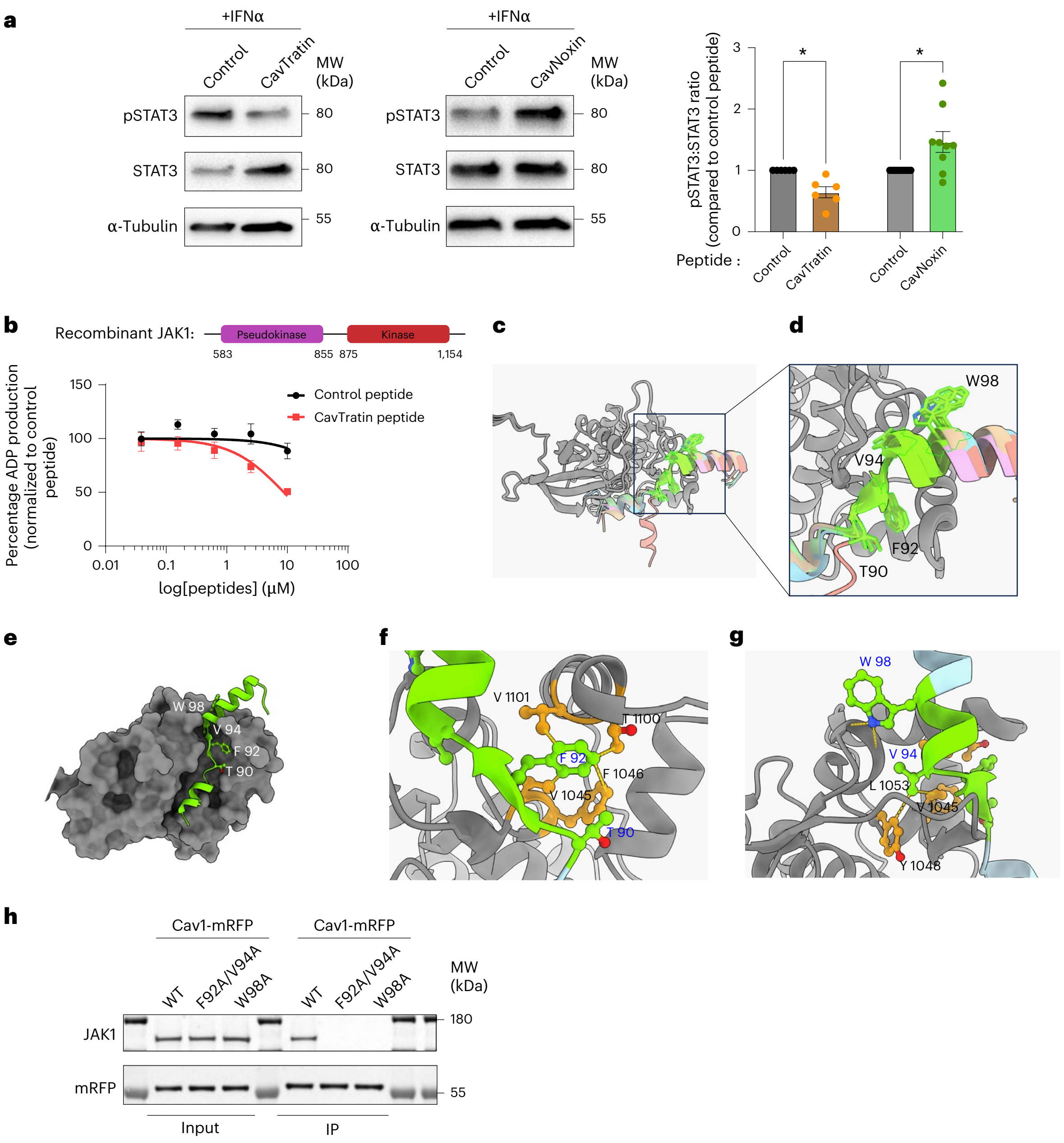

**Fig. 6 | Predicted Cav1–JAK1 complex structure and functional validation of the interaction interface. a**, Representative immunoblots showing pSTAT3(Tyr705) and total STAT3 in MLEC WT cells stimulated with IFNα in the presence of control peptide or CavTratin (left) and control peptide or CavNoxin (right), with the corresponding quantification of the pSTAT3:STAT3 ratio normalized to the respective control peptide condition. Immunoblots are representative of six independent biological replicates for CavTratin and nine independent biological replicates for CavNoxin, with similar results. Quantified data are presented as mean ± s.e.m. (bars, mean; error bars, s.e.m.), with individual data points representing the independent biological replicates (CavTratin, $n = 6$; CavNoxin, $n = 9$). Statistical significance was assessed using a two-sided Wilcoxon matched-pairs signed-rank test. Exact *P* values are indicated in the figure and provided in the Source Data. **b**, In vitro ADP production from ATP conversion by recombinant JAK1 plotted as a function of peptide log concentration (μM). Data are presented as mean ± s.e.m. (symbols/line, mean; error bars, s.e.m.) from three independent in vitro technical replicate experiments ($n = 3$). Statistical comparison of the fitted dose–response curves was performed using an extra-sum-of-squares *F* test (two-sided). Exact *P* values are indicated in the figure and provided in the Source Data. **c**, Superimposition of the five AF3-predicted structures of the JAK1(855–1154) kinase domain in complex with the Cav1(80–110) peptide, shown in cartoon representation. JAK1(855–1154) is shown in grey in all models, whereas Cav1(80–110) is shown in different colours for each model, except for the Cav1(90–98) segment, highlighted in green in all five structures. **d**, Superimposition of the side-chain conformations of Cav1 residues T90, F92, V94 and W98 in the five AF3-predicted models. **e**, Top-ranked AlphaFold3-predicted structure of the JAK1(855–1154)–Cav1(80–110) complex. JAK1 is shown in surface representation (grey) and the Cav1 peptide is shown in cartoon representation (green). Side chains of Cav1 T90, F92, V94 and W98 are shown in ball-and-stick representation and coloured by heteroatom. **f**, Close-up view of the JAK1 residues forming the predicted binding pocket for Cav1-F92 in the AF3 model. **g**, Close-up view of the predicted interactions of Cav1–V94 and Cav1–W98 with the JAK1 kinase domain. In **f**,**g**, JAK1 is shown in cartoon representation with side chains shown as orange ball-and-stick, and the Cav1 peptide is shown in green. **h**, Representative co-immunoprecipitation of Cav1–mRFP with endogenous JAK1 in MLEC Cav1$^{-/-}$ cells expressing Cav1(WT)–mRFP, Cav1(F92A/V94A)–mRFP or Cav1(W98A)–mRFP under ISO conditions. Immunoblots are representative of three independent biological experiments with similar results. Source numerical data and unprocessed blots are available in source data.

https://doi.org/10.1038/s41556-026-01966-0

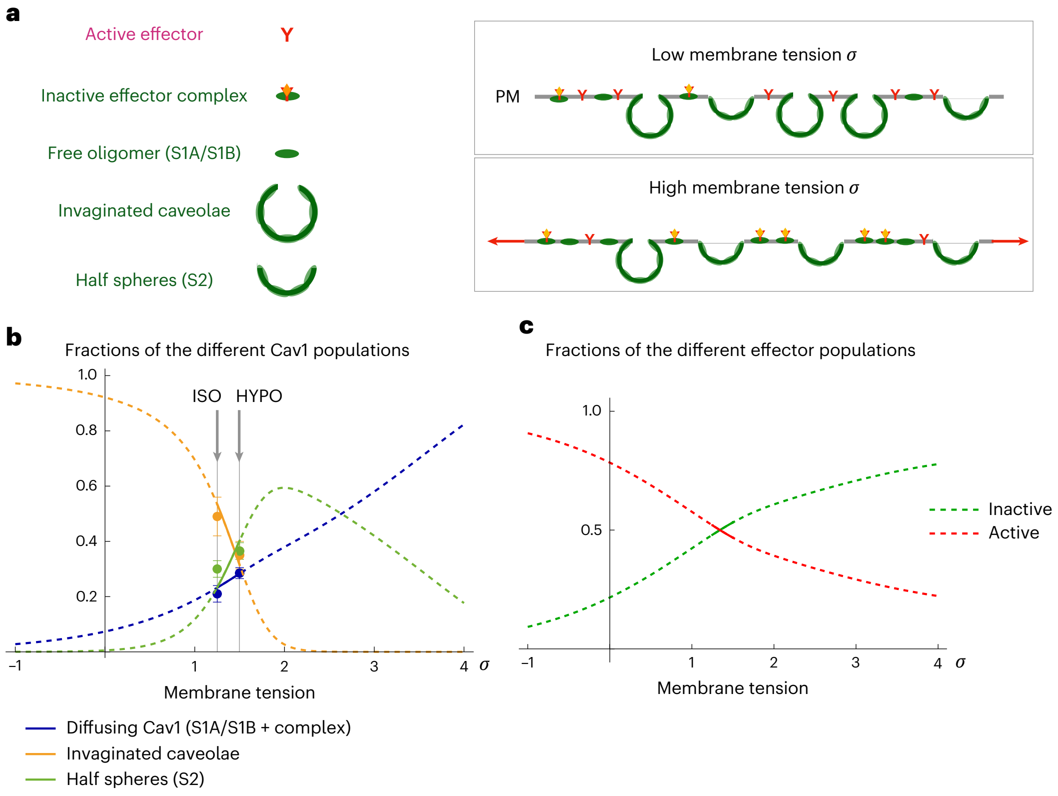

**Fig. 7 | Physical model of caveolae remodelling and effector regulation under membrane tension. a**, Schematic representation of the Cav1 and membrane-associated signalling-effector states included in the physical model: free S1A/S1B oligomers, hemispherical S2 domains, fully formed caveolae, active effectors and Cav1-bound inactive effector complexes. A sketch of the model is shown at right. **b**, Model-predicted variation in the fractions of the three Cav1 populations as a function of membrane tension. The blue line represents the sum of all diffusive Cav1 states. **c**, Model-predicted variation in the fractions of active and inactive membrane-associated signalling effectors as a function of membrane tension. In **b**,**c**, solid lines indicate the tension range explored experimentally in the stretching assays, whereas dashed lines indicate the model extrapolation over a broader range of membrane tension. Data points in **b** are derived from the experimental measurements shown in Fig. 4f. Model parameters are $e_b = 3.6$, $\lambda = 1.76$, $\rho_{tot} = 0.33$, $\varepsilon = 2.6$, $\rho_{(j,tot)} = 0.02$.

STAT1 (Extended Data Fig. 6d). We also analysed interactions between Cav1 and endothelial nitric oxide synthase (eNOS) as well as protein tyrosine phosphatase 1B (PTP1B)[31,85]. Both interactions increased during hypo-osmotic shock and returned to baseline upon recovery (Extended Data Fig. 7a). As observed for JAK1 (Fig. 2b,c), there is a correlation between the hypo-osmotic shock strength and the extent of interaction (Extended Data Fig. 7b), likely reflecting Cav1 release from disassembled caveolae. Similarly, this effect was rapid, with maximal interaction reached within 5 min of hypo-osmotic shock and no further increase upon prolonged exposure (Extended Data Fig. 7c). Increased Cav1–eNOS interaction reduced eNOS activation (Ser1177 phosphorylation; Extended Data Fig. 7d)[86]. Return to iso-osmotic conditions restored baseline eNOS–Cav1 interaction and eNOS activation. No effect was observed in Cav1$^{-/-}$ cells.

Cav1 also interacted with phosphatase and tensin homologue (PTEN), a potent tumour suppressor and negative regulator of AKT signalling[87] (Extended Data Fig. 8a). Hypo-osmotic shock increased Cav1 binding to PTEN, correlating with enhanced AKT Ser473 phosphorylation. These data remain, however, correlative, and we can only speculate that the increase in AKT activity, also observed by RPPA in stretched cells (Extended Data Fig. 6b), reflects inhibition of PTEN phosphatase activity by Cav1, particularly as AKT does not interact with Cav1 (Extended Data Fig. 8b). Of note, we found that as observed for JAK1, Cav1 interaction with PTEN required residues F92, V94 and W98 of the Cav1–CSD domain (Extended Data Fig. 8b). Similar to JAK1, eNOS and PTP1B, the Cav1–PTEN interaction returned to basal levels upon restoration of iso-osmotic conditions (Extended Data Fig. 8a). Finally, Cav1 did not interact with TYK2, another JAK family member activated by IFNα (Extended Data Fig. 8b). Although caveolin and integrins cooperate in mechanosignalling[88], as we recently showed in invadosome biogenesis and activity[89]. However, we could not immunoprecipitate integrins with Cav1 in MLEC cells (Extended Data Fig. 8c). These results establish the selectivity of caveolae mechanosignalling.

## Physical model of caveolae formation under mechanical stress

We developed a thermodynamic model of caveolae self-assembly (Supplementary Note 1)[90]. The theoretical model includes full caveolae, hemispherical S2 scaffolds and smaller S1A/B scaffolds (Fig. 7a). Minimization of the system's free energy yields a membrane tension-dependent fraction of the total Cav1 population in the different states, which is proportional to

$$\text{caveolae}: \rho_{\text{full}} = n\, e^{n(\mu_c + e_b - \sigma)}, S2: \rho_{\text{half}} = \frac{n}{2} e^{\frac{n}{2}\left(\mu_c + e_b + \lambda - \frac{\sigma}{2}\right)}, S1: \rho_1 = e^{\mu_c} \tag{1}$$

where σ is the membrane tension, $e_b$ is the binding energy between S1 scaffolds in larger domains (caveolae and S2), $\lambda$ is the line tension associated with the boundaries of S2 domains, $n = 13$ is the number of S1 in caveolae and $\mu_c$ is the Cav1 chemical potential, obtained from the conservation of the total number of Cav1 at the membrane (see below). The energetic parameters are normalized to be expressed in unit of the thermal energy $k_B T$.

The model predicts a sigmoidal decrease of caveolar Cav1 and increase of freely diffusing Cav1 with membrane tension (Fig. 7b). Hemispherical S2 domains exist within a limited tension range strongly depending on S2 line tension. Parameters of Fig. 7b were fitted to match super-resolution data (Fig. 4b,e). The fit, although not unique, suggests that the membrane tension homeostatic value is within the range that permits substantial variation of free Cav1 under stretch. Free Cav1 may interact with and inactivate membrane-associated signalling effectors. This is described within the same framework, where the population of effectors in the different states is proportional to

$$\text{active} : \rho_j = e^{\mu_j}, \ \text{inactive (bound to Cav1)} : \rho_d = e^{\mu_j+\varepsilon+\mu_c} \qquad (2)$$

where  is the binding energy between S1 and effectors and $\mu_j$ is the effector chemical potential. The two chemical potentials are obtained from the conservation of the total number of the respective proteins at the membrane: $\rho_1 + \rho_d + \rho_{full} + \rho_{half} = \rho_{tot}$ and $\rho_j + \rho_d = \rho_{j,tot}$. Increased membrane tension promotes effector inactivation via Cav1 release from caveolae and S2 aggregates (Fig. 7c). A more complete model (Supplementary Note 1) allowing multiple bindings on free Cav1 oligomers does not alter these conclusions (Fig. 7b,c). Overall, this model, based on equilibrium thermodynamics, quantitatively explains how membrane tension controls Cav1 states and signalling, consistent with our experimental observations and predictive across a broad tension range.

## Discussion

Since their first description in 1953, research over the years has revealed a variety of roles for caveolae and caveolins in preserving biological functions (reviewed previously[2,22]). Although studies in the mid-1970s suggested roles in mechano-protection and cellular integrity[91–93], it was only after the demonstration that caveolae sense and respond to mechanical stress that the field reassessed their classical functions in the context of cell mechanics[2,43,50–52]. We initially hypothesized that caveolar components released upon mechanical disassembly could mediate the mechanical response of the cell[49]. Indeed, we could demonstrate that increased membrane tension triggers translocation of the ATPase EHD2 from the neck of caveolae to the nucleus, where it regulates gene transcription[59]. Similarly, Cavin1 is released from the caveolar coat upon hypo-osmotic shock[43,58,94], and Cavin3 can interact with BRCA1 to regulate cancer-related pathways following caveolae disassembly induced by UV or osmotic stress[95].

Our findings reveal that mechanical stress significantly augments the extent of Cav1 interaction with JAK1, PTEN, PTP1B and eNOS. Together with the proposed role of non-caveolar Cav1 scaffolds in signalling[39], this supports a model in which Cav1 released from mechanically disassembled caveolae mediates these interactions. sptPALM microscopy revealed that the population of non-diffusive Cav1 particles, initially constrained to confined domains under low membrane tension (likely caveolae), transitioned significantly as membrane tension progressively increased. This transition was characterized by a diffusion pattern indicative of Cav1 scaffolds scattering upon caveolae disassembly, accompanied by an increased population of freely diffusing Cav1 and an increase in their diffusion coefficient. In Cavin1$^{-/-}$ cells where only non-caveolar Cav1 is present, we measured a diffusion coefficient for Cav1 particles that was strictly identical to the higher diffusion coefficient induced by osmotic stress in WT cells. These observations confirm that the highly diffusive pool of Cav1 molecules corresponds to non-caveolar Cav1. Similarly, we established a direct correlation between the level of inhibition of STAT3 phosphorylation and the quantity of non-caveolar Cav1.

Super-resolution imaging and network analysis have identified distinct subclasses of non-caveolar Cav1 or scaffolds that act as building blocks of caveolae[41]. Analysis of our SMLM data indicates that mechanical stress promotes caveolae disassembly into Cav1 scaffolds. This disassembly was strongly correlated with an increase in both Cav1 diffusion and its interaction with signalling effectors. These observations establish a mechanistic link between caveolae disassembly, scaffold release and signalling output.

Structural modelling and MD simulations identified a plausible Cav1–JAK1 complex conformation in which Cav1 residue V94 forms the core of a motif that inserts into a cleft on the JAK1 surface. Residues F92 and W98 flank V94 and likely stabilize this interaction, as confirmed by targeted mutagenesis. This model is consistent with results obtained using the JAK1Δ(1057–1154) and JAK1Δ(1072–1154) truncation mutants. Residues 1057–1071 form a helix (highlighted in red in Extended Data Fig. 5o and Supplementary Video 3) that supports much of the Cav1 binding site (residues 1033–1055, highlighted in cyan in Extended Data Fig. 5o and Supplementary Video 3). Accordingly, removal of residues 1072–1154 (highlighted in orange in Extended Data Fig. 5o and Supplementary Video 3) is predicted to preserve sufficient binding interface for peptide interaction, albeit with altered affinity, whereas deletion of the 1057–1071 helix would disrupt the binding site and prevent Cav1 association with the JAK1 kinase domain. These findings indicate that the Cav1(90–98) segment within the Cav1–CSD is required for functional engagement of Cav1 and support a direct role for this domain in JAK1 binding.

The functionality of Cav1–CSD has been debated, as it has been proposed based on Cav1 sequence alignment, that this hydrophobic motif is embedded in the lipids of the plasma membrane, thus preventing direct physical interactions with cytosolic proteins[80,96]. The preferential interaction of Cav1 scaffolds, as opposed to caveolae, with signalling molecules during periods of mechanical stress provides a potential explanation for the involvement of the Cav1–CSD. Indeed, cryo-EM structural characterization of the Cav1–8S complex has offered new insights into this interaction[97,98]. Cryo-EM data show that the CSD is positioned at the outer rim of the 8S Cav1 discoid complex[17], suggesting that mechanical disassembly of caveolae into scaffolds, accompanied by lipid reorganization[81], could expose the CSD and render it accessible for binding to cytosolic proteins, which may be otherwise occluded in budded caveolae. Building on this notion, a recent study used the structure of the Cav1–8S complex to perform coarse-grain MD simulations of a single Cav1–8S embedded in lipid membranes of varying compositions[83]. These simulations revealed that the Cav1–8S complex preferentially localizes to highly curved membrane surfaces, resulting in the exposure of several Cav1–CSD residues, including T90, V94 and W98, to the aqueous environment. Our structural predictions further indicate a central role for Cav1 residue V94 in mediating interaction with the JAK1 kinase domain. Notably, the Cav1(90–98) segment, which adopts a helical conformation in the 8S Cav1 structure (PDB code 7SC0, ref. 17), adopts a markedly different conformation in the predicted JAK1 complex. Together, these observations support a model in which Cav1 undergoes a conformational transition from its 8S form, exposing residues F92, V94 and W98 of the Cav1–CSD and rendering them accessible for JAK1 binding. These data are also consistent with a recent study suggesting that the S2 and S1B Cav1 scaffolds exhibit a more exposed CSD with the surrounding molecular environment[99]. In addition, the simultaneous release of cavins from the caveola bulb, induced by mechanical stress, may also contribute to the enhanced accessibility of Cav1–CSD.

As the expression of cavin proteins seems limited to vertebrates, it has been proposed that caveolins can carry out their functions independently of caveolae in most organisms. Likewise, various cell types including neurons, lymphocytes, hepatocytes, and certain cancer cells do not express cavins, suggesting that caveolins may exert caveola-independent functions[63]. Early studies have reported the ability of Cav1 to interact with several effectors through the Cav1–CSD domain[29,30,75,76]. Using CSD-mimicking peptides and point mutations in the Cav1–CSD, we provide unequivocal evidence of the CSD requirement for the direct interaction between Cav1 and JAK1. Accordingly, it has been reported that the deletion of the CSD abolished the inhibition of STAT3 phosphorylation caused by Cav1 overexpression[100]. It is noteworthy that the CSD exhibits primary sequence similarities to the pseudo-substrate domain of SOCS1, which mediates JAK inhibition by SOCS1 (refs. 101,102). In this context, it is noteworthy that another member of the SOCS family, SOCS3, relies on Cavin1 for its localization at the plasma membrane in endothelial cells, and that STAT3 activation is increased when Cavin1 is depleted[103]. It will be interesting to test if, under mechanical stress, SOCS3 may be released from Cavin1, which would then compete with Cav1 scaffolds to bind to JAK1.

Superimposition of the AF3-predicted JAK1–Cav1 complex onto the cryo-EM structure of the JAK1 dimer (PDB ID: 8EWY)[104] provides additional mechanistic insight. In our model, the Cav1 peptide binds at the interface between the tyrosine kinase domains of the two JAK1 monomers. This interface, characterized by helical packing between the kinase domains, is thought to be critical for JAK1 dimerization, despite the presence of a secondary interface involving the pseudo-kinase domains, and is therefore likely essential for cytokine signalling. We speculate that Cav1 binding at this site could disrupt the interface or prevent of its formation, thereby modulating cytokine signal transduction mediated by JAK1 dimerization.

JAK1 inhibition was observed even in the absence of stimulation with IFNα, indicating that this regulatory process may be extended to other cytokines that activate JAK kinases. In the context of our previous study on interleukin (IL)-6–STAT3 signalling in human muscle cells, it is probable that the control exerted by caveolae mechanosensing on this signalling axis operates through the same mechanism[53]. It is notable that JAK1-dependent STAT3 activation was specifically targeted while leaving STAT1 activation unaffected. Our data indicate that TYK2, the other kinase operating in the IFNα signalling complex, does not interact with Cav1. These findings further support the dichotomy between STAT3, which is known for its oncogenic properties, and STAT1, which is recognized as a tumour suppressor[105].

Our findings unveil a tension sensitive mechanism through which caveolae exert a distant control over the regulation of various signalling pathways. The proposed mechanism is supported by a theoretical model that considers the thermodynamics of caveolae formation under mechanical stress. The model suggests that as membrane tension increases, there is a transition from caveolar Cav1 to Cav1 scaffolds, accompanied by an enhanced affinity of Cav1 towards its effectors. STORM imaging revealed a small pre-existing pool of Cav1 scaffolds at the plasma membrane. JAK1 associates with these scaffolds, indicating that this pool is functionally engaged. This population may arise from local caveolar disassembly triggered by local heterogeneities in membrane tension, as we previously reported in migrating cells[106]. Alternatively, they may represent synthesized Cav1–8S complexes that arrive at the plasma membrane as scaffold intermediates before their assembly into mature caveolae.

Mechanical forces can regulate diverse cellular functions by directly influencing protein interactions, such as reinforcing[107,108] or destabilizing interactions[43,109] and controlling enzymatic reactions[110]. Furthermore, mechanical deformations have been shown to uncover concealed or cryptic binding sites, as demonstrated for vinculin and talin[111], as well as cryptic phosphorylation[112] or proteolysis sites[113]. Thus, there is a consensus that external mechanical stresses are transmitted directly and rapidly to induce local protein deformation in mechanosensitive structures like integrin adhesions, the cytoskeleton or the nucleus[69,114–116]. Our findings reveal a different paradigm of mechanotransduction, challenging the notion that mechanical forces trigger immediate local effects or are rapidly transmitted through the cell via cytoskeletal elements or the membrane. Instead, we demonstrate that the conversion of caveolae into caveolin scaffolds generates mechanical messengers that diffuse at the plasma membrane. Cav1 scaffolds interact with signalling effectors at distant locations from the initial mechanosensing caveolae, with a time delay. Caveolae mechanosignalling may also serve as a mechanism for integrating and facilitating crosstalk with other mechanosensitive structures, such as integrin adhesions and the cytoskeleton. Notably, integrin adhesion and Cav1 have been functionally interconnected[38,117,118] and share common cytoskeleton partners[119] and signalling pathways[120–122]. In addition, caveolae have been associated with actin stress fibres and implicated in the regulation of their contractility[32,123,124]. In this context, it is interesting that protein deformation within integrin adhesion is not directly triggered by the transmission of external stretch but mediated by a delayed acto-myosin remodelling process[73].

The pathophysiological implications of caveolae mechanosignalling remain to be explored. Several of the signalling effectors regulated by this process, including PTEN, PTP1B and STAT3, are central to tumorigenesis. The role of Cav1 and caveolae in cancer has been debated due to their seemingly contradictory behaviour, with reports indicating both oncogenic and tumour suppressor properties[25,125–127]. The functional aspect of caveolae mechanics unveiled in this study may substantially influence tumour growth, as mechanical forces experienced by cancer cells during tumour progression could disrupt caveolae mechanosensing and alter the precise regulation of caveolae-mediated signalling.

Cav1 interacts with numerous proteins, including signalling molecules and membrane receptors. Yet, the lack of compelling evidence for the localization of these proteins inside caveolae, along with data suggesting exclusion of bulk plasma membrane proteins[34], raises the question of how caveolae regulate effectors located outside their structure. Our findings indicate that the reversible conversion of caveolae into Cav1 scaffolds allows distant control of such signalling molecules. Together, these results highlight caveolae as key mechanosignalling devices capable of remotely fine-tuning specific transduction processes at the plasma membrane. Our study not only advances the understanding of caveolae function in cell mechanics but also carries significant implications for human pathophysiology[22].

## Online content

Any methods, additional references, Nature Portfolio reporting summaries, source data, extended data, supplementary information, acknowledgements, peer review information; details of author contributions and competing interests; and statements of data and code availability are available at https://doi.org/10.1038/s41556-026-01966-0.

## References

1. Lamaze, C., Tardif, N., Dewulf, M., Vassilopoulos, S. & Blouin, C. M. The caveolae dress code: structure and signaling. *Curr. Opin. Cell Biol.* **47**, 117–125 (2017).
2. Parton, R. G. et al. Caveolae: the FAQs. *Traffic* **21**, 181–185 (2020).
3. Palade, G. E. The fine structure of blood capillaries. *J. Appl. Phys.* **24**, 1424 (1953).
4. Yamada, E. The fine structure of the gall bladder epithelium of the mouse. *J. Biophys. Biochem. Cytol.* **1**, 445–458 (1955).
5. Rothberg, K. G. et al. Caveolin, a protein component of caveolae membrane coats. *Cell* **68**, 673–682 (1992).
6. Way, M. & Parton, R. G. M-caveolin, a muscle-specific caveolin-related protein. *FEBS Lett.* **378**, 108–112 (1996).
7. Scherer, P. E. et al. Identification, sequence, and expression of caveolin-2 defines a caveolin gene family. *Proc. Natl Acad. Sci. USA* **93**, 131–135 (1996).
8. Aboulaich, N., Vainonen, J. P., Stralfors, P. & Vener, A. V. Vectorial proteomics reveal targeting, phosphorylation and specific fragmentation of polymerase I and transcript release factor (PTRF) at the surface of caveolae in human adipocytes. *Biochem. J.* **383**, 237–248 (2004).
9. Hill, M. M. et al. PTRF-Cavin, a conserved cytoplasmic protein required for caveola formation and function. *Cell* **132**, 113–124 (2008).
10. Liu, L. & Pilch, P. F. A critical role of cavin (polymerase I and transcript release factor) in caveolae formation and organization. *J. Biol. Chem.* **283**, 4314–4322 (2008).

11. Bastiani, M. et al. MURC/Cavin-4 and cavin family members form tissue-specific caveolar complexes. *J. Cell Biol.* **185**, 1259–1273 (2009).
12. Sverdlov, M., Shinin, V., Place, A. T., Castellon, M. & Minshall, R. D. Filamin A regulates caveolae internalization and trafficking in endothelial cells. *Mol. Biol. Cell* **20**, 4531–4540 (2009).
13. Senju, Y., Itoh, Y., Takano, K., Hamada, S. & Suetsugu, S. Essential role of PACSIN2/syndapin-II in caveolae membrane sculpting. *J. Cell Sci.* **124**, 2032–2040 (2011).
14. Hansen, C. G., Howard, G. & Nichols, B. J. Pacsin 2 is recruited to caveolae and functions in caveolar biogenesis. *J. Cell Sci.* **124**, 2777–2785 (2011).
15. Moren, B. et al. EHD2 regulates caveolar dynamics via ATP-driven targeting and oligomerization. *Mol. Biol. Cell* **23**, 1316–1329 (2012).
16. Koch, D., Westermann, M., Kessels, M. M. & Qualmann, B. Ultrastructural freeze-fracture immunolabeling identifies plasma membrane-localized syndapin II as a crucial factor in shaping caveolae. *Histochem. Cell Biol.* **138**, 215–230 (2012).
17. Porta, J. C. et al. Molecular architecture of the human caveolin-1 complex. *Sci. Adv.* **8**, eabn7232 (2022).
18. Patel, H. H., Murray, F. & Insel, P. A. Caveolae as organizers of pharmacologically relevant signal transduction molecules. *Annu. Rev. Pharmacol. Toxicol.* **48**, 359–391 (2008).
19. Lajoie, P. & Nabi, I. R. Lipid rafts, caveolae, and their endocytosis. *Int. Rev. Cell Mol. Biol.* **282**, 135–163 (2010).
20. Pilch, P. F., Meshulam, T., Ding, S. & Liu, L. Caveolae and lipid trafficking in adipocytes. *Clin. Lipidol.* **6**, 49–58 (2011).
21. Parton, R. G., McMahon, K. A. & Wu, Y. Caveolae: formation, dynamics, and function. *Curr. Opin. Cell Biol.* **65**, 8–16 (2020).
22. Lamaze, C., Blouin, C. M. & Sens, P. Caveolae mechanics in cellular functions and disease. *Nat. Rev. Mol. Cell Biol.* https://doi.org/10.1038/s41580-026-00964-2 (2026).
23. Minshall, R. D., Sessa, W. C., Stan, R. V., Anderson, R. G. & Malik, A. B. Caveolin regulation of endothelial function. *Am. J. Physiol. Lung Cell. Mol. Physiol.* **285**, L1179–L1183 (2003).
24. Williams, J. J. & Palmer, T. M. Cavin-1: caveolae-dependent signalling and cardiovascular disease. *Biochem. Soc. Trans.* **42**, 284–288 (2014).
25. Singh, V. & Lamaze, C. Membrane tension buffering by caveolae: a role in cancer?. *Cancer Metastasis Rev.* **2**, 505–517 (2020).
26. Liu, L. Lessons from cavin-1 deficiency. *Biochem. Soc. Trans.* **48**, 147–154 (2020).
27. Boscher, C. & Nabi, I. R. Caveolin-1: role in cell signaling. *Adv. Exp. Med. Biol.* **729**, 29–50 (2012).
28. Fridolfsson, H. N., Roth, D. M., Insel, P. A. & Patel, H. H. Regulation of intracellular signaling and function by caveolin. *FASEB J.* **28**, 3823–3831 (2014).
29. Couet, J., Sargiacomo, M. & Lisanti, M. P. Interaction of a receptor tyrosine kinase, EGF-R, with caveolins. Caveolin binding negatively regulates tyrosine and serine/threonine kinase activities. *J. Biol. Chem.* **272**, 30429–30438 (1997).
30. Nystrom, F. H., Chen, H., Cong, L. N., Li, Y. & Quon, M. J. Caveolin-1 interacts with the insulin receptor and can differentially modulate insulin signaling in transfected Cos-7 cells and rat adipose cells. *Mol. Endocrinol.* **13**, 2013–2024 (1999).
31. Bernatchez, P. N. et al. Dissecting the molecular control of endothelial NO synthase by caveolin-1 using cell-permeable peptides. *Proc. Natl Acad. Sci. USA* **102**, 761–766 (2005).
32. Grande-Garcia, A. et al. Caveolin-1 regulates cell polarization and directional migration through Src kinase and Rho GTPases. *J. Cell Biol.* **177**, 683–694 (2007).
33. Ariotti, N. et al. Caveolae regulate the nanoscale organization of the plasma membrane to remotely control Ras signaling. *J. Cell Biol.* **204**, 777–792 (2014).
34. Shvets, E., Bitsikas, V., Howard, G., Hansen, C. G. & Nichols, B. J. Dynamic caveolae exclude bulk membrane proteins and are required for sorting of excess glycosphingolipids. *Nat. Commun.* **6**, 6867 (2015).
35. Lajoie, P. et al. Plasma membrane domain organization regulates EGFR signaling in tumor cells. *J. Cell Biol.* **179**, 341–356 (2007).
36. Joshi, B. et al. Phosphorylated caveolin-1 regulates Rho/ROCK-dependent focal adhesion dynamics and tumor cell migration and invasion. *Cancer Res.* **68**, 8210–8220 (2008).
37. Moon, H. et al. PTRF/cavin-1 neutralizes non-caveolar caveolin-1 microdomains in prostate cancer. *Oncogene* **33**, 3561–3570 (2014).
38. Meng, F. et al. The phospho-caveolin-1 scaffolding domain dampens force fluctuations in focal adhesions and promotes cancer cell migration. *Mol. Biol. Cell* **28**, 2190–2201 (2017).
39. Lajoie, P., Goetz, J. G., Dennis, J. W. & Nabi, I. R. Lattices, rafts, and scaffolds: domain regulation of receptor signaling at the plasma membrane. *J. Cell Biol.* **185**, 381–385 (2009).
40. Khater, I. M., Meng, F., Wong, T. H., Nabi, I. R. & Hamarneh, G. Super resolution network analysis defines the molecular architecture of caveolae and caveolin-1 scaffolds. *Sci. Rep.* **8**, 9009 (2018).
41. Khater, I. M., Liu, Q., Chou, K. C., Hamarneh, G. & Nabi, I. R. Super-resolution modularity analysis shows polyhedral caveolin-1 oligomers combine to form scaffolds and caveolae. *Sci. Rep.* **9**, 9888 (2019).
42. Lolo, F. N. et al. Caveolin-1 dolines form a distinct and rapid caveolae-independent mechanoadaptation system. *Nat. Cell Biol.* https://doi.org/10.1038/s41556-022-01034-3 (2022).
43. Sinha, B. et al. Cells respond to mechanical stress by rapid disassembly of caveolae. *Cell* **144**, 402–413 (2011).
44. Cheng, J. P. et al. Caveolae protect endothelial cells from membrane rupture during increased cardiac output. *J. Cell Biol.* **211**, 53–61 (2015).
45. Lo, H. P. et al. The caveolin-cavin system plays a conserved and critical role in mechanoprotection of skeletal muscle. *J. Cell Biol.* **210**, 833–849 (2015).
46. Elliott, M. H. et al. Caveolin-1 modulates intraocular pressure: implications for caveolae mechanoprotection in glaucoma. *Sci. Rep.* **6**, 37127 (2016).
47. Lim, Y. W. et al. Caveolae protect notochord cells against catastrophic mechanical failure during development. *Curr. Biol.* **27**, 1968–1981.e1967 (2017).
48. Garcia, J. et al. Sheath cell invasion and trans-differentiation repair mechanical damage caused by loss of caveolae in the zebrafish notochord. *Curr. Biol.* **27**, 1982–1989.e1983 (2017).
49. Nassoy, P. & Lamaze, C. Stressing caveolae new role in cell mechanics. *Trends Cell Biol.* **22**, 381–389 (2012).
50. Parton, R. G. & Del Pozo, M. A. Caveolae as plasma membrane sensors, protectors and organizers. *Nat. Rev. Mol. Cell Biol.* **14**, 98–112 (2013).
51. Cheng, J. P. & Nichols, B. J. Caveolae: one function or many? *Trends Cell Biol.* **26**, 177–189 (2016).
52. Del Pozo, M. A., Lolo, F. N. & Echarri, A. Caveolae: mechanosensing and mechanotransduction devices linking membrane trafficking to mechanoadaptation. *Curr. Opin. Cell Biol.* **68**, 113–123 (2021).
53. Dewulf, M. et al. Dystrophy-associated caveolin-3 mutations reveal that caveolae couple IL6/STAT3 signaling with mechanosensing in human muscle cells. *Nat. Commun.* **10**, 1974 (2019).
54. Schreiber, G. & Piehler, J. The molecular basis for functional plasticity in type I interferon signaling. *Trends Immunol.* **36**, 139–149 (2015).

55. de Weerd, N. A., Kurowska, A. K., Mendoza, J. L. & Schreiber, G. Structure-function of type I and III interferons. *Curr. Opin. Immunol.* **86**, 102413 (2024).
56. Geletu, M. et al. Effect of caveolin-1 upon Stat3-ptyr705 levels in breast and lung carcinoma cells. *Biochem. Cell Biol.* https://doi.org/10.1139/bcb-2018-0367 (2019).
57. Geletu, M. et al. Reciprocal regulation of the cadherin-11/Stat3 axis by caveolin-1 in mouse fibroblasts and lung carcinoma cells. *Biochim. Biophys. Acta Mol. Cell Res.* **1865**, 794–802 (2018).
58. Gambin, Y. et al. Single-molecule analysis reveals self assembly and nanoscale segregation of two distinct cavin subcomplexes on caveolae. *eLife* **3**, e01434 (2013).
59. Torrino, S. et al. EHD2 is a mechanotransducer connecting caveolae dynamics with gene transcription. *J. Cell Biol.* **217**, 4092–4105 (2018).
60. Rossier, O. et al. Integrins β1 and β3 exhibit distinct dynamic nanoscale organizations inside focal adhesions. *Nat. Cell Biol.* **14**, 1057–1067 (2012).
61. Mehidi, A. et al. Forces generated by lamellipodial actin filament elongation regulate the WAVE complex during cell migration. *Nat. Cell Biol.* **23**, 1148–1162 (2021).
62. Orré, T. et al. Molecular motion and tridimensional nanoscale localization of kindlin control integrin activation in focal adhesions. *Nat. Commun.* **12**, 3104 (2021).
63. Pol, A., Morales-Paytuví, F., Bosch, M. & Parton, R. G. Non-caveolar caveolins: duties outside the caves. *J. Cell Sci.* https://doi.org/10.1242/jcs.241562 (2020).
64. Orre, T., Mehidi, A., Massou, S., Rossier, O. & Giannone, G. Using single-protein tracking to study cell migration. *Methods Mol. Biol.* **1749**, 291–311 (2018).
65. Ouyang, W., Aristov, A., Lelek, M., Hao, X. & Zimmer, C. Deep learning massively accelerates super-resolution localization microscopy. *Nat. Biotechnol.* **36**, 460–468 (2018).
66. Schermelleh, L. et al. Super-resolution microscopy demystified. *Nat. Cell Biol.* **21**, 72–84 (2019).
67. Khater, I. M., Nabi, I. R. & Hamarneh, G. A review of super-resolution single-molecule localization microscopy cluster analysis and quantification methods. *Patterns* **1**, 100038 (2020).
68. Möckl, L., Roy, A. R. & Moerner, W. E. Deep learning in single-molecule microscopy: fundamentals, caveats, and recent developments. *Biomed. Opt. Express* **11**, 1633–1661 (2020).
69. Nunes Vicente, F., Chen, T., Rossier, O. & Giannone, G. Novel imaging methods and force probes for molecular mechanobiology of cytoskeleton and adhesion. *Trends Cell Biol.* **33**, 204–220 (2023).
70. Monier, S. et al. VIP21-caveolin, a membrane protein constituent of the caveolar coat, oligomerizes in vivo and in vitro. *Mol. Biol. Cell* **6**, 911–927 (1995).
71. Hayer, A., Stoeber, M., Bissig, C. & Helenius, A. Biogenesis of caveolae: stepwise assembly of large caveolin and cavin complexes. *Traffic* **3**, 3 (2009).
72. Pelkmans, L. & Zerial, M. Kinase-regulated quantal assemblies and kiss-and-run recycling of caveolae. *Nature* **436**, 128–133 (2005).
73. Massou, S. et al. Cell stretching is amplified by active actin remodelling to deform and recruit proteins in mechanosensitive structures. *Nat. Cell Biol.* https://doi.org/10.1038/s41556-020-0548-2 (2020).
74. Shivanandan, A., Radenovic, A. & Sbalzarini, I. F. MosaicIA: an ImageJ/Fiji plugin for spatial pattern and interaction analysis. *BMC Bioinform.* **14**, 349 (2013).
75. Li, S., Couet, J. & Lisanti, M. P. Src tyrosine kinases, Gα subunits, and H-Ras share a common membrane-anchored scaffolding protein, caveolin. Caveolin binding negatively regulates the auto-activation of Src tyrosine kinases. *J. Biol. Chem.* **271**, 29182–29190 (1996).
76. García-Cardeña, G. et al. Dissecting the interaction between nitric oxide synthase (NOS) and caveolin. Functional significance of the nos caveolin binding domain in vivo. *J. Biol. Chem.* **272**, 25437–25440 (1997).
77. Bernatchez, P., Sharma, A., Bauer, P. M., Marin, E. & Sessa, W. C. A noninhibitory mutant of the caveolin-1 scaffolding domain enhances eNOS-derived NO synthesis and vasodilation in mice. *J. Clin. Invest.* **121**, 3747–3755 (2011).
78. Couet, J., Li, S., Okamoto, T., Ikezu, T. & Lisanti, M. P. Identification of peptide and protein ligands for the caveolin-scaffolding domain. Implications for the interaction of caveolin with caveolae-associated proteins. *J. Biol. Chem.* **272**, 6525–6533 (1997).
79. Oka, N. et al. Caveolin interaction with protein kinase C. Isoenzyme-dependent regulation of kinase activity by the caveolin scaffolding domain peptide. *J. Biol. Chem.* **272**, 33416–33421 (1997).
80. Collins, B. M., Davis, M. J., Hancock, J. F. & Parton, R. G. Structure-based reassessment of the caveolin signaling model: do caveolae regulate signaling through caveolin-protein interactions? *Dev. Cell* **23**, 11–20 (2012).
81. Kenworthy, A. K., Han, B., Ariotti, N. & Parton, R. G. The role of membrane lipids in the formation and function of caveolae. *Cold Spring Harb.Persp. Biol.* https://doi.org/10.1101/cshperspect.a041413 (2023).
82. Abramson, J. et al. Accurate structure prediction of biomolecular interactions with AlphaFold 3. *Nature* **630**, 493–500 (2024).
83. Doktorova, M. et al. Caveolin assemblies displace one bilayer leaflet to organize and bend membranes. *Proc. Natl Acad. Sci. USA* **122**, e2417024122 (2025).
84. Boellner, S. & Becker, K. F. Reverse phase protein arrays-quantitative assessment of multiple biomarkers in biopsies for clinical use. *Microarrays* **4**, 98–114 (2015).
85. Lee, H. et al. Identification of phosphocaveolin-1 as a novel protein tyrosine phosphatase 1B substrate. *Biochemistry* **45**, 234–240 (2006).
86. Saeedi Saravi, S. S. et al. Differential endothelial signaling responses elicited by chemogenetic $H_2O_2$ synthesis. *Redox Biol.* **36**, 101605 (2020).
87. Caselli, A., Mazzinghi, B., Camici, G., Manao, G. & Ramponi, G. Some protein tyrosine phosphatases target in part to lipid rafts and interact with caveolin-1. *Biochem. Biophys. Res. Commun.* **296**, 692–697 (2002).
88. Lolo, F.-N. et al. Caveolae couple mechanical stress to integrin recycling and activation. *eLife* **11**, e82348 (2022).
89. Monteiro, P. et al. A mechanosensitive caveolae-invadosome interplay drives matrix remodelling for cancer cell invasion. *Nat. Cell Biol.* **25**, 1787–1803 (2023).
90. Sens, P. & Turner, M. S. Theoretical model for the formation of caveolae and similar membrane invaginations. *Biophys. J.* **86**, 2049–2057 (2004).
91. Dulhunty, A. F. & Franzini-Armstrong, C. The relative contributions of the folds and caveolae to the surface membrane of frog skeletal muscle fibres at different sarcomere lengths. *J. Physiol.* **250**, 513–539 (1975).
92. Prescott, L. & Brightman, M. W. The sarcolemma of *Aplysia* smooth muscle in freeze-fracture preparations. *Tissue Cell* **8**, 248–258 (1976).
93. Gabella, G. & Blundell, D. Effect of stretch and contraction on caveolae of smooth muscle cells. *Cell Tissue Res.* **190**, 255–271 (1978).
94. Qifti, A., Balaji, S. & Scarlata, S. Deformation of caveolae impacts global transcription and translation processes through relocalization of cavin-1. *J. Biol. Chem.* **298**, 102005 (2022).
95. McMahon, K. A. et al. Cavin3 released from caveolae interacts with BRCA1 to regulate the cellular stress response. *eLife* **10**, e61407 (2021).

96. Byrne, D. P., Dart, C. & Rigden, D. J. Evaluating caveolin interactions: do proteins interact with the caveolin scaffolding domain through a widespread aromatic residue-rich motif?. *PLoS ONE* **7**, e44879 (2012).
97. Han, B. et al. Structure and assembly of CAV1 8S complexes revealed by single particle electron microscopy. *Sci. Adv.* https://doi.org/10.1126/sciadv.abc6185 (2020).
98. Lim, J. E., Bernatchez, P. & Nabi, I. R. Scaffolds and the scaffolding domain: an alternative paradigm for caveolin-1 signaling. *Biochem. Soc. Trans.* **52**, 947–959 (2024).
99. Wong, T. H. et al. Single molecule network analysis identifies structural changes to caveolae and scaffolds due to mutation of the caveolin-1 scaffolding domain. *Sci. Rep.* https://doi.org/10.1038/s41598-021-86770-6 (2021).
100. Okada, S. et al. Deletion of caveolin scaffolding domain alters cancer cell migration. *Cell Cycle* **18**, 1268–1280 (2019).
101. Jasmin, J. F., Mercier, I., Sotgia, F. & Lisanti, M. P. SOCS proteins and caveolin-1 as negative regulators of endocrine signaling. *Trends Endocrinol. Metab.* **17**, 150–158 (2006).
102. Kershaw, N. J., Murphy, J. M., Lucet, I. S., Nicola, N. A. & Babon, J. J. Regulation of Janus kinases by SOCS proteins. *Biochem. Soc. Trans.* **41**, 1042–1047 (2013).
103. Williams, J. J. L. et al. Interaction of suppressor of cytokine signalling 3 with cavin-1 links SOCS3 function and cavin-1 stability. *Nat. Commun.* **9**, 168 (2018).
104. Caveney, N. A. et al. Structural basis of Janus kinase trans-activation. *Cell Rep.* **42**, 112201 (2023).
105. Owen, K. L., Brockwell, N. K. & Parker, B. S. JAK-STAT signaling: a double-edged sword of immune regulation and cancer progression. *Cancers* https://doi.org/10.3390/cancers11122002 (2019).
106. Singh, V. et al. Spatiotemporal coupling of caveolae mechanosensing and RhoA-GEFs regulates cell polarity and directional migration. *Nat. Commun.* **17**, 398 (2025).
107. Friedland, J. C., Lee, M. H. & Boettiger, D. Mechanically activated integrin switch controls α5β1 function. *Science* **323**, 642–644 (2009).
108. Giannone, G., Jiang, G., Sutton, D. H., Critchley, D. R. & Sheetz, M. P. Talin1 is critical for force-dependent reinforcement of initial integrin-cytoskeleton bonds but not tyrosine kinase activation. *J. Cell Biol.* **163**, 409–419 (2003).
109. Jiang, G., Giannone, G., Critchley, D. R., Fukumoto, E. & Sheetz, M. P. Two-piconewton slip bond between fibronectin and the cytoskeleton depends on talin. *Nature* **424**, 334–337 (2003).
110. Wang, Y. et al. Visualizing the mechanical activation of Src. *Nature* **434**, 1040–1045 (2005).
111. del Rio, A. et al. Stretching single talin rod molecules activates vinculin binding. *Science* **323**, 638–641 (2009).
112. Sawada, Y. et al. Force sensing by mechanical extension of the Src family kinase substrate p130Cas. *Cell* **127**, 1015–1026 (2006).
113. Gordon, W. R. et al. Mechanical allostery: evidence for a force requirement in the proteolytic activation of notch. *Dev. Cell* **33**, 729–736 (2015).
114. Iskratsch, T., Wolfenson, H. & Sheetz, M. P. Appreciating force and shape-the rise of mechanotransduction in cell biology. *Nat. Rev. Mol. Cell Biol.* **15**, 825–833 (2014).
115. Ladoux, B. & Mège, R. M. Mechanobiology of collective cell behaviours. *Nat. Rev. Mol. Cell Biol.* **18**, 743–757 (2017).
116. Kirby, T. J. & Lammerding, J. Emerging views of the nucleus as a cellular mechanosensor. *Nat. Cell Biol.* **20**, 373–381 (2018).
117. del Pozo, M. A. et al. Phospho-caveolin-1 mediates integrin-regulated membrane domain internalization. *Nat. Cell Biol.* **7**, 901–908 (2005).
118. Osmani, N. et al. An Arf6- and caveolae-dependent pathway links hemidesmosome remodeling and mechanoresponse. *Mol. Biol. Cell* **29**, 435–451 (2018).
119. Muriel, O. et al. Phosphorylated filamin A regulates actin-linked caveolae dynamics. *J. Cell Sci.* **124**, 2763–2776 (2011).
120. Goetz, J. G. et al. Concerted regulation of focal adhesion dynamics by galectin-3 and tyrosine-phosphorylated caveolin-1. *J. Cell Biol.* **180**, 1261–1275 (2008).
121. Gottlieb-Abraham, E. et al. Src-mediated caveolin-1 phosphorylation affects the targeting of active Src to specific membrane sites. *Mol. Biol. Cell* **24**, 3881–3895 (2013).
122. Zimnicka, A. M. et al. Src-dependent phosphorylation of caveolin-1 Tyr-14 promotes swelling and release of caveolae. *Mol. Biol. Cell* **27**, 2090–2106 (2016).
123. Joshi, B. et al. Phosphocaveolin-1 is a mechanotransducer that induces caveola biogenesis via Egr1 transcriptional regulation. *J. Cell Biol.* **199**, 425–435 (2012).
124. Sotodosos-Alonso, L., Pulgarín-Alfaro, M. & Del Pozo, M. A. Caveolae mechanotransduction at the interface between cytoskeleton and extracellular matrix. *Cells* https://doi.org/10.3390/cells12060942 (2023).
125. Goetz, J. G., Lajoie, P., Wiseman, S. M. & Nabi, I. R. Caveolin-1 in tumor progression: the good, the bad and the ugly. *Cancer Metastasis Rev.* **27**, 715–735 (2008).
126. Lamaze, C. & Torrino, S. Caveolae and cancer: a new mechanical perspective. *Biomed. J.* **38**, 367–379 (2015).
127. Simón, L., Campos, A., Leyton, L. & Quest, A. F. G. Caveolin-1 function at the plasma membrane and in intracellular compartments in cancer. *Cancer Metastasis Rev.* **39**, 435–453 (2020).

---

[1]Membrane Mechanics and Dynamics of Intracellular Signalling Laboratory, Institut Curie–Centre de Recherche, PSL Research University, Paris, France. [2]Institut National de la Santé et de la Recherche Médicale (INSERM), U1339, Paris, France. [3]Centre National de la Recherche Scientifique (CNRS), UMR3666, Paris, France. [4]Interdisciplinary Institute for Neuroscience, University of Bordeaux, Bordeaux, France. [5]UMR 5297 CNRS, Bordeaux, France. [6]School of Computing Science, Simon Fraser University, Burnaby, British Columbia, Canada. [7]Department of Electrical and Computer Engineering, Faculty of Engineering and Technology, Birzeit University, Birzeit, Palestine. [8]Institut Curie, PSL University, INSERM U900, Mines Paris Tech, Paris, France. [9]Department of Cellular and Physiological Sciences, University of British Columbia, Vancouver, British Columbia, Canada. [10]Institute for Integrative Biology of the Cell (I2BC), Université Paris-Saclay, CEA, CNRS, Gif-sur-Yvette, France. [11]Institut Curie, PSL Research University, Sorbonne University, CNRS UMR168, Paris, France. [12]Present address: GlaxoSmithKline, Rueil-Malmaison, France. [13]Present address: Cell Biology and Biophysics Unit, European Molecular Biology Laboratory, Heidelberg, Germany. [14]Present address: Somaiya Centre for Integrated Science Education and Research, SciSER-Physics Department, Somaiya Vidyavihar University, Mumbai, India. [15]Present address: ALIRI Bioanalysis, Loos, France. [16]These authors contributed equally: Satish Kailasam Mani, Nicolas Tardif, Olivier Rossier. [17]These authors jointly supervised this work: Grégory Giannone, Cédric M. Blouin, Christophe Lamaze. ✉e-mail: cedric.blouin@curie.fr; christophe.lamaze@curie.fr

## Methods

This research complies with all relevant ethical regulations.

### Cell culture, transfection and cell treatments

All cell lines were cultured at 37 °C under 5% $CO_2$ in their respective culture medium. WT and Cav1$^{-/-}$ MLECs (a gift from R.V. Stan) were cultured in Endothelial Cell Growth Medium-2 (EGM-2) Bulletkit (Lonza, cat. no.CC-3162) composed of EBM-2 Basal Medium (cat. no. CC-3156) and supplemented with EGM-2 SingleQuots (cat. no. CC-4176) containing hydrocortisone, hFGF-B, VEGF, R3-IGF-1, ascorbic acid, hEGF, GA-1000 (gentamicin, amphotericin-B) and heparin along with 10% FBS (Gibco, Life Technologies). All MEF cell lines used in this study (MEF WT, MEF Cavin1$^{-/-}$ and MEF Cavin1$^{-/-}$ expressing low/medium/high levels of Cav1, a gift from M. del Pozo) were cultured in Dulbecco's modified Eagle medium (DMEM) GlutaMAX (Gibco, Life Technologies) supplemented with 10% FBS (Gibco, Life Technologies), 100 U ml$^{-1}$ penicillin–streptomycin, 1 mM sodium pyruvate and 15 mM HEPES.

Plasmids were transfected either by electroporation using Ingenio electroporation solution (Mirus Bio) or by lipofection using Lipofectamine LTX with Plus reagent (Invitrogen, Life Technologies), Lipofectamine 3000 (Invitrogen, Life Technologies) or HiPerFect transfection reagents (QIAGEN) following the manufacturer's instructions. Electroporation of cells was performed with a pulse of 220 V and 975 µF using a Gene Pulser II module (Bio-Rad). siRNA transfections were performed using the HiPerFect kit and cells were incubated for 3 days before further experimentation. Depletion efficiency was assessed by immunoblotting.

Unless otherwise stated, stimulation with IFNα or IFNβ (recombinant mouse IFNα; BioLegend cat. no. 752806, mouse IFNβ; Tebubio, cat. no. 12400-1) was performed at a concentration of 1,000 U ml$^{-1}$ and 500 U ml$^{-1}$, respectively. For cell stretching experiments, cells were grown on a rectangular polydimethylsiloxane (PDMS) sheet (thickness ~100 µm, dimensions ~12 × 7 mm) coated with fibronectin and stretched uni-axially using a custom-built device equipped with a motorized linear actuator (PI, Karlsruhe) and a temperature controller. Cells were pre-stretched by 25% for 2 min and stretch was maintained during IFNα stimulation. For hypo-osmotic shock (HYPO), cells were subjected to culture medium diluted in water and processed for subsequent experiments. Unless otherwise stated, cells were subjected to 30 mOsm hypo-osmotic shock (10% culture medium and 90% water) for a duration of 5 min. Recovery of cells was performed by first subjecting the cells to a 5-min hypo-osmotic shock and immediately replenishing with normal culture medium (300 mOsm). Unless otherwise stated, recovery was performed for a duration of 5 min after hypo-osmotic shock.

### Plasmids and antibodies

Cav1–GFP and Cavin1–mEGFP were a gift from A. Helenius (Addgene plasmid #14433; https://n2t.net/addgene:14433; RRID: Addgene_14433 and Addgene plasmid #27709; http://n2t.net/addgene:27709; RRID: Addgene_27709, respectively). Cav1–mRFP and Cav1-F92A/V94A–mRFP plasmids are described elsewhere[38]. Cav1–W98-mRFP was generated using site-directed mutagenesis from Cav1–mRFP. mEos3.2-Caveolin-C-10 was a gift from M. Davidson (Addgene plasmid #57447; http://n2t.net/addgene:57447; RRID: Addgene 57447). mEos2-CAAX was generated by amplifying the coding DNA sequence of the corresponding protein by PCR and inserted into pcDNAm-FRT-PC-mEos2 blue at Fse1/Asc1 sites. For the generation of ALFA-tagged JAK1 WT, JAK1Δ(1056–1154) and JAK1Δ(1071–1154) constructs, JAK1 was first amplified with primers containing the ALFA-tag sequence. The amplicon was then cloned into a pmCherry-C vector backbone, devoid of the mCherry sequence. Subsequently, point mutations were introduced at the desired residues by site-directed mutagenesis to generate the respective mutants. The fidelity of all constructs was verified by sequencing.

The following primary antibodies and their dilutions were used: mouse anti-α-tubulin (Sigma-Aldrich, clone B512, cat. no. T5168, 1:1,000 for WB); mouse anti-STAT3 (Cell Signalling, clone 124H6, cat. no. 9139, 1:1,000 for WB); rabbit anti-pSTAT3 (Tyr705) (Cell Signalling Technologies, clone D3A7, cat. no. 9145, 1:1,000 for WB, 1:100 for IF); rabbit anti-STAT1 (Cell Signalling Technologies, cat. no. 9172, 1:1,000 for WB); mouse anti-pSTAT1 (Tyr701) (Cell Signalling Technologies, clone 58D6, cat. no. 9167, 1:1,000 for WB, 1:100 for IF); mouse anti-Cav1 (BD Transduction, cat. no. 610407, 1:1,000 for WB); rabbit anti-Cav1 (Cell Signalling Technologies cat. no. 3238S, 1:1,000 for WB, 2–5 µg per condition for IP, 1:50 for dSTORM, 1:150 for IF); mouse anti-PTRF (BD Transduction, cat. no. 611258, 1:1,000 for WB); rabbit anti-PTRF (cat. no. ab48824, Abcam, discontinued, 1:1,000 for WB, 1:50 for dSTORM, 1:150 for IF); rabbit anti-JAK1 (Cell Signalling Technologies, cat. no. 3332S, 1:2,000 for WB); mouse anti-JAK1 (Santa Cruz Biotechnology, cat. no. sc-1677, 1:50 for STORM). Rabbit anti-eNOS (Cell Signalling Technologies cat. no. 32027S, 1:2,000 for WB); rabbit anti-PTEN (Cell Signalling Technologies cat. no. 9188S, 1:2,000 for WB); rabbit anti-AKT (Cell Signalling Technologies, cat. no. 9272S, 1:2,000 for WB); rabbit anti-pAKT (Ser473) (Cell Signalling Technologies, cat. no. 4060S, 1:2,000 for WB); rabbit anti-PTP1B (Abcam, cat. no. ab244207, 1:2,000 for WB); rabbit anti-β1-integrin (Proteintech, cat. no. 12594-1-AP); rabbit anti-mCherry (Institut Curie Recombinant antibody platform, A-P-R no. 13); p-eNOS (Ser1177) (Thermo Fisher, cat. no. PA5-104858, 1:2,000 for WB).

For secondary antibodies, donkey anti-mouse-HRP (Jackson ImmunoResearch, cat. no. 715-035-151) and donkey anti-rabbit-HRP (Jackson ImmunoResearch, cat. no. 711-035-152) were used at a dilution of 1:5,000 for WB; donkey anti-mouse-AF647 (Jackson ImmunoResearch, cat. no. 715-606-150) and donkey anti-rabbit-CF680 (Biotium, cat. no. 20820) were used at a dilution of 1:200 and 1:400, respectively, for STORM imaging. Donkey anti-mouse DyLight 800 (cat. no. SA5-10172); and donkey anti-goat DyLight 800 (cat. no. SA5-10044).

### CSD-mimicking peptides

CSD-mimicking peptides were synthetized from Biomatik (control peptide sequence, HHHHHH-RQIKIWFQNRRMKWKKWGIDKASFTTFTVTKYWFRY; CavTratin sequence, HHHHHH-QIKIWFQNRRMKWKKDGIWKASFTTFTVTKY; and CavNoxin sequence, HHHHHH-RQIKIWFQNRRMKWKKDGIWKASFAAATVTKWYFYR). Cells were treated for 6 h with 1 µM CSD-mimicking peptide resuspended in EGM-2 culture medium.

### In vitro kinase activity measurement

In vitro kinase assay was performed using purified JAK1 (ProQinase 1480-0000-1 JAK1 aa583-1154) and RBER-IRStide (ProQinase 0863-0000-1). The kinase reaction was performed in kinase reaction buffer (100 µM ATP, 80 µg ml$^{-1}$ RBER-IRStide and dimethylsulfoxide according to peptide concentration) at 30 °C for 1 h. Measurement of ADP production was performed using a Promega ADP-Glo Kinase Assay. Luminescence measurement was performed using BMG Labtech FLUOstar Omega plate reader.

### Immunoblotting

Cells were lysed in sample buffer (62.5 mM Tris-HCl, pH 6.0, 2% (vol/vol) SDS, 10% (vol/vol) glycerol, 40 mM dithiothreitol and 0.03% (wt/vol) phenol red). The lysates were analysed by SDS–PAGE on 4–20% mini-PROTEAN TGX or TGX stain-free precast protein gels (Bio-Rad) and immunoblotted with the indicated primary and secondary antibodies that were either horseradish peroxidase-conjugated or fluorescently labelled. The chemiluminescence signal was revealed using Pierce ECL western blotting, SuperSignal west dura extended duration or SuperSignal west femto (Thermo Scientific Life Technologies) substrate. Acquisition and quantification were performed using a ChemiDoc MP imaging system (Bio-Rad). For STAT1, the phosphorylated and total protein levels were assayed on the same blot with the primary antibodies mouse anti-pSTAT1 and rabbit anti-STAT1, and visualized using fluorescence and luminescence, respectively. The ratio of phosphorylated-to-total protein was determined for each time point.

### Immunofluorescence

For immunofluorescence (IF) analysis, cells were either cultured on coverslips or PDMS as per the experimental procedure, treated as described earlier and then fixed with ice-cold methanol for 15 min at −20 °C. After washing with 0.2% (wt/vol) BSA in PBS, the cells were subsequently incubated with the indicated primary antibody and fluorescence-conjugated secondary antibody for 1 h at room temperature. The coverslips were mounted in Fluoromount-G mounting medium (eBioscience) with 2 µg ml$^{-1}$ 4,6-diamidino-2-phenylindole (Sigma-Aldrich) to counterstain nuclei. Images were acquired on a Leica DM 6000B inverted wide-field microscope equipped with a HCX PL Apo ×63, 1.40 numerical aperture (NA) oil immersion objective and an electron-multiplying charge-coupled device camera (Photometrics CoolSMAP HQ). Nuclear translocation of pSTAT1:pSTAT3 was quantified using a homemade plugin in the ImageJ software (National Institutes of Health) by calculating the nuclear-to-cytoplasmic ratio of the pSTAT1:pSTAT3 signal (nuclei masks were realized with 4,6-diamidino-2-phenylindole staining). Detailed light microscopy acquisition and reporting parameters are provided in Supplementary Table 3.

### Co-immunoprecipitation

Cells were lysed in 1% NP-40 in ice-cold Tris–NaCl–EDTA (10 mM Tris-HCl, pH 7.5, 150 mM NaCl and 0.5 mM EDTA) with protease inhibitor cocktail (Roche) for 30 min. For conventional co-immunoprecipitation, cleared lysates (16,000*g* for 10 min at 4 °C) were incubated overnight with 1 µg ml$^{-1}$ of the indicated antibody at 4 °C, with rotation, followed by incubation for 1 h with 25 µl protein A/G magnetic beads (Thermo Scientific) in the case of endogenous proteins. For tagged proteins, 25 µl of GFP-Trap or RFP-Trap beads (Chromotek) were used. After three washes in Tris–NaCl–EDTA buffer, the immunoprecipitated beads were eluted following the manufacturer's instructions. Magnetic crosslink co-immunoprecipitation (Pierce Crosslink Magnetic IP/Co-IP kit, cat. no. 88805) was performed as per the manufacturer's instruction. In brief, the desired antibody was covalently crosslinked to protein A/G magnetic beads using the DSS (disuccinimidyl suberate) crosslinker and subsequently incubated overnight with pre-cleared lysates at 4 °C. Incubated beads were then eluted and the immunoprecipitates were analysed by immunoblotting.

### Spinning-disc confocal microscopy

Time-lapse images were acquired using an inverted Nikon Eclipse Ti-E microscope equipped with a Yokogawa CSU-X1 spinning disc confocal unit, integrated into MetaMorph software (Gataca Systems). The system featured an sCMOS camera with 95% quantum efficiency and a pixel size of 11 µm. Appropriate emission filters were used for each fluorophore: 4,6-diamidino-2-phenylindole (440 nm), GFP (ET525/50), mCherry (605/64) and Cy5 (ET708/75). Imaging was performed using a ×40 CFI Plan Fluor NA 1.3 oil objective. Detailed light microscopy acquisition and reporting parameters are provided in Supplementary Table 3.

### dSTORM sample preparation

MLEC WT cells grown on high resolution no. 1.5 glass coverslips (THOR labs) were washed three times with PHEM solution (60 mM PIPES, 25 mM HEPES, 5 mM EGTA and 2 mM Mg acetate adjusted to pH 6.9 with 1 M KOH) and fixed for 20 min in 4% PFA. They were then washed three times in PBS (137 mM NaCl, 2.7 mM KCl, 8 mM $Na_2HPO_4$ and 2 mM $KH_2PO_4$). Up to this fixation step, all chemical reagents were pre- warmed at 37 °C. The cells were then quenched for auto-fluorescence from PFA in 50 mM $NH_4Cl$ for 20 min at room temperature. The cells were washed in PBS three times before being blocked and permeabilized in blocking buffer (1× PBS, 1% BSA and 0.1% saponin) for 1 h at room temperature. Fixed cells were incubated for 1 h at 37 °C with the respective primary antibodies diluted in blocking buffer and washed three times with PBS. This was followed by 1-h incubation at 37 °C with corresponding secondary antibodies diluted in blocking buffer and washed three times with PBS. After immunolabelling, a post-fixation step was performed using PBS with 3.6% formaldehyde for 15 min. The cells were washed in PBS three times and then reduced for 10 min with 50 mM $NH_4Cl$ (Sigma-Aldrich, 254134), followed by three additional washes in PBS.

### Dual-colour dSTORM imaging

Fluorophores Alexa-Fluor 647 (AF647) and CF680 photo switch under reducing and oxygen-free buffer conditions, making them suitable for dSTORM single-molecule imaging, which enables the localization of the emitters with sub-diffraction localization precision[128]. Thanks to their close spectral proximity, AF647 was excited and acquired simultaneously with CF680 in the same dSTORM buffer (Abbelight SMART-Kit) using a 640-nm laser (Oxxius), and their respective signals discriminated after single-molecule localization using a spectral-demixing strategy[129]. To implement spectral-demixing dSTORM of JAK1–A647 and Cav1–CF680, we used a dual-view Abbelight SAFe360, equipped with two Hamamatsu Fusion sCMOS cameras and mounted on an Olympus Ix83 inverted microscope with a ×100 1.5 NA TIRF objective. The SAFe360 uses astigmatic PSF engineering to extract the axial position and achieves quasi-isotropic 3D localization precision, and a long-pass dichroic mirror to split fluorescence from single emitters on the two cameras. Samples were illuminated in HILO at 80% of max laser power and imaged at 50-ms exposure time for 100,000 frames. Single-molecule localization, drift correction, spectral demixing and data visualization were performed using Abbelight NEO software. Detailed light microscopy acquisition and reporting parameters are provided in Supplementary Table 3.

### 3D SMLM network analysis

A total of 30 cells (15 cells each for ISO and HYPO conditions) stained for Cav1–CF680 and JAK1–AF647 were imaged using the Abbelight SAFe360 microscope utilizing the spectral-demixing technique. Cav1 localizations were processed, and the resulting clusters were classified using the 3D SMLM network analysis pipeline described previously[40]. The datasets were analysed using the 3D SMLM network analysis based on the following parameters: merging threshold = 19 nm (to correct multiple blinking of single fluorophores); proximity threshold = 80 nm (for network construction); α = 2 (for noise filtering); bandwidth = 120 nm (for segmenting the localization into blobs/clusters using mean shift algorithm). Following this, 28 features/descriptors (such as shape, topology, network, size and hollowness) were extracted for every segmented blob/cluster. The clusters/blobs feature of every condition were then grouped into four groups using the *x*-means algorithm. The biological names for the groups of caveolae and S2, S1A and S1B scaffolds, were obtained by comparing the group centres with the Cav1 groups that were obtained previously[40] and were assigned based on the best match (highest similarity).

### Spatial pattern and interaction analysis

The interaction analysis was performed using the MosaicIA plugin[74] for Fiji by loading the 3D coordinates of JAK1 and the centre of mass of the corresponding Cav1 clusters identified using the 3D SMLM network analysis pipeline (namely caveolae, S2, S1B and S1A scaffolds) from a total of 30 cells (15 cells each for ISO and HYPO condition) and selecting two random ROIs from each cell. The workflow for interaction analysis described previously[74] was followed. In brief, we computed the cross–nearest-neighbour distance distribution between JAK1 and Cav1 localizations and fitted a pairwise Gibbs interaction model that infers the interaction potential's strength ($\varepsilon$) and range ($\sigma$) that best explain the observed pattern after context correction (controls for density and mask geometry). In this framework, a positive $\varepsilon$ indicates spatial attraction (co-organization) and a negative $\varepsilon$ indicates repulsion relative to the null. The following parameters were used for computing distance distributions: grid spacing = 0.2 (this value was chosen by sequentially reducing the grid spacing until the q($d$) does not significantly change); Kernel wt(q) = 0.001; Kernel wt(p) was used as suggested by the software. To determine the best parametric potential for the dataset, a non-parametric potential was first used to estimate the shape of interaction. The various available parametric potentials were then tested to determine the one that best fits the estimated shape of interaction. The Linear L1 potential resulted in the best fit and hence was used for subsequent datasets. The strength of interaction was plotted for each Cav1 cluster type under ISO and HYPO conditions.

### Colocalization/nearest localization using distance to centroid

The open-source software Point Cloud Analyst (https://github.com/flevet/PoCA) was used to determine the distance to centroids between objects of interest (between JAK1 and the various classes of Cav1 clusters) within a defined ROI. In brief, the 3D coordinates of JAK1 and Cav1 clusters (namely caveolae, S2, S1B and S1A scaffolds) identified using the 3D SMLM network analysis pipeline were loaded individually and the corresponding Voronoi diagram or tessellation was generated using an in-built algorithm. For creating objects from the Voronoi tessellations, a cutoff threshold of 75 and 100 with a minimum number of localizations of 2 and 11 was used for JAK1 and Cav1, respectively. The centroids of the resulting objects were extracted following which the centroids of JAK1 and the various Cav1 cluster objects were superimposed in pairs (for example, JAK1–Caveolae, JAK1–S2, JAK1–S1B and JAK1–S1A). The distance to centroids for each pair was calculated within several defined ROIs using the Cav1 cluster centroids as the reference, which is the distance that computation was carried out between JAK1 objects (centroids) and the outline of the reference (Cav1 objects).

### Micromechanical stretching device compatible with super-resolution microscopy

The stretching device compatible with super-resolution microscopy (used for DNA-PAINT and single-particle tracking in the current manuscript) has been described previously[73,130]. In brief, a plasma-cleaned PDMS sheet (10 µm; Sylgard 184, DE9330, Samaro) was deposited on a plasma-cleaned glass coverslip, lubricated by a thin layer of low-viscous glycerol (glycerol for fluorescence microscopy; CAS 56-81-5; Merck; 1040950250), and reinforced by a thicker elastomer frame (40 µm, PF film X0; 1.5 mil; Gel-Pak). The 40-µm elastomer frame was pre-cut to the size of the glass coverslip with a squared (3 × 3 mm) observation chamber using a Graphtec cutting plotter (Graphtec Craft ROBO pro; CE5000-40-CRP). Uniaxial stretch was applied using a milled (Charlyrobot, Mecanumic) poly(methyl methacrylate) device consisting of a fixed holding arm and a mobile arm, positioned on opposite sides of the observation chamber on the elastomer frame. The mobile arm was connected to a mechanical motor (MTS-65, 52 mm; linear stage with stepper motor; 0.1-µm resolution; PI). The PDMS substrate was coated with human fibronectin (10 µg ml$^{-1}$) for 90 min at 37 °C. Then, after electroporation with Cav1–GFP, MLEC Cav1$^{-/-}$ cells were plated on the stretching device and spread overnight at 37 °C.

### DNA-PAINT acquisition and analysis

The stretching device was mounted on an inverted motorized microscope (Nikon Ti) equipped with a CFI Apochromat TIRF ×100 oil, NA 1.49 objective and a perfect focus system (PFS-2). First, live stretching onto the microscope was performed at 37 °C. To calibrate the strain on each stretching device, we adsorbed 0.1-µm fluorescent beads (TetraSpeck Microspheres; 0.1 µm; Thermo Fisher Scientific; T7279) on the stretching chamber and used a small stretch (2–3%) before the stretching protocol. Strain was calculated using distances of same beads before and after stretch: strain = $(L_{\mathrm{stretch}} - L_0)/L_0$, where $L_0$ is the beads distance before stretch and $L_{\mathrm{stretch}}$ is the distance for same beads after stretch. Then, a uniaxial cyclic stretch (stretch: 30% strain, 0.5 Hz, 30 min) was applied, followed by rapid cell fixation in 4% paraformaldehyde in PBS buffer for 15 min. Then, cells were quenched with glycine (150 mM) for 20 min, and blocked for 90 min with 3% BSA and 0.2% Triton X-100 in PBS, then incubated with GFP nanobody conjugated with a DNA strand P1 for 4 h (5′ Nanobody GFP–TTA TAC ATC TA 3′), followed by a second fixation with 4% paraformaldehyde and 0.2% glutaraldehyde in PBS for 20 min.

DNA-PAINT acquisitions[131] after live stretching and fixation were performed at 25 °C in stretching devices on the same microscope. Before DNA-PAINT, we acquired low-resolution images of Cav1–GFP. Then, super-resolution imaging was performed thanks to the perfect focus system, allowing long acquisition in TIRF illumination mode, required for SMLM, including DNA-PAINT. To register super-resolution intensity images, we adsorbed 90-nm gold nanoparticles (Cytodiagnostics) on the stretching chamber that were imaged during the entirety of the DNA-PAINT acquisitions. Cy3B-labelled DNA imager strands (5′ CTA GAT GTA T–Cy3b 3′) were added to the stretching chamber at variable concentrations (0.2 to 1 nM), and visualized with a 561-nm laser (Coherent Obis FP series lasers) with 20 mW power at the sample plane. Fluorescence was collected by the combination of a dichroic filter and emission filters (dichroic, Di01-R561; emission, FF01-617/73; Semrock) and a sensitive scientific complementary metal-oxide semiconductor (ORCA-Flash4.0, Hammamatsu). Cav1–GFP was imaged using a conventional GFP filter cube (excitation, FF01-472/30; dichroic, FF-495Di02; emission, FF02-520/28; Semrock). The acquisitions were steered by MetaMorph software (Molecular Devices) in streaming mode at 100 ms for 90,000 frames. DNA-PAINT image reconstruction and drift correction were carried out using the Picasso software[131]. The spatial resolution of DNA-PAINT acquisitions obtained on stretching device was ~15.7 ± 1.5 nm (full width at half maximum). SR-Tesseler[132] was used to segment DNA-PAINT super-resolution images, to obtain the size distribution of Cav1–GFP clusters without stretching, or after cyclic stretching. Single-molecule localizations were used to compute Voronoi diagram. Clusters were segmented using average density factor of 20. To filter background noise of DNA-PAINT acquisitions, often corresponding to unspecific binding of some DNA imager strands to the cover-glass, we set a threshold for the number of localizations (50), enabling to select only genuine signals associated with binding to DNA docking strands. To analyse the smallest Cav1–GFP structures detected using DNA-PAINT, we manually selected isolated clusters that exhibited DNA-PAINT signals throughout the entire acquisition period. The size of these clusters was measured using SR-Tesseler[131].

### sptPALM sample preparation

For both MLEC and MEF cells, transient transfections of plasmids were performed 1 day before experiments using the Nucleofactor transfection kit for MEF-1 and Nucleofactor IIb device (Amaxa, Lonza). For MLECs, cells were detached with accutase solution (Sigma-Aldrich, cat. no. SLBT9789). The accutase was inactivated using EGM-2 medium, and the cells were washed and suspended in EGM-2 medium. Cells were then seeded overnight in EGM-2 medium on nitric-acid-cleaned glass coverslips. The next day, EGM-2 medium was rinsed once with PBS and left for experiment in serum-free Ringer medium (150 mM NaCl, 5 mM KCl, 2 mM $CaCl_2$, 2 mM $MgCl_2$ and 10 mM HEPES, pH 7.4) supplemented with 11 mM glucose. For MEFs, cells were detached with 0.05% trypsin, 0.02% EDTA solution (Gibco, cat. no. 25300054). The trypsin was inactivated using soybean trypsin inhibitor (1 mg ml$^{-1}$ in DMEM, Sigma), and the cells were washed and suspended in serum-free Ringer medium (150 mM NaCl, 5 mM KCl, 2 mM $CaCl_2$, 2 mM $MgCl_2$ and 10 mM HEPES, pH 7.4) supplemented with 11 mM glucose. Cells were then seeded on a human fibronectin-coated surface (10 µg ml$^{-1}$ fibronectin, Roche). The MEF PTRF/Cavin1$^{-/-}$ cell line was a gift from M. del Pozo (Spanish National Centre for Cardiovascular Research, Spain) and is described elsewhere[42]. Absence of *Mycoplasma* contamination was assessed using the MycoAlert detection kit (Lonza, cat. no. LT07-318). For sptPALM, 120,000 MLEC or 50,000 MEF cells were seeded on no. 1.5H glass coverslips (Marienfeld). When mentioned, hypo-osmotic shock was induced by replacing the observation medium (Ringer + glucose) with a Ringer + glucose solution diluted ten times with MQ-grade deionized water, at least 5 min before acquisition.

### sptPALM optical setup and image acquisition

All acquisitions were steered by MetaMorph software (Molecular Devices) with an inverted motorized microscope (Nikon Ti) equipped with a temperature control system (The Cube, The Box, Life Imaging Services), a Nikon CFI Apo TIRF ×100 oil, NA 1.49 objective and a perfect focus system, allowing long acquisition in TIRF illumination mode. The coverslip was mounted in a Ludin chamber (Life Imaging Services) before acquisition. For photoactivation localization microscopy, cells expressing mEos3.2-tagged constructs were photoactivated using a 405-nm laser (Omicron) and the resulting photoconverted single-molecule fluorescence was excited with a 561-nm laser (Cobolt Jive). Both lasers illuminated the sample simultaneously. Their respective power was adjusted to keep the number of the stochastically activated molecules constant and well separated during the acquisition. Fluorescence was collected by the combination of a dichroic and emission filters (D101-R561 and F39-617, respectively; Chroma) and a sensitive electron-multiplying charge-coupled device (Evolve, Photometric). The acquisition was performed in streaming mode at 50 Hz. Cav1–GFP and Cavin1–mEGFP was imaged using a conventional GFP filter cube (ET470/40, T495LPXR, ET525/50, Chroma). Using this filter cube does not allow spectral separation of the unconverted pool of mEos3.2 from the GFP fluorescent signal. For this reason, in the case of the MEF Cavin1$^{-/-}$ cell line, we were able to detect Cav1-based structures (scaffolds) with the unconverted pool of mEos3.2–Cav-1 (whose emission spectra is similar to the one of GFP).

### Single-molecule segmentation and tracking

A typical sptPALM experiment leads to a set of at least 4,000 images per cell, analysed to extract molecule localization and dynamics. Single-molecule fluorescent spots were localized and tracked over time using a combination of wavelet segmentation and simulated annealing algorithms[133–135]. Under the experimental conditions described above, the resolution of the system was quantified to 59 nm (full width at half maximum). This spatial resolution depends on the image signal to noise ratio and the segmentation algorithm[136] and was determined using fixed mEos3.2 samples. We analysed 130 two-dimensional distributions of single molecule positions belonging to long trajectories (>50 frames) by bi-dimensional Gaussian fitting, the resolution being determined as 2.3 $s_{xy}$, where $s_{xy}$ is the pointing accuracy.

For the trajectory analysis, cell contours were identified manually from Cav1–GFP or unconverted pool of mEos3.2-Cav1 images. We analysed trajectories lasting at least 260 ms (≥13 points) with a custom MATLAB routine analysing the mean squared displacement (MSD), which describes the diffusion properties of a molecule, computed as equation (3):

$$\mathrm{MSD}\,(t = n \times \Delta t) = \frac{\sum_{i=1}^{N-n} (x_{i+n} + x_i)^2 + (y_{i+n} - y_i)^2}{N - n} \tag{3}$$

where $x_i$ and $y_i$ are the coordinates of the label position at time $I \times \Delta t$. We defined the measured diffusion coefficient $D$ as the slope of the affine regression line fitted to the $n = 1$–4 values of the MSD ($n \times \Delta t$). The MSD was computed then fitted on a duration equal to 80% (minimum of 10 points, 200 ms) of the whole stretch by equation (4):

$$\mathrm{MSD}\,(t) = \frac{4 r_{\mathrm{conf}}^2}{3} \left(1 - \mathrm{e}^{-t/\tau}\right) \tag{4}$$

where $r_{\mathrm{conf}}$ is the measured confinement radius and $\tau$ the time constant $\tau = (r_{\mathrm{conf}}{}^2/3D_{\mathrm{conf}})$. To reduce the inaccuracy of the MSD fit due to down sampling for larger time intervals, we used a weighted fit. Trajectories were sorted in three groups: immobile, confined and diffusive. Immobile trajectories were defined as trajectories with $D < 0.011\ \mu\mathrm{m}^2\ \mathrm{s}^{-1}$, corresponding to molecules that explored an area inferior to the one defined by the image spatial resolution ~(0.05 µm)$^2$ during the time used to fit the initial slope of the MSD[60] (four points, 80 ms): $D_{\mathrm{threshold}} = (0.059\ \mu\mathrm{m})^2/(4 \times 4 \times 0.02\ \mathrm{s})$~$0.011\ \mu\mathrm{m}^2\ \mathrm{s}^{-1}$. To separate confined and diffusive trajectories, we used the time constant calculated $\tau$ for each trajectory. Confined and diffusive events were defined as trajectories with a time constant inferior and superior to half the time interval used to compute the MSD (100 ms), respectively.

### Molecular modelling and simulation

Structural predictions were performed using AF3 (ref. 82) through the AlphaFold Server (https://alphafoldserver.com). Protein sequences were retrieved from UniProt (The UniProt Consortium, 2025) (Q03135, CAV1_HUMAN; P23458, JAK1_HUMAN). Structural models were analysed using UCSF ChimeraX (v.1.11)[137].

The AF3-predicted structure of the JAK1 kinase domain in complex with Cav1(80–110) was further investigated by MD simulations in explicit solvent. The initial structure was built and refined using successive steps of energy minimization and restrained MD with CHARMM (v.49b1)[138], using the CHARMM36m force field[139]. The system was solvated in a TIP3P water orthorhombic box using the solvate module of VMD[140] with a minimum distance of 12 Å between the protein/peptide and the box boundaries in all directions. The system was subsequently neutralized and supplemented with Na$^+$ and Cl$^-$ ions to reach an ionic strength of 150 mM. Energy minimization was performed for 10,000 steps under positional restraints to maintain the structure close to the initial conformation. Several minimization cycles were applied, during which the force constant on atomic positions was gradually reduced from 10 kcal mol$^{-1}$ Å$^{-2}$ to 0. This step was followed by a 2-ns MD equilibration step in the NVT ensemble. Production simulations were then carried out in the NPT ensemble for 0.7 µs. To account for stochastic effects, three MD trajectories were run with different initial velocities. Temperature was maintained at 310 K and pressure at 1 atm using Langevin dynamics. During production, a time step of 2 fs was used, and multiple time stepping was applied using the rRESPA algorithm, with long-range electrostatic interactions computed every 4 fs using the Particle Mesh Ewald method with a real-space grid spacing of 1 Å. Periodic boundary conditions were applied. A cutoff distance of 12 Å was used for short-range electrostatic and van der Waals interactions. MD simulations were performed using NAMD v.3.0.1 (CUDA version)[141]. Calculations were carried out on A100 GPU resources provided by GENCI at IDRIS@CNRS (Jean Zay supercomputer). Trajectory analyses were conducted using CHARMM v.49b1. MD trajectories were analysed using ChimeraX v.1.11 and VMD. Figures were generated with ChimeraX v.1.11 and Gnuplot v.6.0 (http://www.gnuplot.info, 2023).

### Sample preparation for RPPA high-throughput screening

A total of 25 µg ml$^{-1}$ fibronectin diluted in 100 mM NaOH, pH 8.6 was incubated on a PDMS layer at 37 °C. Then, 70,000 WT MLEC or MLEC Cav1$^{-/-}$ cells were seeded and incubated for 4 h at 37 °C in complete MLEC medium. Cells were stretched by 25% for 2 min, then while the stretch was maintained, the cell medium was replaced with stimulation medium (EBM-2 no serum with IFNα 1,000 U ml$^{-1}$) for 20 min at 37 °C. Cells were washed with PBS and lysed with hot Laemmli 1× sample buffer (50 mM Tris, pH 6.8, 2% SDS, 5% glycerol, 2 mM dithiothreitol, 2.5 mM EDTA, 2.5 mM/EGTA, 2× phosphatase inhibitors (Halt Phosphatase inhibitor cocktail 100×, Perbio, Ref. 78420) and protease inhibitors (protease inhibitor cocktail, complete MINI EDTA-free, Roche, ref. 1,1836170 tablet/5 ml, 4 mM sodium orthovanadate and 20 mM sodium fluoride)). Samples were snap frozen in liquid nitrogen and later subjected to RPPA analysis.

### Hydrogen peroxide stimulation and eNOS Ser1177 phosphorylation

MLEC WT and Cav1 knockout (Cav1$^{-/-}$) cells were cultured under standard conditions to the indicated confluency. For oxidative stimulation, cells were treated with $H_2O_2$ (100 µM final concentration) for 15 min at 37 °C. At the end of treatment, cells were placed on ice, washed once with ice-cold PBS and lysed in ice-cold lysis buffer supplemented with protease and phosphatase inhibitors. Equal amounts of protein were resolved by SDS–PAGE and transferred to nitrocellulose membranes. Membranes were blocked and immunoblotted with an antibody to phospho-eNOS (Ser1177). Where indicated, membranes were subsequently probed for total eNOS and/or a loading control. Bands were visualized using chemiluminescence and quantified by densitometry.

### Statistics and reproducibility

No statistical methods were used to predetermine sample sizes. All collected data were included in subsequent analyses without exclusion. For all experiments, sample allocation to treatment groups used simple randomization protocols. Researchers were not blinded to group allocation during experimental procedures or the outcome evaluation. Data distribution was assumed to be normal but this was not formally tested.

### Reporting summary

Further information on research design is available in the Nature Portfolio Reporting Summary linked to this article.

## Data availability

Source data have been provided for the graphs and uncropped blot and gel scans in the Figures and Extended Data. All other data supporting the findings of this study and newly generated plasmids (Cav1–W98–mRFP, ALFA-tagged JAK1-WT, JAK1-Δ(1072–1154) or JAK1-Δ(1057–1154)) are available from the corresponding author on reasonable request. AF3 structures for Jak1–CAV1(80–110) are available on ModelArchive at https://modelarchive.org/ with the accession code ma-ys8kz[142]. Source data are provided with this paper.

## Code availability

Codes and algorithms used to analyse all data have already been described elsewhere and are publicly available.

## References

128. Heilemann, M. et al. Subdiffraction-resolution fluorescence imaging with conventional fluorescent probes. *Angewandte Chemie* **47**, 6172–6176 (2008).
129. Lampe, A., Tadeus, G. & Schmoranzer, J. Spectral demixing avoids registration errors and reduces noise in multicolor localization-based super-resolution microscopy. *Methods. Appl. Fluoresc.* **3**, 034006 (2015).
130. Nunes Vicente, F. et al. Molecular organization and mechanics of single vimentin filaments revealed by super-resolution imaging. *Sci. Adv.* **8**, eabm2696 (2022).
131. Schnitzbauer, J., Strauss, M. T., Schlichthaerle, T., Schueder, F. & Jungmann, R. Super-resolution microscopy with DNA-PAINT. *Nat. Protoc.* **12**, 1198–1228 (2017).
132. Levet, F. et al. SR-Tesseler: a method to segment and quantify localization-based super-resolution microscopy data. *Nat. Methods* **12**, 1065–1071 (2015).
133. Izeddin, I. et al. Wavelet analysis for single molecule localization microscopy. *Opt. Express* **20**, 2081–2095 (2012).
134. Racine, V. et al. Visualization and quantification of vesicle trafficking on a three-dimensional cytoskeleton network in living cells. *J. Microsc.* **225**, 214–228 (2007).
135. Racine, V. et al. in Multiple-target tracking of 3D fluorescent objects based on simulated annealing. *IEEE International Symposium on Biomedical Imaging* 6–9 April. 1020–1023 (IEEE, 2006).
136. Cheezum, M. K., Walker, W. F. & Guilford, W. H. Quantitative comparison of algorithms for tracking single fluorescent particles. *Biophys. J.* **81**, 2378–2388 (2001).
137. Meng, E. C. et al. UCSF ChimeraX: tools for structure building and analysis. *Protein Sci.* **32**, e4792 (2023).
138. Brooks, B. R. et al. CHARMM: the biomolecular simulation program. *J. Comput. Chem.* **30**, 1545–1614 (2009).
139. Huang, J. et al. CHARMM36m: an improved force field for folded and intrinsically disordered proteins. *Nat. Methods* **14**, 71–73 (2017).
140. Humphrey, W., Dalke, A. & Schulten, K. VMD: visual molecular dynamics. *J. Mol. Graph* **14**, 27–38 (1996). 33-38.
141. Phillips, J. C. et al. Scalable molecular dynamics with NAMD. *J. Comput. Chem.* **26**, 1781–1802 (2005).
142. Tauriello, G. et al. ModelArchive: a deposition database for computational macromolecular structural models. *J. Mol. Biol.* **437**, 168996 (2025).

## Acknowledgements

We are grateful to A. Kenworthy, B. Han and M. Doktorova for sharing their preliminary data on coarse-grain MD[83] and for their stimulating discussions. We are also indebted to I. S. Moreira, University of Coimbra for sharing preliminary data on docking experiments and for insightful discussions. The core facilities and the CurieCoreTech recombinant antibodies platform of Institut Curie, the scientific and technical assistance from staff of the Cell and Tissue Imaging (PICT-IBiSA) and the Nikon Imaging Centre at Institut Curie, member of the French National Research Infractucture France-BioImaging (ANR-10-INBS-04) are acknowledged. We thank C. Schietroma from Abbelight for technical assistance with SMLM (STORM) experiments. We are grateful to P. Nassoy and F. Wetzel for the design and development of the stretching device compatible with super-resolution microscopy, and to P. Nassoy for his insightful and extensive discussions on the mechanobiological responses of proteins in cells. The help of the following people for providing cell lines is acknowledged: R. V. Stan (Dartmouth CollegeA) and M. Del Pozo and F.-N. Lolo (Spanish National Centre for Cardiovascular Research). This work was supported by institutional grants from the Curie Institute, Institut National de la Santé et de la Recherche Médicale, CNRS and by specific grants from Agence Nationale de la Recherche (ANR-19-CE15-0020-02) and INCa 2018-1-PL BIO-08-ICR-1 (decision no. 2018-154) to C.L. Funding from France Canada Research Fund: NVKA GR013361 - FCRF to C.L. and I.R.N. is acknowledged. Exchanges between the C.L. and I.R.N. laboratories are supported by an International Research Project 'IRP Cav1'. G.G. was supported by the INCA (AAP PL BIO no. 2020-109), the ANR (ANR-21-CE11-0004-01) and the French Government in the framework of the University of Bordeaux's IdEx 'Investments for the Future' programme/GPR BRAIN_2030, GPR LIGHT. O.R. was supported by the ANR (ANR-20-CE42-0003-02) and the Nouvelle-Aquitaine Regional Council (AAPR2021-2020-12041310). S.K.M. was supported by a PhD fellowship from Ligue Nationale contre le Cancer, N.T. by a PhD fellowship from Ministère de l'Enseignement Supérieur et de la Recherche, M.D. by a PhD fellowship from Association Française contre les Myopathies: CAV-MUT (17151) and V.B. by a postdoctoral fellowship from Fondation de France (WB-2024-54138). The Lamaze and Sens teams are members of Labex Cell(n) scale ANR-10-LBX-0038, part of the IDEX PSL ANR-10-IDEX-0001-02.

MD simulations were carried out on A100 GPU resources provided by GENCI at IDRIS@CNRS (Jean Zay supercomputer; allocation A0190715663). The funders had no role in study design, data collection and analysis, decision to publish or preparation of the manuscript.

## Author contributions

S.K.M., N.T., P.C. and C.M.B. designed and performed the experiments, analysed and interpreted the data, and wrote the manuscript. O.R. designed and performed the sptPALM experiments, analysed and interpreted the corresponding data. X.Z., F.N.V. and G.G. designed and performed the DNA-PAINT experiments. A.R., C.G., P.G.T., R.R. and M.D. performed experiments. I.B. performed RPPA analysis. I.K., I.R.N., V.B. and G.H. analysed and interpreted the 3D STORM data using 3D SMLM network analysis. P.S. designed the physical model for theoretical validation of the study. G.G., O.R., I.K., I.R.N., P.C., P.S. and C.M.B. proofread and edited the manuscript. C.L. supervised the study, designed the experiments, interpreted the data and wrote the manuscript. All authors discussed the results and commented on the manuscript.

## Competing interests

The authors declare no competing interests.

## Additional information

**Extended data** is available for this paper at https://doi.org/10.1038/s41556-026-01966-0.

**Supplementary information** The online version contains supplementary material available at https://doi.org/10.1038/s41556-026-01966-0.

**Correspondence and requests for materials** should be addressed to Cédric M. Blouin or Christophe Lamaze.

**Peer review information** *Nature Cell Biology* thanks Ai Shinobu, and the other, anonymous, reviewer(s) for their contribution to the peer review of this work. Peer reviewer reports are available.

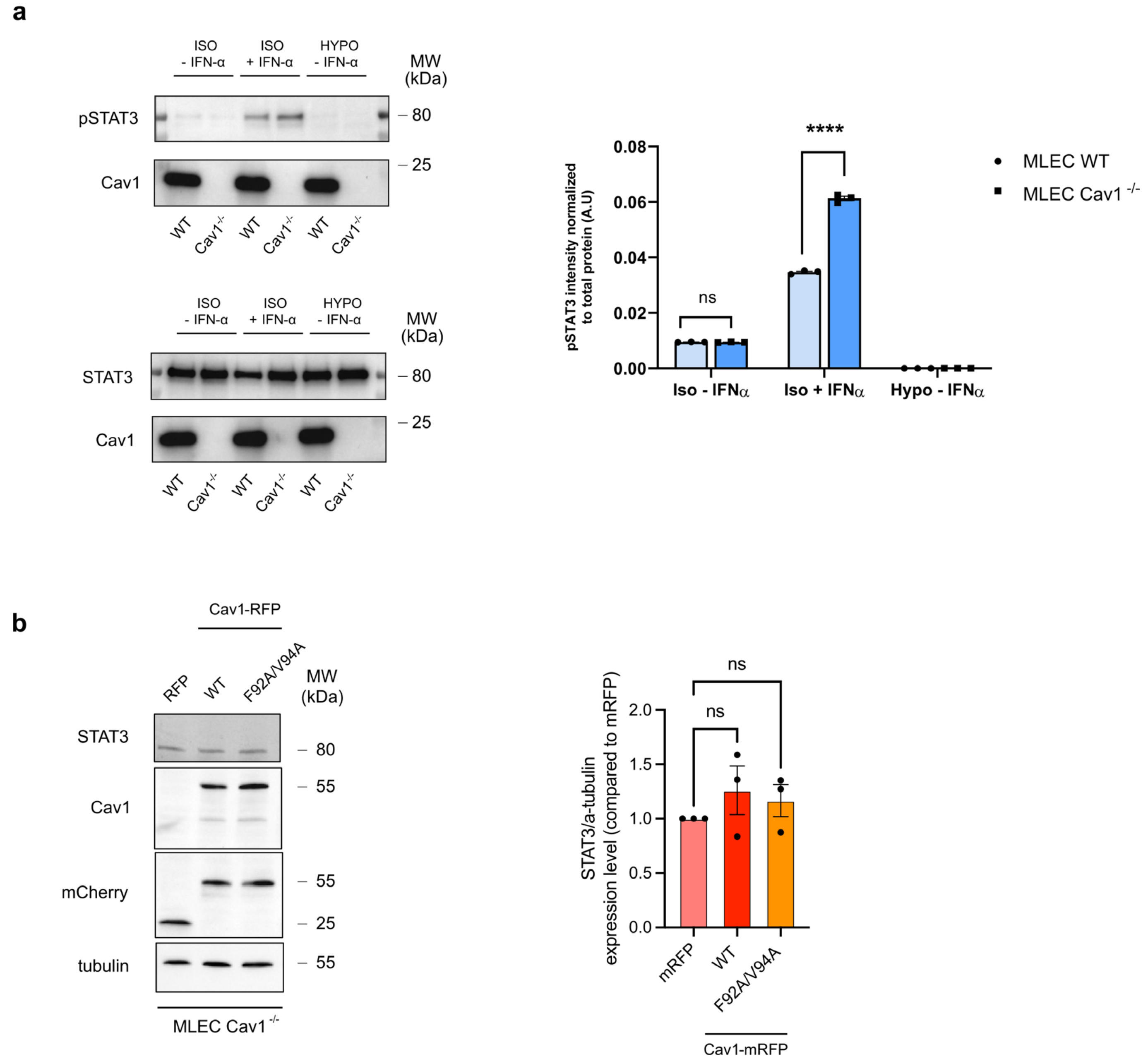

**Extended Data Fig. 1 | Cav1-dependent regulation of basal and IFN-α-induced STAT3 signalling.** (**a**) Representative immunoblots showing pSTAT3(Tyr705) and STAT3 levels in MLEC WT and MLEC Cav1$^{-/-}$ cells under iso-osmotic (ISO) and hypo-osmotic (HYPO) conditions, in the presence or absence of IFN-α, as indicated. Quantification is based on the pSTAT3(Tyr705)/total protein signal ratio, where total protein was determined from the corresponding stain-free blot. Immunoblots are representative of 3 independent biological experiments with similar results. Quantified data are presented as mean ± s.d. (bars, mean; error bars, s.d.), with individual data points representing 3 independent biological replicates ($n = 3$). Statistical significance was assessed using a two-sided ANOVA with multiple-comparisons correction. Exact P values are indicated in the figure and provided in the Source Data. (**b**) Representative immunoblots of lysates from MLEC WT cells expressing RFP, Cav1-WT–RFP, or Cav1-F92A/V94A–RFP, probed for pSTAT3, STAT3, and α-tubulin under basal conditions. Quantification is shown as the STAT3/α-tubulin signal ratio normalized to the RFP control condition. Immunoblots are representative of 3 independent biological experiments with similar results. Quantified data are presented as mean ± s.d. (bars, mean; error bars, s.d.), with individual data points representing 3 independent biological replicates ($n = 3$). Statistical significance was assessed using a two-sided ANOVA with multiple-comparisons correction. Exact P values are provided in the Source Data. ****$P < 0.0001$; ns, not significant. Source numerical data and unprocessed blots are available in source data.

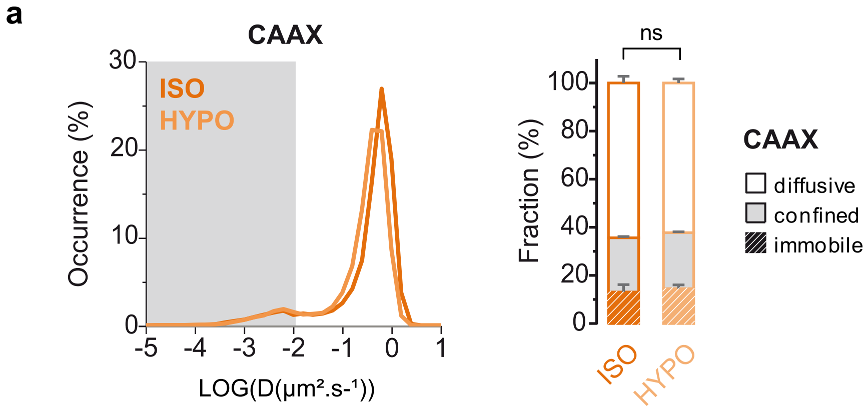

**Extended Data Fig. 2 | Diffusion of a membrane-anchored CAAX probe is not altered by hypo-osmotic shock.** (**a**) Distribution of the diffusion coefficient (D) computed from mEos3.2-CAAX trajectories in MLEC WT cells under iso-osmotic (ISO; dark orange) and hypo-osmotic (HYPO; light orange) conditions, shown on a logarithmic scale. The grey area corresponds to D < 0.011 µm$^2$ s$^{-1}$ and defines the immobile fraction. Right, fractions of diffusive, confined, and immobile trajectories in ISO and HYPO conditions. Data were obtained from single cells pooled from 2 independent biological experiments (ISO, *n* = 9 cells; HYPO, *n* = 11 cells). Where summary values are shown, data are presented as mean ± SEM (bars, mean; error bars, SEM; for distribution plots, lines, mean; shaded bands/error bars, SEM, if shown). Statistical significance was assessed using a two-sided ANOVA with multiple-comparisons correction. Exact P values are provided in the Source Data. ns, not significant. Source numerical data are available in source data.

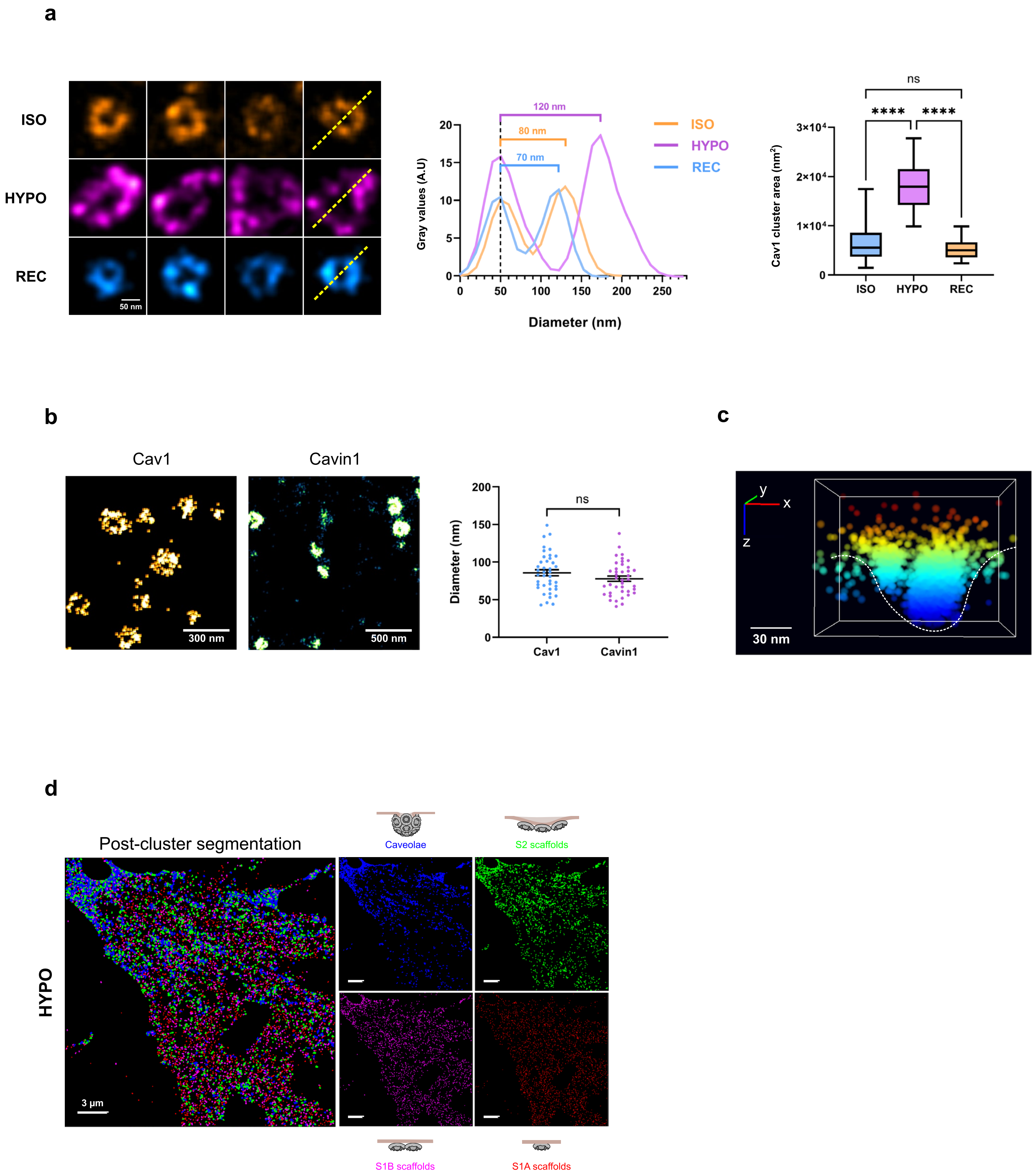

**Extended Data Fig. 3 | See next page for caption.**

**Extended Data Fig. 3 | Nanoscale characterization of Cav1-positive structures by dSTORM and 3D SMLM network analysis.** (**a**) Left: Representative 2D dSTORM acquisitions of MLEC WT cells stained for Cav1–AF647 under iso-osmotic (ISO), hypo-osmotic (HYPO) and recovery (REC) conditions. Scale bar: 50 nm. Middle: representative line-intensity profiles of Cav1-positive structures illustrating the change in apparent diameter across conditions. Right: box-and-whisker plots showing the distribution of Cav1 cluster area ($nm^2$) in ISO, HYPO and REC conditions. Each point corresponds to one segmented Cav1 cluster (*n* = 73 clusters per condition, technical observations pooled from 3 independent biological experiments). Box plots are defined as follows: centre line, median; box bounds: 25th and 75th percentiles; whiskers: minimum and maximum values. Statistical significance was assessed using ordinary one-way ANOVA followed by Tukey's multiple-comparisons test. Exact P values are provided in the Source Data. ****P < 0.0001; ns: not significant. (**b**) Representative 3D STORM spectral-demixing images of Cav1–CF680 and Cavin1–CF680 in MLEC WT cells at steady state, together with quantification of Cav1 and Cavin1 cluster diameters. Images are representative of 3 independent biological experiments with similar results. For the quantification, each point represents one particle (*n* = 40 particles per condition, technical observations). Data are presented as mean ± s.d. (horizontal bar, mean; error bars, s.d.). Statistical significance was assessed using a two-sided unpaired t-test. Exact P values are provided in the Source Data. ns, not significant. Scale bars: 300 nm (Cav1) and 500 nm (Cavin1). (**c**) Side view of a 3D point cloud localization corresponding to a bona fide budded caveola in MLEC WT cells at steady state. The dotted line indicates the putative position of the plasma membrane. Image is representative of 3 independent biological experiments with similar results. Scale bar: 30 nm. (**d**) Representative 3D STORM localizations of Cav1 in MLEC WT cells under HYPO, processed and segmented using the 3D SMLM network/graph-based analysis pipeline to classify Cav1 localizations into caveolae and the non-caveolar scaffold populations S2, S1B and S1A. Images are representative of 3 independent biological experiments with similar results. Source numerical data are available in source data.

https://doi.org/10.1038/s41556-026-01966-0

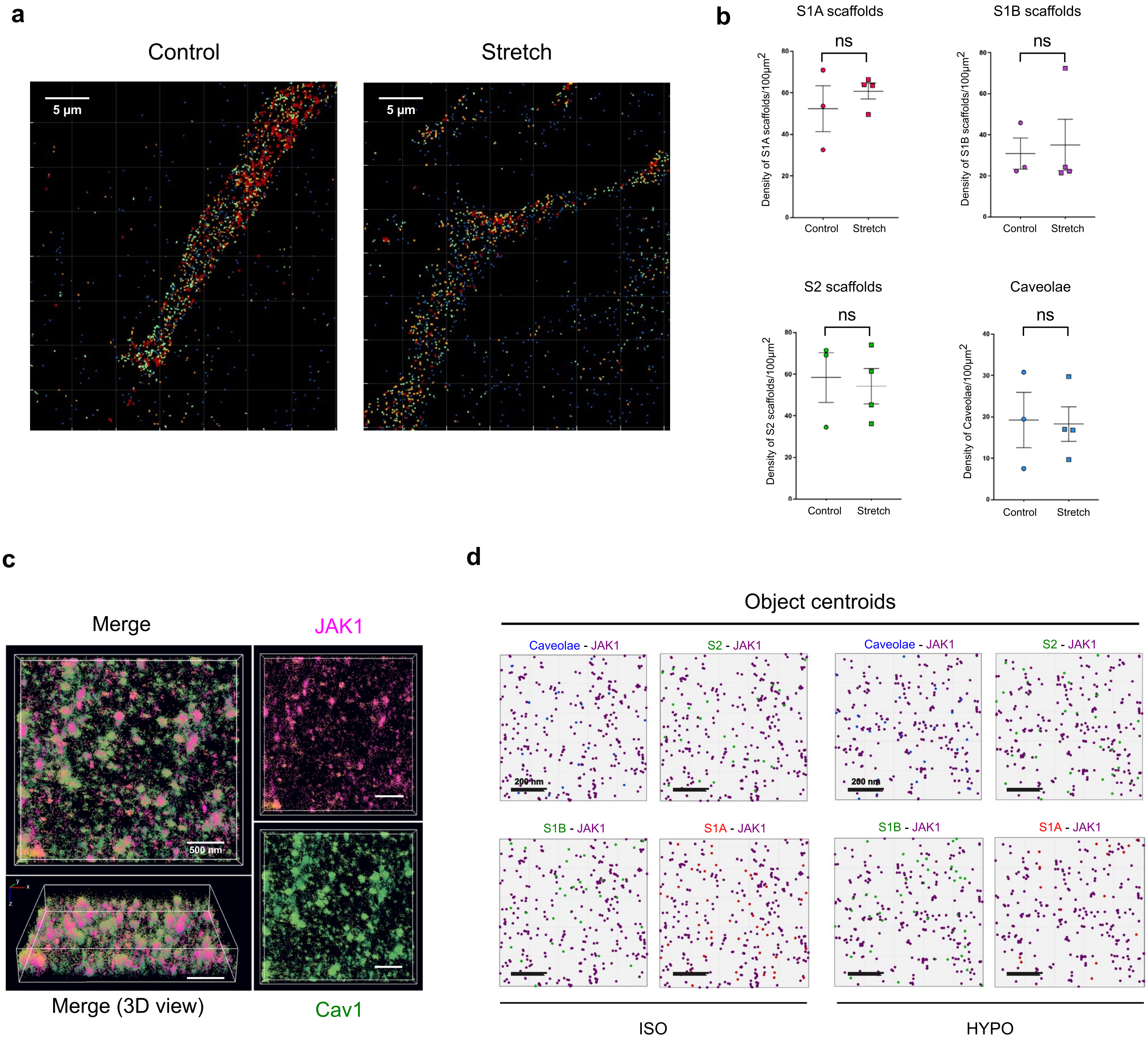

**Extended Data Fig. 4 | DNA-PAINT-based classification of Cav1 assemblies under stretch and qualitative 3D visualization of Cav1–JAK1 proximity.** (**a**) Representative DNA-PAINT localizations of Cav1 in MLEC WT cells under control (no stretch) and 30 min uniaxial stretch conditions. DNA-PAINT coordinate datasets were processed and segmented using the same 3D SMLM network/graph-based analysis pipeline used in the main figures to classify Cav1 localizations into caveolae and the non-caveolar scaffold populations S2, S1B and S1A. Images are representative of data acquired across 3 independent biological experiments with similar results. Scale bars: 5 µm. (**b**) Quantification of the density of Cav1 objects per 100 µm$^2$ for each class (caveolae, S2, S1B and S1A) under control and stretch conditions. Data are presented as mean ± SD (horizontal bar, mean; error bars, SD), with individual data points representing single cells (control, $n = 3$ cells; stretch, $n = 4$ cells) acquired across 3 independent biological experiments. Statistical significance was assessed using a two-sided Mann–Whitney U test. ns: not significant. (**c**) Representative 3D spectral-demixing STORM visualization of Cav1–CF680 and JAK1–AF647 point cloud localizations in MLEC WT cells at steady state, shown as merged views and individual channels to provide a qualitative visualization of Cav1–JAK1 spatial overlap/proximity. Images are representative of 3 independent biological experiments with similar results. Scale bar: 500 nm. (**d**) Representative views of the extracted object centroids corresponding to the Cav1–JAK1 object pairs shown in Fig. 4e, overlaid with JAK1 localizations within a defined ROI under iso-osmotic (ISO) and hypo-osmotic shock (HYPO) conditions. Images are representative of data acquired from 15 cells per condition across 3 independent biological experiments with similar results. Scale bar: 200 nm. Source numerical data are available in source data.

https://doi.org/10.1038/s41556-026-01966-0

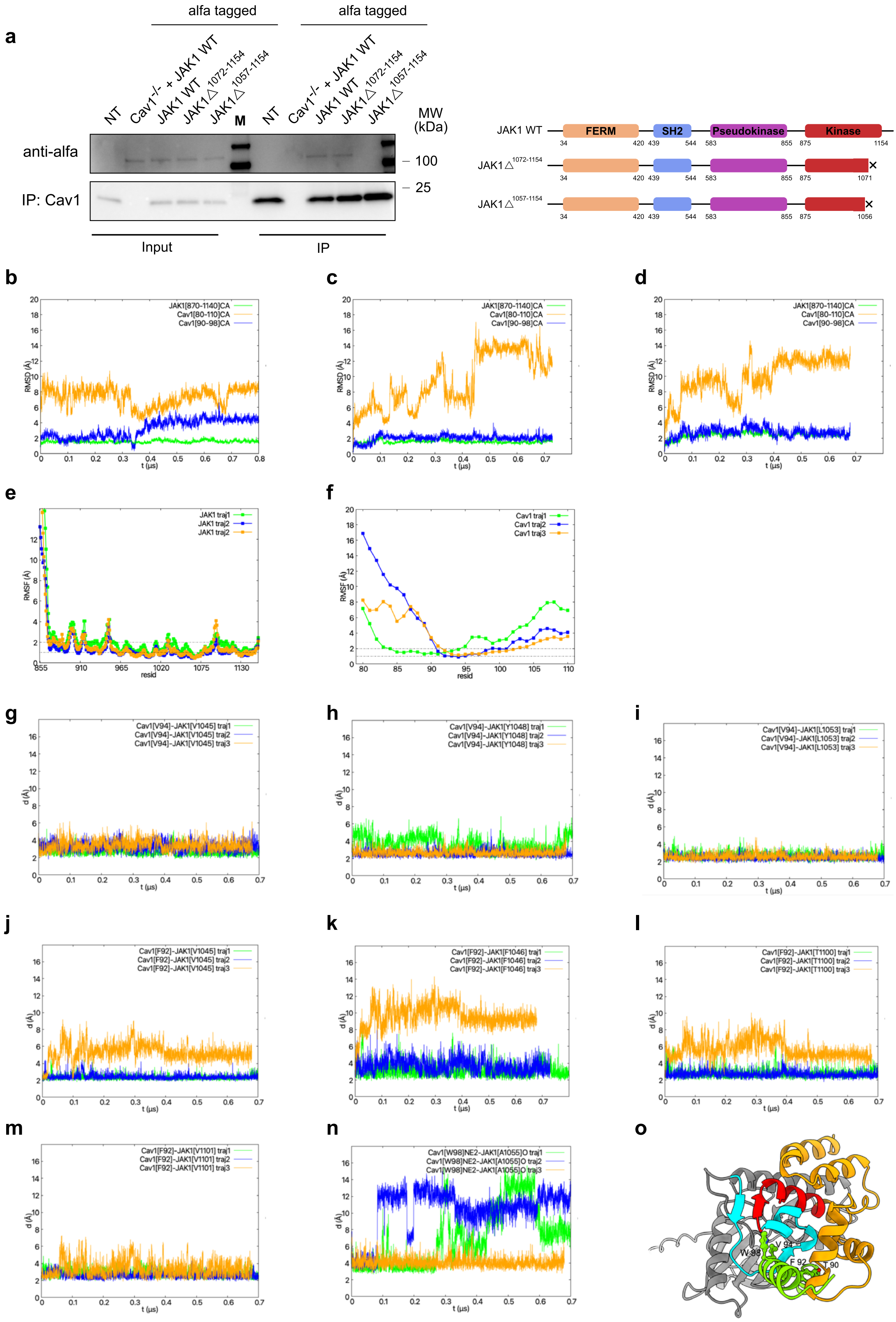

**Extended Data Fig. 5 | See next page for caption.**

**Extended Data Fig. 5 | Mapping and molecular modelling of the Cav1–JAK1 interaction interface.** (**a**) Left, representative immunoprecipitation of endogenous Cav1 from MLEC WT cells expressing ALFA-tagged JAK1-WT, JAK1-Δ1072–1154, or JAK1-Δ1057–1154 constructs. Immunoblots are representative of 3 independent biological experiments (*n* = 3) with similar results. Right, schematic representation of the corresponding ALFA-tagged JAK1 constructs. (**b**–**d**) Root-mean-square deviation (RMSD) of Cα atoms along molecular dynamics (MD) trajectories 1 (**b**), 2 (**c**), and 3 (**d**) for the JAK1[855–1154] kinase domain (green), the Cav1[80–110] peptide (orange), and the Cav1[90–98] segment (blue). (**e**) Root-mean-square fluctuation (RMSF) of Cα atoms for JAK1[855–1154]. (**f**) RMSF of Cα atoms for the Cav1[80–110] peptide. In (**e,f**), dashed lines indicate RMSF values of 1.0 Å and 2.0 Å. (**g**–**i**) Minimum distances along MD trajectories 1 (green), 2 (blue), and 3 (orange) between the side chain of Cav1 V94 and JAK1 V1045 (**g**), JAK1 Y1048 (**h**), and JAK1 L1053 (**i**).(**j**–**m**) Minimum distances along MD trajectories 1 (green), 2 (blue), and 3 (orange) between the side chain of Cav1 F92 and JAK1 V1045 (**j**), JAK1 F1046 (**k**), JAK1 T1100 (**l**), and JAK1 V1101 (**m**). (**n**) Distance between the Nε2 atom of Cav1W98 and the backbone carbonyl oxygen of JAK1 Q1055 along the MD trajectories. (**o**) Cartoon representation of the AF3-refined JAK1[855–1154]–Cav1[80–110] complex. JAK1 is shown in grey, except for segment 1033–1055 (cyan), segment 1056–1070 (red), and segment 1071–1154 (orange). Cav1[80–110] is shown in green, and the side chains of T90, F92, V94, and W98 are shown in ball-and-stick representation. Source numerical data and unprocessed blots are available in source data.

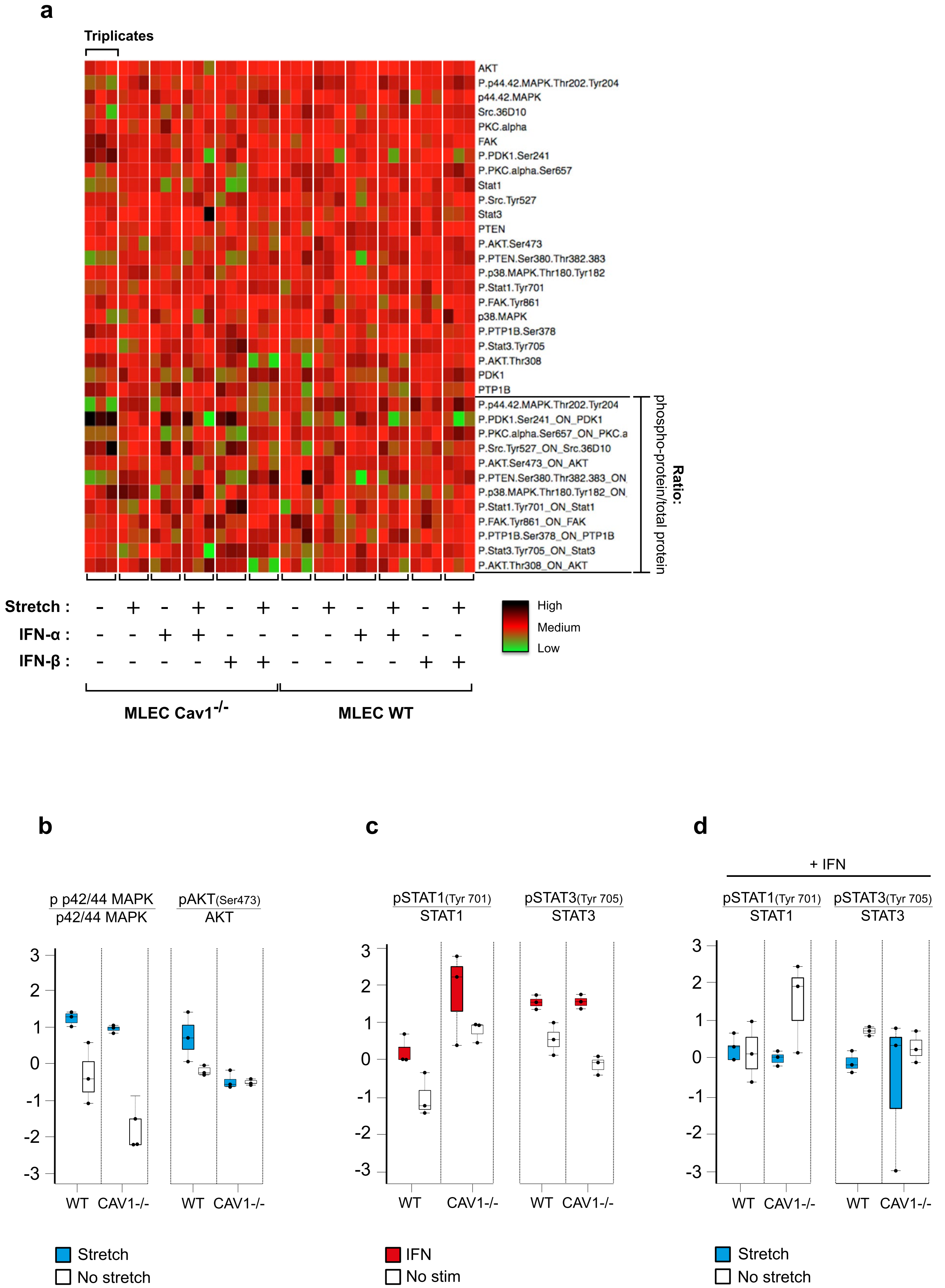

**Extended Data Fig. 6 | See next page for caption.**

**Extended Data Fig. 6 | Stretch- and IFN-dependent signalling responses in MLEC WT and Cav1$^{-/-}$ cells measured by RPPA.** (**a**) Heat map showing activation-state changes of signalling effectors in MLEC WT and MLEC Cav1$^{-/-}$ cells treated or not with Type-I IFN under resting or uniaxial stretch conditions. Heat-map values are shown as log2-transformed phospho-protein/total protein ratios, with 3 independent biological replicates (*n* = 3) per condition. (**b**) Box-and-whisker plots showing p44/42 MAPK and AKT phosphorylation ratios (phospho-protein/total protein) under resting or uniaxial stretch conditions in MLEC WT and MLEC Cav1 − /− cells. (**c**) Box-and-whisker plots showing STAT1 and STAT3 phosphorylation ratios (phospho-protein/total protein) in MLEC WT and MLEC Cav1 − /− cells stimulated or not with Type-I IFN. (**d**) Box-and-whisker plots showing STAT1 and STAT3 phosphorylation ratios (phospho-protein/total protein) in MLEC WT and MLEC Cav1 − /− cells under resting or uniaxial stretch conditions following Type-I IFN stimulation. In (**b**–**d**), data are shown in log2 scale from 3 independent biological replicates (*n* = 3). Box plots are defined as follows: centre line: median; box bounds: 25th and 75th percentiles; whiskers: minimum and maximum values.

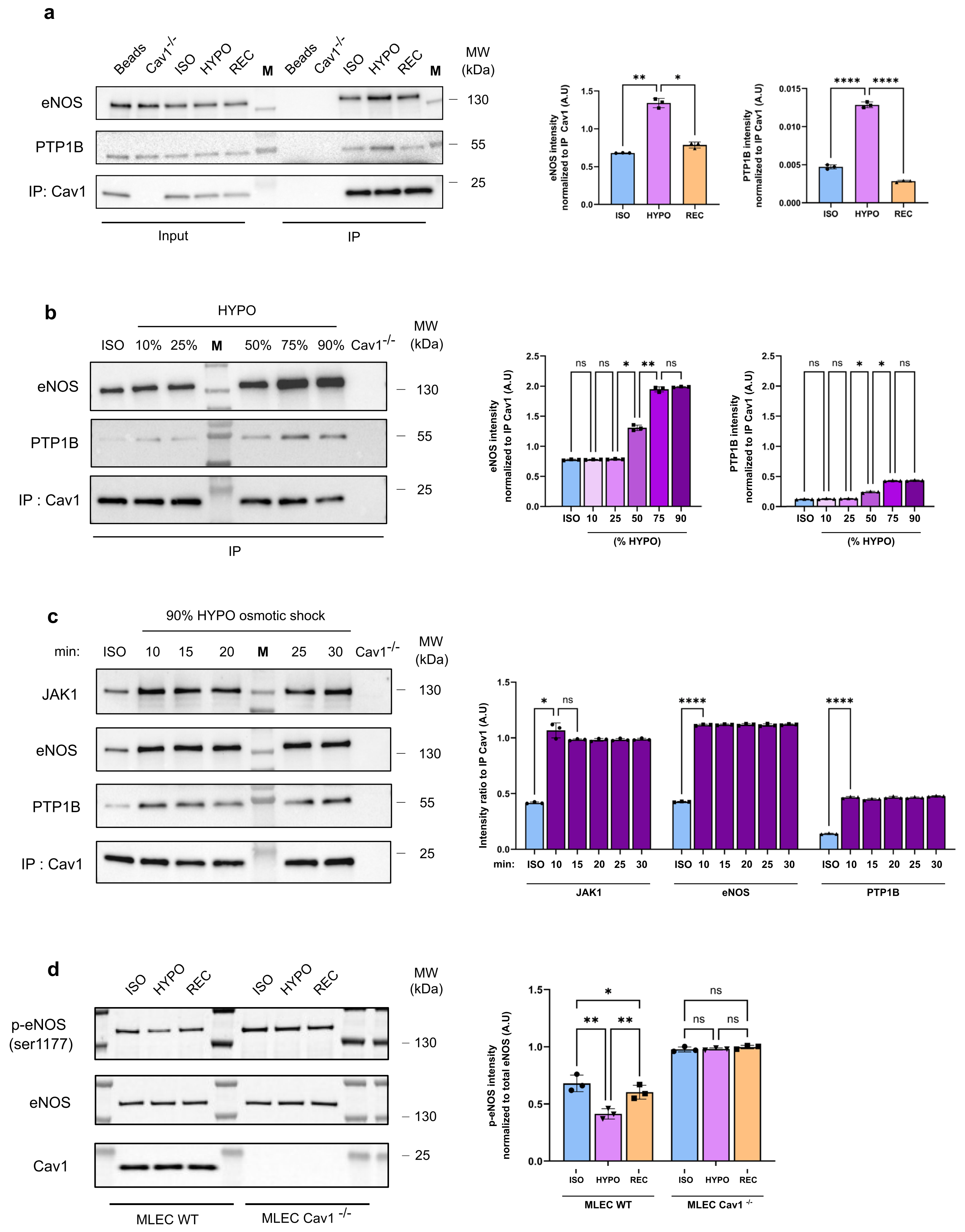

**Extended Data Fig. 7 | See next page for caption.**

**Extended Data Fig. 7 | Cav1 associates with eNOS and PTP1B under increased membrane tension, and Cav1 loss alters eNOS Ser1177 phosphorylation dynamics.** (**a**) Representative co-immunoprecipitation of endogenous eNOS and PTP1B with Cav1 in MLEC WT cells under iso-osmotic (ISO), hypo-osmotic (HYPO) and recovery (REC) conditions. Quantification is based on the signal intensity ratio of eNOS or PTP1B relative to the corresponding immunoprecipitated Cav1 signal. Immunoblots are representative of 3 independent biological experiments with similar results. Quantified data are presented as mean ± SD (bars: mean; error bars: SD), with individual data points representing 3 independent biological replicates ($n = 3$). Statistical significance was assessed using a two-sided one-way ANOVA with multiple-comparisons correction. Exact P values are provided in the Source Data. (**b**) Representative co-immunoprecipitation of endogenous eNOS and PTP1B with Cav1 in MLEC WT cells under ISO and increasing percentages of hypo-osmotic shock (HYPO). Quantification is based on the signal intensity ratio of eNOS or PTP1B relative to the corresponding immunoprecipitated Cav1 signal. Immunoblots are representative of 3 independent biological experiments with similar results. Quantified data are presented as mean ± SD (symbols/line: mean; error bars: SD), with individual data points representing 3 independent biological replicates ($n = 3$). Statistical significance was assessed using a two-sided one-way ANOVA with multiple-comparisons correction. Exact P values are provided in the Source Data. (**c**) Representative co-immunoprecipitation of endogenous JAK1, eNOS and PTP1B with Cav1 in MLEC WT cells under ISO and after increasing durations of 90% hypo-osmotic shock (HYPO). Quantification is based on the signal intensity ratio of each effector relative to the corresponding immunoprecipitated Cav1 signal. Immunoblots are representative of 3 independent biological experiments with similar results. Quantified data are presented as mean ± SD (symbols/line: mean; error bars: SD), with individual data points representing 3 independent biological replicates ($n = 3$). Statistical significance was assessed using a two-sided one-way ANOVA with multiple-comparisons correction. Exact P values are provided in the Source Data. (**d**) Left: MLEC WT and MLEC Cav1 − /− cells were subjected to ISO, HYPO or REC conditions and all samples were stimulated with $H_2O_2$ before lysis. Representative immunoblots show p-eNOS(Ser1177), total eNOS and Cav1. Right: Quantification of p-eNOS(Ser1177) normalized to total eNOS. Immunoblots are representative of 3 independent biological experiments with similar results. Quantified data are presented as mean ± SD (bars: mean; error bars: SD), with individual data points representing 3 independent biological replicates ($n = 3$). Statistical significance was assessed using a two-sided one-way ANOVA with multiple-comparisons correction. Exact P values are provided in the Source Data. $P < 0.05$; $P < 0.01$; **$P < 0.0001$; ns: not significant. Source numerical data and unprocessed blots are available in source data.

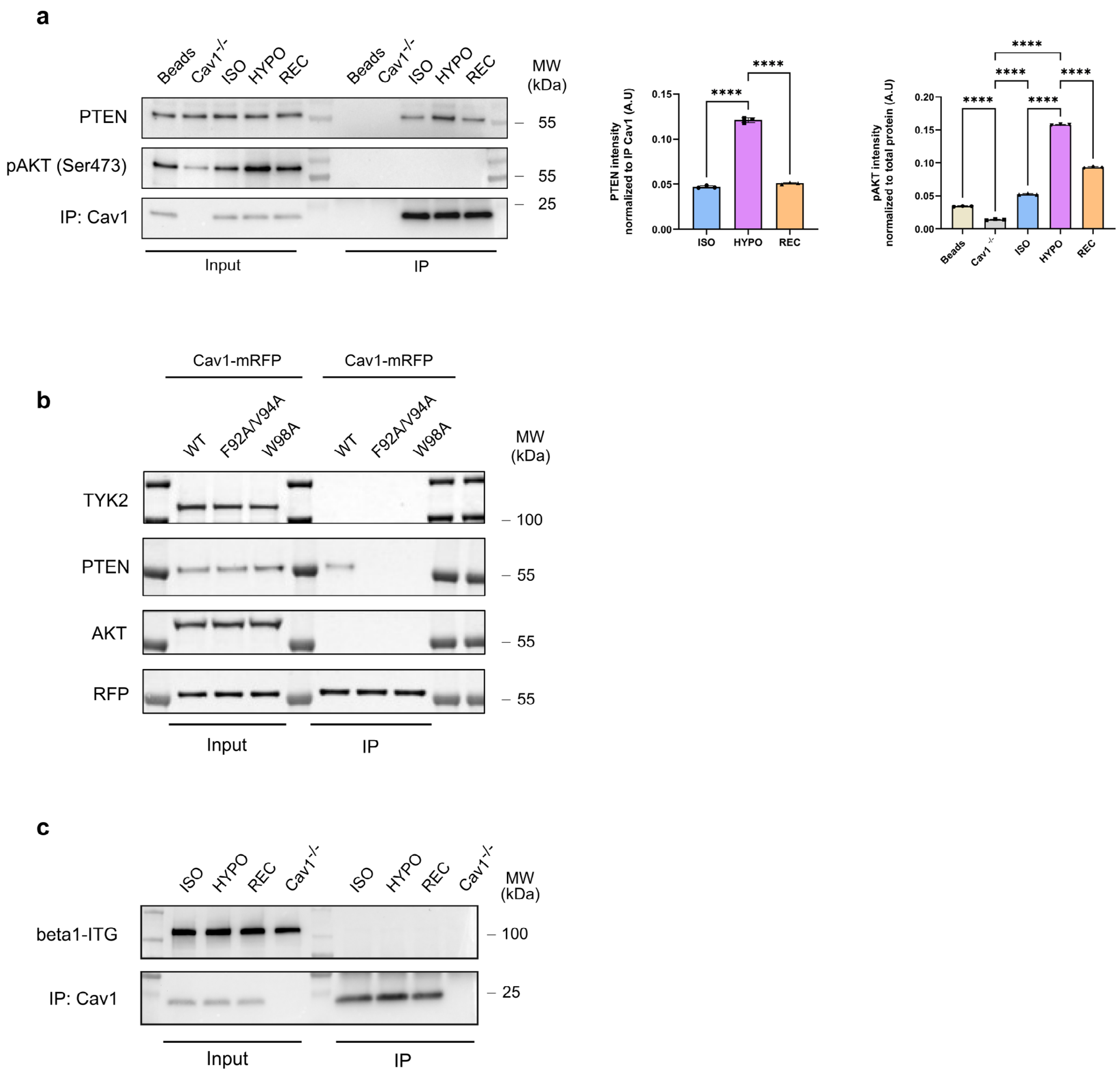

**Extended Data Fig. 8 | Cav1 associates with PTEN, AKT, TYK2 and β1-integrin in a tension and scaffolding domain dependent manner.** (**a**) Representative co-immunoprecipitation of endogenous PTEN with Cav1 in MLEC WT cells under iso-osmotic (ISO), hypo-osmotic (HYPO) and recovery (REC) conditions, together with the corresponding pAKT (Ser473) levels. Quantification of PTEN is based on the signal intensity ratio of PTEN relative to immunoprecipitated Cav1. Quantification of pAKT (Ser473) is based on the signal intensity ratio of pAKT (Ser473) relative to total protein measured from the corresponding stain-free blot. Immunoblots are representative of 3 independent biological experiments (n = 3) with similar results. Quantified data are presented as mean ± SD (bars: mean; error bars: SD) with individual data points representing the 3 independent biological replicates. Statistical significance was assessed using a two-sided repeated-measures one-way ANOVA with multiple-comparisons correction. Exact P values are provided in the Source Data. (**b**) Representative co-immunoprecipitation of Cav1−mRFP with endogenous TYK2, PTEN and AKT in MLEC Cav1 −/− cells expressing Cav1-WT−mRFP, Cav1-F92A/V94A−mRFP or Cav1-W98A−mRFP under ISO conditions. The RFP immunoblot is the same as that shown in Fig. 6h. Immunoblots are representative of 3 independent biological experiments (n = 3) with similar results. (**c**) Representative co-immunoprecipitation of endogenous β1-integrin with Cav1 in MLEC WT cells under ISO, HYPO and REC conditions. Immunoblots are representative of 3 independent biological experiments (n = 3) with similar results. ns = not significant; *: $P < 0.05$; **: $P < 0.01$; ***: $P < 0.001$; ****: $P < 0.0001$. Source numerical data and unprocessed blots are available in source data.

Corresponding author(s): Christophe LAMAZE ; Cedric BLOUIN
Last updated by author(s): Feb 13, 2026

# Reporting Summary

Nature Portfolio wishes to improve the reproducibility of the work that we publish. This form provides structure for consistency and transparency in reporting. For further information on Nature Portfolio policies, see our Editorial Policies and the Editorial Policy Checklist.

## Statistics

For all statistical analyses, confirm that the following items are present in the figure legend, table legend, main text, or Methods section.

| n/a | Confirmed | |
|---|---|---|
| ☐ | ☒ | The exact sample size (*n*) for each experimental group/condition, given as a discrete number and unit of measurement |
| ☐ | ☒ | A statement on whether measurements were taken from distinct samples or whether the same sample was measured repeatedly |
| ☐ | ☒ | The statistical test(s) used AND whether they are one- or two-sided<br>*Only common tests should be described solely by name; describe more complex techniques in the Methods section.* |
| ☒ | ☐ | A description of all covariates tested |
| ☒ | ☐ | A description of any assumptions or corrections, such as tests of normality and adjustment for multiple comparisons |
| ☐ | ☒ | A full description of the statistical parameters including central tendency (e.g. means) or other basic estimates (e.g. regression coefficient) AND variation (e.g. standard deviation) or associated estimates of uncertainty (e.g. confidence intervals) |
| ☐ | ☒ | For null hypothesis testing, the test statistic (e.g. *F*, *t*, *r*) with confidence intervals, effect sizes, degrees of freedom and *P* value noted<br>*Give P values as exact values whenever suitable.* |
| ☒ | ☐ | For Bayesian analysis, information on the choice of priors and Markov chain Monte Carlo settings |
| ☒ | ☐ | For hierarchical and complex designs, identification of the appropriate level for tests and full reporting of outcomes |
| ☐ | ☒ | Estimates of effect sizes (e.g. Cohen's *d*, Pearson's *r*), indicating how they were calculated |

*Our web collection on statistics for biologists contains articles on many of the points above.*

## Software and code

Policy information about availability of computer code

| | |
|---|---|
| Data collection | Images were captured with an Inverted Eclipse Ti-E (Nikon) + Spinning disk CSU-X1 (Yokogawa) integrated in Metamorph software by Gataca Systems. dSTORM single molecule imaging was done using an Abbelight SAFe360 with the spectral demixing mode (dichroic mirror at 700 nm, Chroma) with two sCMOS cameras (Hamamatsu Fusion BT) mounted on an inverted Nikon Ti2-E microscope with a 100X 1.49NA objective. For sptPALM single molecule tracking experiments, acquisitions were steered by MetaMorph software (Molecular Devices) with an inverted motorized microscope (Nikon Ti) equipped with a Nikon CFI Apo TIRF 100x oil, NA 1.49 objective and a perfect focus system, allowing long acquisition in TIRF illumination mode. For DNA-PAINT experiments, a stretching device was mounted on an inverted motorized microscope (Nikon Ti) equipped with a CFI Apochromat TIRF 100× oil, NA 1.49 objective. All images for western blots were acquired by Image Lab 6.1 (BioRad). |
| Data analysis | Microscopy images were processed using ImageJ/Fiji softwares (version up to 2.9.0) as indicated. Western blots were analyzed and quantified using Image Lab 6.1 (BioRad) and ImageJ/Fiji softwares (version up to 2.9.0). dSTORM images were processed with NEO software provided by Abbelight company and later analyzed using a 3D-network analysis pipeline from SuperResNet platform. DNA-PAINT image reconstruction and drift correction were carried out using the Picasso software. For spt-PALM, single molecule fluorescent spots were localized and tracked over time using a combination of wavelet segmentation and simulated annealing algorithms and trajectory analysis was performed using a custom MATLAB algorithm. |

For manuscripts utilizing custom algorithms or software that are central to the research but not yet described in published literature, software must be made available to editors and reviewers. We strongly encourage code deposition in a community repository (e.g. GitHub). See the Nature Portfolio guidelines for submitting code & software for further information.

## Data

Policy information about availability of data

All manuscripts must include a data availability statement. This statement should provide the following information, where applicable:

- Accession codes, unique identifiers, or web links for publicly available datasets
- A description of any restrictions on data availability
- For clinical datasets or third party data, please ensure that the statement adheres to our policy

All data supporting the findings are available from the corresponding authors on reasonable request. Source data are provided with this paper.

## Research involving human participants, their data, or biological material

Policy information about studies with human participants or human data. See also policy information about sex, gender (identity/presentation), and sexual orientation and race, ethnicity and racism.

| | |
|---|---|
| Reporting on sex and gender | *Use the terms sex (biological attribute) and gender (shaped by social and cultural circumstances) carefully in order to avoid confusing both terms. Indicate if findings apply to only one sex or gender; describe whether sex and gender were considered in study design; whether sex and/or gender was determined based on self-reporting or assigned and methods used.*<br>*Provide in the source data disaggregated sex and gender data, where this information has been collected, and if consent has been obtained for sharing of individual-level data; provide overall numbers in this Reporting Summary. Please state if this information has not been collected.*<br>*Report sex- and gender-based analyses where performed, justify reasons for lack of sex- and gender-based analysis.* |
| Reporting on race, ethnicity, or other socially relevant groupings | *Please specify the socially constructed or socially relevant categorization variable(s) used in your manuscript and explain why they were used. Please note that such variables should not be used as proxies for other socially constructed/relevant variables (for example, race or ethnicity should not be used as a proxy for socioeconomic status).*<br>*Provide clear definitions of the relevant terms used, how they were provided (by the participants/respondents, the researchers, or third parties), and the method(s) used to classify people into the different categories (e.g. self-report, census or administrative data, social media data, etc.)*<br>*Please provide details about how you controlled for confounding variables in your analyses.* |
| Population characteristics | *Describe the covariate-relevant population characteristics of the human research participants (e.g. age, genotypic information, past and current diagnosis and treatment categories). If you filled out the behavioural & social sciences study design questions and have nothing to add here, write "See above."* |
| Recruitment | *Describe how participants were recruited. Outline any potential self-selection bias or other biases that may be present and how these are likely to impact results.* |
| Ethics oversight | *Identify the organization(s) that approved the study protocol.* |

Note that full information on the approval of the study protocol must also be provided in the manuscript.

# Field-specific reporting

Please select the one below that is the best fit for your research. If you are not sure, read the appropriate sections before making your selection.

☒ Life sciences ☐ Behavioural & social sciences ☐ Ecological, evolutionary & environmental sciences

For a reference copy of the document with all sections, see nature.com/documents/nr-reporting-summary-flat.pdf

# Life sciences study design

All studies must disclose on these points even when the disclosure is negative.

| | |
|---|---|
| Sample size | Sample size for each experiment is indicated in figure captions. No statistical method was used to determine sample size prior to experiment. Sample size were chosen based on previous studies (Blouin et al., Cell 2016; Chmiest et al., Nat Commun 2016; Dewulf et al., Nat Commun 2019; Zanin et al., Nat Cell Biol 2023). |
| Data exclusions | No data was excluded from statistical analysis. |
| Replication | Unless stated otherwise in the figure legends, all representative results shown for immunolabelling, high-throughput screening, in-vitro kinase activity, dSTORM, sptPALM and western blot experiments were performed at least three times independently with similar results. |
| Randomization | For comparison between experimental groups (control vs treatment), the samples were asigned randomly to each group. All the control and treated experiments were done on the same day side by side using the same reagents batches. |
| Blinding | Investigators were not blinded as same person both collected and analysed the data. |

# Reporting for specific materials, systems and methods

We require information from authors about some types of materials, experimental systems and methods used in many studies. Here, indicate whether each material, system or method listed is relevant to your study. If you are not sure if a list item applies to your research, read the appropriate section before selecting a response.

## Materials & experimental systems

| n/a | Involved in the study | |
|---|---|---|
| ☐ | ☒ | Antibodies |
| ☐ | ☒ | Eukaryotic cell lines |
| ☒ | ☐ | Palaeontology and archaeology |
| ☒ | ☐ | Animals and other organisms |
| ☒ | ☐ | Clinical data |
| ☒ | ☐ | Dual use research of concern |
| ☒ | ☐ | Plants |

## Methods

| n/a | Involved in the study | |
|---|---|---|
| ☒ | ☐ | ChIP-seq |
| ☒ | ☐ | Flow cytometry |
| ☒ | ☐ | MRI-based neuroimaging |

## Antibodies

Antibodies used

The following primary antibodies were used: mouse anti-α-tubulin (Sigma-Aldrich, clone B512, Cat. #T5168, 1:1000 for WB); mouse anti-CHC (BD Transduction, Cat. #610500, 1:5000 for WB); mouse anti-STAT3 (Cell signaling, clone 124H6, Cat. #9139, 1:1000 for WB); rabbit anti-pSTAT3 (Tyr705) (Cell signaling technologies, clone D3A7, Cat. #9145, 1:1000 for WB, 1:100 for IF); rabbit anti-STAT1 (Cell signaling technologies, Cat. #9172, 1:1000 for WB); mouse anti-pSTAT1 (Tyr701) (Cell signaling technologies, clone 58D6, Cat. #9167, 1:1000 for WB, 1:100 for IF); mouse anti-Cav1 (BD Transduction, Cat. #610407, 1:1000 for WB); rabbit anti-Cav1 (Cell Signaling Technologies Cat. #3238S, 1:1000 for WB, 2-5 µg/condition for IP, 1:50 for dSTORM, 1:150 for IF); mouse anti-PTRF (BD Transduction Cat. #611258, 1:1000 for WB); rabbit anti-PTRF (Cat. #ab48824, Abcam – discontinued, 1:1000 for WB, 1:50 for dSTORM, 1:150 for IF); rabbit anti-JAK1 (Cell signaling technologies, Cat. #3332S, 1:2000 for WB); mouse anti-JAK1 (Santa Cruz Biotechnology, Cat. #sc-1677, 1:50 for STORM); rabbit anti-eNOS (Cell signaling technologies Cat. #32027S, 1:2000 for WB); rabbit anti-PTEN (Cell signaling technologies Cat. #9188S, 1:2000 for WB); rabbit anti-AKT (Cell signaling technologies Cat. #9272S, 1:2000 for WB); rabbit anti-pAKT (Ser473) (Cell signaling technologies Cat. #4060S, 1:2000 for WB); rabbit anti-PTP1B (Abcam Cat. #ab244207, 1:2000 for WB); rabbit anti-mCherry (Institut Curie Recombinant antibody platform, A-P-R #13); rabbit p-eNOS (Ser1177) (Thermo Fisher Cat. # PA5-104858, 1:2000 for WB).

The following secondary antibodies were used: Donkey anti-mouse-HRP (Jackson ImmunoResearch, cat. #715-035-151) and Donkey anti-rabbit-HRP (Jackson ImmunoResearch, cat. #711-035-152) were used at a dilution of 1:5,000 for WB; Donkey anti-mouse-AF647 (Jackson ImmunoResearch, cat. #715-606-150) and Donkey anti-rabbit-CF680 (Biotium, cat. #20820) were used at a dilution of 1:200 and 1:400 respectively, for STORM imaging. ChromoTek GFP-Booster AF647, Cat. # gb2AF647); Donkey anti-mouse DyLight 800 (cat. #SA5-10172); Donkey anti-goat DyLight 800 (cat. #SA5-10044) ..

Validation

The following primary antibodies have been characterized by their manufacturer:
mouse anti-α-tubulin: https://www.sigmaaldrich.com/FR/fr/product/sigma/t5168
mouse anti-CHC:https://www.bdbiosciences.com/en-ca/products/reagents/microscopy-imaging-reagents/immunofluorescence-reagents/purified-mouse-anti-clathrin-heavy-chain.610500
mouse anti-STAT3: https://www.cellsignal.com/products/primary-antibodies/stat3-124h6-mouse-mab/9139
rabbit anti-pSTAT3: https://www.cellsignal.com/products/primary-antibodies/phospho-stat3-tyr705-d3a7-xp-rabbit-mab/9145
rabbit anti-STAT1: https://www.cellsignal.com/products/primary-antibodies/stat1-antibody/9172
mouse anti-pSTAT1(Tyr 701): https://www.bdbiosciences.com/en-us/products/reagents/flow-cytometry-reagents/research-reagents/single-color-antibodies-ruo/purified-mouse-anti-stat1-py701.612132
mouse anti-Cav1: https://www.bdbiosciences.com/en-us/products/reagents/microscopy-imaging-reagents/immunofluorescence-reagents/purified-mouse-anti-caveolin-1.610407
rabbit anti-Cav1: https://www.cellsignal.com/products/primary-antibodies/caveolin-1-antibody/3238
rabbit anti-PTRF: discontinued; original webpage no longer available; 3rd party website link: https://www.citeab.com/antibodies/749886-ab48824-anti-ptrf-antibody
mouse anti-PTRF: discontinued; webpage no longer available
rabbit anti-JAK1: https://www.cellsignal.com/products/primary-antibodies/jak1-antibody/3332
mouse anti-JAK1: https://www.scbt.com/p/jak1-antibody-a-9
rabbit anti-eNOS: https://www.cellsignal.com/products/primary-antibodies/enos-d9a5l-rabbit-mab/32027
rabbit anti-PTEN: https://www.cellsignal.com/products/primary-antibodies/pten-d4-3-xp-rabbit-mab/9188
rabbit anti-AKT: https://www.cellsignal.com/products/primary-antibodies/akt-antibody/9272
rabbit anti-pAKT (Ser473): https://www.cellsignal.com/products/primary-antibodies/phospho-akt-ser473-d9e-xp-rabbit-mab/4060
rabbit anti-PTP1B: https://www.abcam.com/en-us/products/primary-antibodies/ptp1b-antibody-epr22474-ab244207
rabbit anti-mcherry(recombinant antibody platform, Institut Curie) have been characterized by immunofluorescence and western blot with expected localization and molecular weight.
rabbit anti-p-eNOS (Ser1177): https://www.thermofisher.com/antibody/product/Phospho-eNOS-Ser1177-Antibody-Polyclonal/PA5-104858

The secondary antibodies have been characterized by their manufacturer:
Donkey anti-mouse-HRP: https://www.jacksonimmuno.com/catalog/products/715-035-151

Donkey anti-rabbit-HRP: https://www.jacksonimmuno.com/catalog/products/711-035-152
Donkey anti-mouse-AF647: https://www.jacksonimmuno.com/catalog/products/715-606-150
Donkey anti-rabbit-CF680: https://www.insightbio.com/productinfo/20820-50uL/Biotium
ChromoTek GFP-Booster AF647: https://www.ptglab.com/products/GFP-Booster-Alexa-Fluor-647-gb2AF647.htm
Donkey anti-mouse DyLight 800: https://www.thermofisher.com/antibody/product/Donkey-anti-Mouse-IgG-H-L-Cross-Adsorbed-Secondary-Antibody-Polyclonal/SA5-10172
Donkey anti-rabbit DyLight 800: https://www.thermofisher.com/antibody/product/Donkey-anti-Rabbit-IgG-H-L-Cross-Adsorbed-Secondary-Antibody-Polyclonal/SA5-10044

## Eukaryotic cell lines

Policy information about cell lines and Sex and Gender in Research

| | |
|---|---|
| Cell line source(s) | MLEC WT ; MLEC CAV1-/- ; MEF WT ; MEF CAVIN1-/- |
| Authentication | None used. |
| Mycoplasma contamination | All cell lines were regularly tested for mycoplasma contamination either in our lab (Mycoalert PLUS detection kit, #LT07-710; Lonza) or by the GATC/eurofins company (Mycocheck service ; https://eurofinsgenomics.eu/). |
| Commonly misidentified lines (See ICLAC register) | No commonly misidentified cell lines were used in this study. |

## Plants

| | |
|---|---|
| Seed stocks | *Report on the source of all seed stocks or other plant material used. If applicable, state the seed stock centre and catalogue number. If plant specimens were collected from the field, describe the collection location, date and sampling procedures.* |
| Novel plant genotypes | *Describe the methods by which all novel plant genotypes were produced. This includes those generated by transgenic approaches, gene editing, chemical/radiation-based mutagenesis and hybridization. For transgenic lines, describe the transformation method, the number of independent lines analyzed and the generation upon which experiments were performed. For gene-edited lines, describe the editor used, the endogenous sequence targeted for editing, the targeting guide RNA sequence (if applicable) and how the editor was applied.* |
| Authentication | *Describe any authentication procedures for each seed stock used or novel genotype generated. Describe any experiments used to assess the effect of a mutation and, where applicable, how potential secondary effects (e.g. second site T-DNA insertions, mosiacism, off-target gene editing) were examined.* |